

Titre: Metrology Frame for Robotic Machining of Pockets in Large Flexible
Title: Panels

Auteur: Mehdi Rasoulimir
Author:

Date: 2013

Type: Mémoire ou thèse / Dissertation or Thesis

Référence: Rasoulimir, M. (2013). Metrology Frame for Robotic Machining of Pockets in Large Flexible Panels [Mémoire de maîtrise, École Polytechnique de Montréal].
Citation: PolyPublie. <https://publications.polymtl.ca/1273/>

 **Document en libre accès dans PolyPublie**
Open Access document in PolyPublie

URL de PolyPublie: <https://publications.polymtl.ca/1273/>
PolyPublie URL:

Directeurs de recherche: Luc Baron, & J. R. René Mayer
Advisors:

Programme: Génie mécanique
Program:

UNIVERSITÉ DE MONTRÉAL

METROLOGY FRAME FOR ROBOTIC MACHINING
OF POCKETS IN LARGE FLEXIBLE PANELS

MEHDI RASOULIMIR

DÉPARTEMENT DE GÉNIE MÉCANIQUE
ÉCOLE POLYTECHNIQUE DE MONTRÉAL

MÉMOIRE PRÉSENTÉ EN VUE DE L'OBTENTION
DU DIPLÔME DE MAÎTRISE ÈS SCIENCES APPLIQUÉES
(GÉNIE MÉCANIQUE)

NOVEMBRE 2013

UNIVERSITÉ DE MONTRÉAL

ÉCOLE POLYTECHNIQUE DE MONTRÉAL

Ce mémoire intitulé:

METROLOGY FRAME FOR ROBOTIC MACHINING OF
POCKETS IN LARGE FLEXIBLE PANELS

présenté par : RASOULIMIR Mehdi

en vue de l'obtention du diplôme de : Maîtrise ès sciences appliquées

a été dûment accepté par le jury d'examen constitué de :

M. BALAZINSKI Marek, Docteur ès sciences, président

M. BARON Luc, Ph.D., membre et directeur de recherche

M. MAYER René, Ph.D., membre et codirecteur de recherche

M. ACHICHE Sofiane, Ph.D., membre

DEDICATION

This dissertation is dedicated to my family. My parents who have been the strong and steadfast support in my journey. They taught me the value of life and faithful love. Most of all, I cannot fully express in words for priceless love and encouragement that my wife and my son brought in my life.

ACKNOWLEDGEMENTS

I would never have been able to finish my dissertation without the guidance of my committee members, help from friends, and support from my family and wife.

I would like to express my deepest gratitude to my advisor and co-advisor, Dr. Luc Baron and Dr. René Mayer, for their excellent guidance, caring, patience, and providing me with an excellent atmosphere for doing research. I also appreciate my advisory committee, Dr. Marek Balazinski and Dr. Sofiane Achiche for all their guidance and valuable comments on my research.

I would also like to thank Mr. Guy Gironne, Mr. Francois Ménard and Mr. Vincent Mayer from LRFV lab. and Mr. Nour Aimene, electrical technician, All in the Department of mechanical engineering of École Polytechnique de Montréal for their kindly help during implementation of the project.

Moreover, the project was funded by BOMBARDIER Co. and CRIAQ, I am also grateful of these two organizations for their financial support .

Finally, I would like to thank my wife, Fatemeh. She was always there cheering me up and stood by me through the good times and bad.

RÉSUMÉ

Cette recherche présente une nouvelle technologie pour l'usinage robotisé de poches dans les grands panneaux flexibles. Pas d'articles pertinents ont été trouvés dans la littérature, mais un certain nombre de brevets examinés fournis certains des idées de base pour la conception. En particulier, il apparaît essentiel de soutenir le panneau où les forces d'usinage sont appliquées. Pour atteindre cet objectif, un cadre en C est proposé. En appliquant la méthode des éléments finis (MEF) tous les déplacements et les contraintes dans toute la structure sont évalués. Cela révèle que dû à l'effet des forces d'usinage, les deux branches de l'extrémité du cadre en C proposé dévient en sens inverse entraînant une ouverture importante du cadre en C. Pour mesurer cette déviation excessive, un cadre métrologique est conçu où un faisceau laser passe à travers les éléments optiques et atteint un photodétecteur. La position de la tache laser sur la surface du photodétecteur spécifie la distance momentanée entre les deux branches de l'extrémité du cadre en C. Toute déviation due à la force d'usinage affecte cette distance et sera donc détectée par la photodiode afin d'être compensée. Un prototype en bois du cadre en C est construit pour évaluer l'efficacité du cadre de métrologie optique. Les résultats indiquent que la déviation peut être mesurée avec une répétabilité de $\pm 0,1$ mm et une exactitude de $\pm 0,0884$ mm.

ABSTRACT

This thesis presents a new technology for the robotic machining of pockets in large and flexible panels. No relevant research papers were found in the literature but a number of patents are reviewed providing some basic for a conceptual design. In particular, it appears essential to support the panel where machining forces are applied. In order to achieve this goal, a C-frame is proposed. By applying FEA all of the displacements and stresses throughout the structure are evaluated. This reveals that due to machining forces, the two arms of the proposed C-frame deflect in opposite direction resulting in a significant opening of the C-frame. In order to measure this excessive deflection, a metrology frame is designed where a laser beam passes through optical elements and reaches a photodetector. The position of the laser spot on the photodetector surface specifies the momentary distance between the two arms of the C-frame. Any deflection due to machining force affects this distance and therefore will be sensed by the photodiode in order to be compensated. A small version of the C-frame is built from wood to assess the effectiveness of the optical metrology frame. Results indicate that the deflection can be measured with a repeatability of $\pm 0.1 \text{ mm}$ and precision of $\pm 0.0884 \text{ mm}$.

TABLE OF CONTENTS

DEDICATION	III
ACKNOWLEDGEMENTS	IV
RÉSUMÉ.....	V
ABSTRACT	VI
TABLE OF CONTENTS	VII
LIST OF TABLES	IX
LIST OF FIGURES.....	X
LIST OF ABBREVIATIONS	XIII
LIST OF APPENDIXES	XIV
INTRODUCTION.....	1
CHAPTER 1 LITERATURE REVIEW.....	3
1.1 Introduction.....	3
1.2 Robotic machining of parts	4
1.2.1 Modeling of robotic machining.....	6
1.2.2 Analysis of chatter in machining.....	8
1.2.3 Deformation Compensation	9
1.2.4 Robot calibration.....	11
1.2.5 Future research	12
1.3 Robotic machining of panels.....	12
1.3.1 Background	12
1.3.2 Patent Review.....	15
1.4 Literature Review Conclusion.....	20
CHAPTER 2 DESIGN AND IMPLEMENTATION.....	21

2.1	Proposed solution (mechanical design).....	21
2.1.1	Conceptual design	22
2.1.2	Finite Element Analysis (FEA) of C-frame	24
2.2	Design of metrology frame	26
2.2.1	Conceptual design	26
2.2.2	Elements of metrology frame and their functions	28
2.2.3	Optical assessments of laser beam by Jones matrix	33
2.3	Implementation.....	37
2.4	Electrical section	38
2.4.1	Photodiode and its application in position sensing	38
2.4.2	Implementation of the circuit	40
CHAPTER 3	CONDUCTING A METROLOGY TEST AND DISCUSSION.....	43
3.1	Deflection test	44
3.2	Repeatability tests	48
3.3	Laser head rotation	49
3.4	Accuracy of the measurements	51
CONCLUSION AND FUTURE WORKS	55
Conclusion.....	55
Future works.....	56
REFERENCES.....	57
APPENDIXES	63

LIST OF TABLES

Table 2.1: Jones vector representing polarization states	35
Table 2.1: Jones matrix of common optical elements	35
Table 3.1: Error signals associated with the data in terms of amplitude and frequency.....	54

LIST OF FIGURES

Figure 1.1: Recommended set-up for COMMET.....	5
Figure 1.2: Contour of the total deformation	7
Figure 1.3: Block diagram of real time deformation compensation	9
Figure 1.4: Controlled Material Removal Rate (MRR).....	10
Figure 1.5: Using double robot in machining of panels (GAP project).....	13
Figure 1.6: Panel milling by Torres surface milling machine.....	14
Figure 1.7: Grasping machining end-effector.....	15
Figure 1.8: C-clamp preliminary idea.....	16
Figure 1.9: Illustration of work cell and robot equipped with an end-effector (C-clamp).....	16
Figure 1.10: Using two mirror robots in fastening operations.....	17
Figure 1.11: Machining of panels by two mechanisms (robot).....	18
Figure 1.12: A schematic view of the machining process.....	19
Figure 1.13: Partial cross-sectional view of producing a recess.....	19
Figure 2.1: Conceptual schematic of C-frame based robotic machining	22
Figure 2.2: Conceptual design of C-frame.....	23
Figure 2.3: Placing of tool and support in C-frame	23
Figure 2.4: 3D view of C-frame.....	24
Figure 2.5: Deflection in opposite sides together with nodal stress values.....	25
Figure 2.6: Range of displacement in C-frame because of machining force	25
Figure 2.7: Conceptual metrology frame	27
Figure 2.8: Using quarter and half wave plate to control light polarization	27
Figure 2.9: Linearly polarized light	28
Figure 2.10: Circularly polarized light (just electrical fields are shown).....	29

Figure 2.11: Elliptically polarized light (just electrical fields are shown)	29
Figure 2.12: Polarizing beamsplitter.....	30
Figure 2.13: Using QWP to change the polarization of light	31
Figure 2.14: Using QWP to change the polarization of light.....	31
Figure 2.15: Changing the orientation of a linealy polarized light by HWP.....	32
Figure 2.16: Pentaprism used to change the direction of the light by 90^0	32
Figure 2.17: Retroreflector is composed of three perpendicular reflecting faces	33
Figure 2.18: Retroreflector inverts an image while invesing	33
Figure 2.19: Horizontally polarized light	34
Figure 2.20: Effects of several components on the state of polarization.....	36
Figure 2.21: Nominal state of polarization in C-frame (c:circular, s: s-linea, p:p-linear).....	36
Figure 2.22: Arrangement of metrology elements in CATIA.....	37
Figure 2.23: Implemented metrology frame	38
Figure 2.24: Quadrant photodiode and its coordinate frame	39
Figure 2.25: Positionalresolution.....	40
Figure 2.26: Final electrical circuit	41
Figure 2.27: Electrical section	42
Figure 3.1: Coordinate and directions used during the tests	43
Figure 3.2: Beam position because of deflection in lower arm	44
Figure 3.3: Beam position because of deflection in upper arm.....	45
Figure 3.4: Proposed manual deflection producing	46
Figure 3.5: Measured position with respect to deflection	47
Figure 3.6: Voltage with respect to beam position for different beam diameter	47
Figure 3.7: Repeatability test.....	48

Figure 3.8: Residuals of the repeatability data with respect to the best fit	49
Figure 3.9: Measured position with respect to laser rotation around y axis.....	50
Figure 3.10: Measured position with respect to laser rotation around x axis.....	50
Figure 3.11: Associated error without any laser light(Horizontal scale = 10 $ns/div.$, Vertical scale = 100 $mv/div.$).....	51
Figure 3.12: Error signal related to leg A of photodiode(Horizontal scale = 10 $ns/div.$, Vertical scale = 100 $mv/div.$).....	52
Figure 3.13: Error signal of first differential amplifier.....	53
Figure 3.14: Error signal of sum amplifier.....	53

LIST OF ABBREVIATIONS

CNC	Computer Numerical Control
FCC	Face Centered Cubic
CAD/CAM	Computer Aided Design/Computer Aided Manufacturing
PbG	Programming by Guiding
MRR	Material Removal Rate
GAP	Green Advanced Panels
USPTO	United States Patent and Trademark Office
FEM	Finite Element Modeling
FEA	Finite Element Analysis
PSD	Position Sensing Detector
3D	3 Dimensions
MMMT	Micro/Meso scale Machine Tool
CCD	Charge Coupled Device
PBS	Polarizing Beam Splitter
QWP	Quarter Wave Plate
HWP	Half Wave Plate

LIST OF APPENDIXES

APPENDIX A: C-frame drawing.....	63
APPENDIX B: Matlab code.....	64
APPENDIX C: Principles of photodiode.....	65
APPENDIX D: Op-amp function and application	67
APPENDIX E: Elements of metrology frame	73
APPENDIX F: Elements of electrical section	79
APPENDIX G: Tests Data.....	80
APPENDIX H: Noise signals related to each segment of the electrical section.....	88

INTRODUCTION

The use of robot manipulators in industries is increasing widely. Among them, in machining applications such as milling and turning, using robots brings flexibility and cost-effectiveness. The industrial requirement is to replace chemical machining of pockets in thin aluminum (or aluminum-lithium) aircraft panels with mechanical milling. Up to now, two industrial methods are available for skin milling but the dedicated equipment used is very expensive. The approach used involves machining on one side of the panel while a secondary machine located on the opposite panel side provides the necessary reaction force and probably thickness data. Both sides require a multi-axis mechanical system and a careful synchronization of this motions. Furthermore, the machining accuracy is obtained through a long mechanical loop which imposes strong constraints on the accuracy of the whole mechanical work cell.

- **Problem Statement**

The main issue in robot-assisted machining is the low stiffness of the robot which causes low accuracy with respect to traditional CNC machining. Moreover, in skin machining tasks, flexibility of the panels is also an issue.

- **Research Question**

- How can the tight tolerance (0.05 mm) on pocket from thickness in robotic milling be achieved?
- How can the flexible panel be supported?
- What is the impact of low stiffness of the robot on the machining process?

- **Hypothesis**

It may be possible to remove all obstacles in robotic skin machining by using a mechanical frame and a metrology frame simultaneously.

- **Solution**

In order to reach the desired precision and accuracy during robotic-machining of large flexible panels using a single robot, a mechanical and a metrology frame are proposed. The mechanical C-frame end-effector is designed to reach both sides of the panels thus providing the in-plane movement in addition to supporting the panel on the opposite side of machining by using a spherical support (ball). The metrology frame is designed and embedded inside the mechanical frame to maintain the necessary precision. This metrology frame is able to compensate deflection induced by both the weight of the C-frame and the machining forces.

- **Originality**

Up to date, no publication exists in the realm of milling of panels. On the other hand, published papers concerning robotic machining are rare. Moreover, an inventive method is used in this project which wisely combines two different frames: mechanical and metrology.

- **Contribution and deliverables**

Owing to the novelty of the proposed solution, this project can be patented. Furthermore, against chemical machining, this project is more environmentally friendly and compared to CNC machining, it is more flexible and cost effective.

CHAPTER 1 LITERATURE REVIEW

This chapter reviews the related subjects in the literature and starts with a brief introduction about the place of robotic machining and its advantages and disadvantages. It is divided in two sections: robotic machining of parts and the panels. The related ideas and views about the design are mainly driven from patent review and finally this chapter ends up with a conclusion of literature review.

1.1 Introduction

Having many distinguishing features such as good corrosion and oxidation resistance, high electrical and thermal conductivities, low density (one third of the weight of an equivalent volume of steel), high reflectivity, high ductility, reasonably high strength and relatively low cost, renders aluminum suitable for a wide variety of use in the aerospace and automobile industries. Furthermore, aluminum alloys have the face-centered cubic (FCC) structure, which is stable up to its melting point at 657 °C, and hence contains multiple slip planes which contributes to the excellent formability of aluminum alloys.

Aluminum lithium (Al-Li) alloys are a series of alloys of aluminium usually containing around 2-3% lithium along with copper and magnesium. Lithium reduces density and increases stiffness when alloyed with aluminium (every 1% by weight of lithium added to aluminium reduces the density of the resulting alloy by 3%). With proper alloy design, aluminium-lithium alloys can have exceptional combinations of strength and toughness [1].

These properties make Al-Li particularly suitable to any application where weight to strength ratio is critical and fatigue cracking is a concern. Aerospace and motorsport are typical application areas as well as space exploration where these alloys have been extensively used.

Today's aircraft and aerospace industry requests twofold support from its raw material suppliers, demands include improved toughness, lower weight, increased resistance to fatigue and corrosion. Aluminium and its alloys are amongst the key materials facing these challenges.

Most aluminum parts are produced by casting in foundry plants followed by cleaning, machining, coating and assembly. Today most of the cleaning operations are done in noisy, dusty and unhealthy environment. Therefore, automation for these operations is highly desirable. However,

due to the complex and irregular shape of these cast parts solutions based on CNC machining center is a high cost and non-flexible investment. The main limitation of actual CNC machines is the limited working area that forces the machining tasks to be done in multiple steps and different operations. In contrast, with robots, wider working area up to $20m^3$ is accessible and due to the flexible kinematics of robot, they are capable of machining parts with complex shapes, instead of conventional CNC machine that needs special fixtures and set-up to produce them [2].

Moreover, recent demands of industry indicate the need for low-volume and wide-variety products. Besides, new research in manufacturing and tool design represent the needs of flexibility to overcome the current change in the market. Knowing the fact that solutions based on robots for process such as welding, painting, deburring, etc. are available, it seems that an industrial robot can cover these needs for its time-saving, cost-effectiveness and flexibility.

1.2 Robotic machining of parts

Robotic machining can be roughly defined as machining performed by industrial robots. Robotic machining usually involves multiple paths processes by controlling five or more axes of motion, and the use of spindle and tool to remove material from a part [2].

Controlling and programming a robot to simulate a 5 axis CNC machine tool was reported by D. Milutinovic *et al.* [3]. The benefits of this multi-axis robot is that it can be regarded as a vertical tilting type 5-axis CNC machine (three translations and two rotations) so that it can be beneficial to use all CAD/CAM programs as well as G-code programming even as 3-axis or 5-axis machine tools. Hence it can be implemented easily in machine shops by experienced personnel.

The major obstacle preventing the adoption of robots for material removal processes is the fact that the stiffness of today's industrial robot is much lower than that of a standard CNC machine. The stiffness for a typical articulated robot is usually less than $1 N/\mu m$, while a standard CNC machine center very often has stiffness greater than $50 N/\mu m$ [4].

As is considered in [5,6], there are three major challenges in adopting robots for precision machining tasks. The first difficulty is to generate a motion path for the robot to follow especially for complex workpieces. In on-line programming that is known as jog-and-teach method, the skilled worker teaches the entire path to the robot. This is time-consuming and inaccurate. In off-line programming, the path is taught to the robot based on CAD data of the workpiece. This is

based on accurate modeling of Robot and part and it is cost-effective just for mass production. To face these problems, Z. Pan presented the Programming by Guiding (PbG) method which allows the operator to program robot considering both process requirements and motion path.

The second challenge is the deformation caused by interaction forces between tool and workpiece. Because of low stiffness of robots and for equal force, deformations in robots will be more critical and lead to inaccuracy in the finished part. As a result, a program that does not consider this force-induced deformation is doomed to fail especially in machining with non-constant depth of cut which undoubtedly produces variable force.

The third challenge is chatter that becomes more crucial due to low stiffness and coupled structure of the Robot [5]. To confront this, one solution is to assign time-consuming effort to adjust machining parameters and in most cases much lower material removal rate than the possible machining capacity of the spindle.

The COMET¹ project lead by Delcam aims to overcome the challenges facing European manufacturing industries[7] by bringing industrial robot to the accuracy requested by high-end machining. According to COMET set-up, the tool is controlled by piezo-actuated mechanism and the workpiece is held by the robot Figure 1.1.



Figure1.1 Recommended set-up by COMET [8]

¹Plug-and-produce**CO**mponents and **ME**thods for adaptive control of industrial robots enabling cost effective, high precision manufacturing in factories of the future

COMET is based on the four following innovations [9]:

- 1- methodology for describing kinematic and dynamic behavior of industrial robots;
- 2- an integrated programming and simulation environment for adaptive tool path generation;
- 3- an adaptive optical tracking system to help adjust the robot arm in relation to where it should be according to the initial programmed robot path and make correction via the Robot controller;
- 4- dynamic compensation mechanism needed to achieve accuracy better than $50 \mu m$.

These innovations will be applied to the most common robot available on the market with an anticipated 30% cost efficiency saving with respect to CNC machines.

1.2.1 Modeling of robotic machining

Most robots are modelled as cantilever beam in which each of the links is held by a motor, brake and reduction gears prone to disturbance caused by machining forces [10]. Machining processes are essentially position tasks which require the end-effector of the robot to establish physical contact with the environment and counteract a process-specific force. Characterization of the interaction between the tool and the workpiece is essential for analysing and solving the outstanding problems in robotic machining.

Pan *et al.* [11], assumed that the workpiece is mounted in a sufficiently stable foundation, and proceeded to determine the robot-tool structure model by using transfer function in the *S-domain* and differential equation in the time domain. They found that the dominant factor for a large deflection of the manipulator tip position is the joint compliance because of gear transmission elasticity. Then they concluded the robot stiffness model could be modelled by six rotational stiffness coefficients in the joint space. It was noted that the stiffness matrix of any robot is configuration dependent and non-diagonal. In other words, the force and displacement are coupled in Cartesian space, so the force applied in one direction will affect the deformation in all directions.

Regarding the machining force model, there are many references in the literature. Mainly Y. Altintas [12] represented this force as a non-linear function of width of cut, depth of cut and feed rate.

Modelling of a machining robot considering its parameter identification and focusing on system's stiffness and its behaviour during the milling process has been made by E. Abele *et al.*[13]. They concluded that gear compliance was a dominant factor in deviation of the tool centre point. To overcome this, they developed a model as a function of gear's stiffness of each axis and used the principles of virtual works to calculate the Cartesian compliance. Knowing the process forces and the compliance model, the tool path can be controlled and consequently the accuracy of an industrial robot for machining application can be increased. Moreover, in [14] they presented a method to predict static displacement as well as low frequency oscillations of the tool tip by coupling of robot model with a milling process model.

The robot deformation due to an applied load was studied using FEM by C. Doukaset *al.* for three different configurations of a robot as shown in Figure 1.2. They drew the deformation map of the robot's workspace and described how the area with highest accuracy can be selected for a machining scenario, hence improving the accuracy of machining [15].

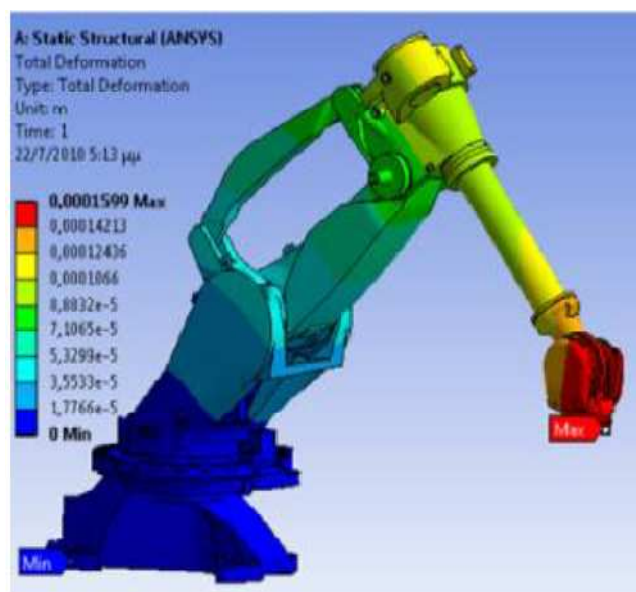


Figure 1.2 Contour of the total deformation [15]

In another project, E. Abele and his group firstly identified the stiffness in the joints and gear as a main cause of overall positional inaccuracy of robot and mentioned that the first three links stiffness had to be considered not only in the direction of motion but also orthogonal to it. They assumed that robot links are stiff and treated the robot as a multi body system. Then, they performed two different implementations for robot modeling, ADAMS and MATLAB, in order

to control the resulting deviations caused by elasticity by offline modifying the trajectories with the joint angle [16]. They considered the backlash of the gears and used spring and damper to model the tilting axis.

1.2.2 Analysis of chatter in machining

Chatter is known as the unstable vibration of the tool with respect to the workpiece during the machining process. It can increase manufacturing costs, reduce the tool life, result in poor dimensional accuracy and surface finish, cause early failure of the cutting tool and damage the machine tools [17]. In order to prevent chatter occurrence, it is usually sufficient to run the machining tasks in compatibility with stability lobes by adjusting spindle speed or depth of cut.

E. Rubio [18] measured the tool vibrations with an inductive sensor and the workpiece with an accelerometer. It was found that measured frequencies are in accordance with the exciting and natural frequencies of the spindle and workpiece-table system, respectively. Also it revealed that acceleration measurements at the workpiece attenuate spindle frequencies, while displacement measurements at the same measurement point attenuate the high frequency peaks of chatter. Velocity measurements, obtained from acceleration data, are good indicators of chatter development because the frequency spectra show the spindle and workpiece vibrations adequately.

In robotic machining, Pan *et al.* emphasized the chatter as an important obstacle to deal with. Low frequency chatter (10 Hz) is observed in robotic machining tasks because the robot is less stiff than a CNC machine but there is not analytical solution for that due to a lack of sensory information. To realize chatter they used a force/torque sensor between the robot wrists and the spindle. They observed that when chatter occurs, the force amplitude increases suddenly as can be seen from FFT of force data. Furthermore, they related the chatter in robotic milling to mode coupling chatter rather than the regenerative one. Finally, some characteristics are derived for chatter phenomena in robotic machining [19]:

- 1- the frequency of chatter is robot based and it is not related to machining parameters. In other words, chatter is related to robot pose, joint orientation and loading. The maximum machining force for robotic applications is around 150N and 50N in parallel and axial direction with respect to cutting direction, respectively.

- 2- when chatter occurs, the entire structure of the robot starts to vibrate.
- 3- the chatter limits are different from one position to another.

Oki *et al.* showed that cutting directions (right-hand and left-hand) affects the cutting quality during robotic machining on account of changing the cutting forces that lead to different deformation in the articulated robot for each cutting condition [20]. In order to reduce the force when machining aluminum they selected a small diameter of end milling tool ($\phi = 3 \text{ mm}$) and realized that the resulted machining frequency is far from the natural frequency of the robot's structure and chatter was never reported.

In another paper [21], Oki *et al.* performed robotic machining with a high and ultra-high speed end mill. They reported that in robotic end milling the cutting force decreased by up to 70% and higher feed rate gained compared to a manufactured fluting machine. At 100000 *rpm* the frequency of fluting machine was close to the forced frequency of cutting (3340 Hz) while low stiffness of the robot had a natural frequency of 25 Hz. Therefore, no chatter occurred.

1.2.3 Deformation Compensation

Motion errors are significant in robotic machining tasks. Two known causes are the deflection under machining force and the robot inherent motion errors (kinematic and dynamic error) which is in the range of 0.1 *mm*.

To measure the deformation and compensate it, first it is necessary to model the stiffness which relates the force applied at the tool tip to the deformation at the tool tip. Experiments were conducted in [17] to identify the joint stiffness parameters and used for a real time compensation method, Figure 1.3.

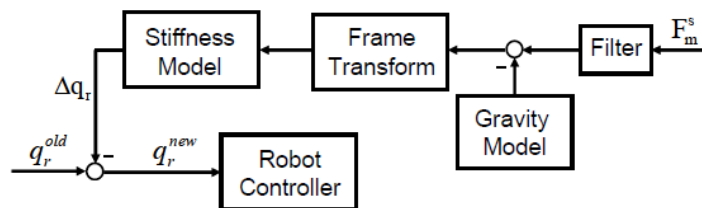


Figure 1.3 Block diagram of real time deformation compensation [17]

In addition, force can be measured by strain gauge sensor fixed on the robot wrist. Finally material removal rate (MRR) can be controlled by adjusting the force. According to Figure 1.4,

by increasing the depth of cut it is possible to keep the force constant while decreasing the feed rate .

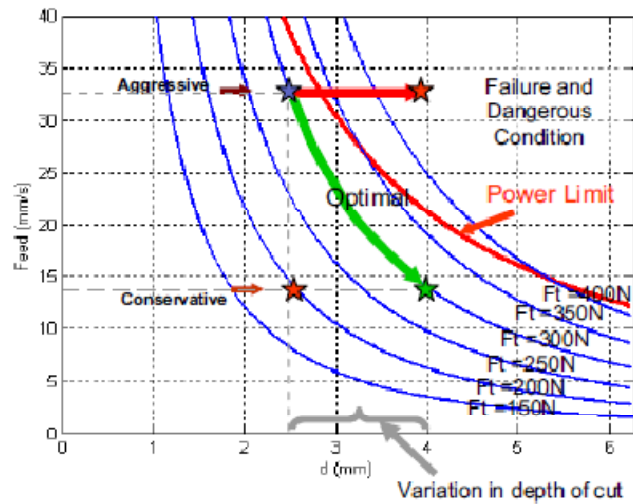


Figure 1.4 Controlled Material Removal Rate (MRR) [17]

Considering the importance of control engineering in machining, G. Ulsoy *et al.* designed and developed different types of controller for CNC machining process [22], In this regard, Wang *et al.* suggested a robust controller to control the MRR in robotic machining tasks [4,17].

The concept of macro/micro manipulator was firstly introduced by A.Sharon in 1988 [23] and is referred to as a large (macro) robot having a small (micro) high-performance robot inside and has been proposed to enhance the functionality of a manipulator. In their system, a five degree-of-freedom micro manipulator (that can accelerate a 22 kg mass at 45 G) was designed, fabricated, and attached to an experimental one-axis robot. They achieved a force-control frequency of 60 Hz that was 32 times higher than the first mode of the robot structure.

As a COMET project [24], funded by the European Commission, using a piezo-actuated high-dynamic micro manipulator in order to compensate for the positioning errors of the robot was reported recently by O. Sornamo *et al.* at Lund university [25]. The spindle was attached to the compensation mechanism and the robot held the workpiece. They experimentally calibrated a black-box model by system identification methods, then, with applying proper on-line control strategy they reduced the structural vibrations and an accuracy of $\pm 15\ \mu\text{m}$ was attained.

1.2.4 Robot calibration

Normally, robots are used in industries for repeatable but low accuracy tasks such as assembly, welding, pick and place and auxiliary machining tasks. Thus they have been designed for high repeatability but low accuracy but in a machining process high precision is needed. To increase the precision during robot-assisted machining, one idea is to calibrate the robot. Robot inaccuracies result from three major sources: geometric errors that come from manufacturing processes, misalignment and joint wear, compliance error because of link deflection and robot's joints and lastly thermal error generated by thermal expansion of robot's links and joints.

The effect of geometric errors, thermal errors and link compliance error on robot positioning accuracy was surveyed by Chunhe Gong *et al.* [26]. In addition, a comprehensive error model for combining geometric errors, position-dependent compliance errors and time-variant thermal errors were derived. Furthermore, a laser tracker has been used to calibrate these errors by an inverse calibration method. It has been observed that the accuracy of robot after calibration improved significantly.

CCD cameras were also used to identify the kinematic parameters of actual machining set up so that positional accuracy of the robot could be improved [27]. Morris *et al.* established a robot calibration method using a coordinate measuring machine (CMM). Experimental measurements of some robot poses are taken using a CMM. Based on the measurements, a kinematic model is developed for the robot arm. Its relationship to the world coordinate frame and the tool is also established [28].

In general, a calibration method should serve two purposes. First, it should establish a relationship between the robot coordinate system and the workpiece coordinate system. Second, it should estimate the kinematic parameters of the robot to accurately describe the actual position and orientation of the robotic links.

H. P. Jawale and his colleagues have conducted research on the effects of backlash and joints clearance on the positional accuracy of serial manipulator [29]. They used a 2R serial manipulator and calculated the maximum error related to backlash and clearances in all the workspace of the robot.

1.2.5 Future research

[30] has proposed some factors in order to advance robotic machining. First, up to now the efficiency of robotic machining has never been studied. Low stiffness and payload limitation will restrict the machining parameters (feed rate, depth of cut, tool diameter) on condition that the machining forces be minimized. This will decrease the material removal rate. Secondly, since different joint configurations have different stiffness, it affects machining efficiency and quality hence it can bring many advantages to have optimal joint configurations based on the machining path. Finally, available industrial robots are configured and designed for transferring and welding tasks. The idea of having a new machining-based configuration will partly lessen the actual low stiffness problem as well as using different robots for finishing and roughing tasks; high-stiffness robot for roughing and low-stiffness for finishing.

1.3 Robotic machining of panels

Regarding the machining of flexible panels, there is not any published article yet. In this case, the flexibility of panel is added to the low stiffness of robot and makes the machining tasks very difficult especially in milling where large forces are induced. It seems inevitable to support and fix the panel as a preliminary condition for machining even though determining the path plan using CAD data appears impossible and imprecise as a result of the panel deformation during machining in the out-of-plane direction.

1.3.1 Background

Currently, large double curvature panels in aerospace industries are machined by chemical method with the environmental disadvantage of producing much slurry, rinsed water and solvents. The eco-friendly alternative for it can be conventional milling but regarding the costs and flexibility, robotic milling is considered the best technology, according to [31], with over 50% reduction in electricity consumption, operation costs and production cycle time, over 16000 tons reduction in produced waste and 20% cost reduction per machined part.

Actually, two commercial solutions have been found. In France, Dufieux industry, within the Green Advanced Panels (GAP) project [32], is using two 6-degrees-of-freedom robotic manipulators to support both sides of the panel at the machining point in order to reach the

required manufacturing tolerances of the panel. Unfortunately, the machining accuracy is obtained through a very long mechanical loop passing through two manipulators and their relative floor mounting, and consequently imposes strong constraints on the accuracy and calibration of each component of the whole machining work cell. Moreover, the overall cost of such a manufacturing system is high Figure 1.5.



Figure 1.5 Using double robot in machining of panels (GAP project) [32]

In Spain, at Mtorres industry, the Torres surface milling is a machine specifically designed to perform mechanically the aircraft skins thickness reduction process which was traditionally executed using chemical milling [33]. This solution includes a vertical 5 axis milling machine, a flexible tooling system plus another column with a 5 axis configuration, located at the back side of the installation, Figure 1.6. It was proposed to machine fuselage or wing skin panels pockets for weight reduction purposes, therefore eliminating the traditional chemical milling process and substituting it with an efficient and environmentally friendly solution.

All three machines work simultaneously. While the tooling machine supports the panel in space, the milling machine performs the surface milling process and the holding machine supports the panel from its backside to avoid panel deflections at the machining location and to measure in real time the actual panel thickness, via a built-in ultrasonic measuring system, in order to keep an accurate final panel thickness.

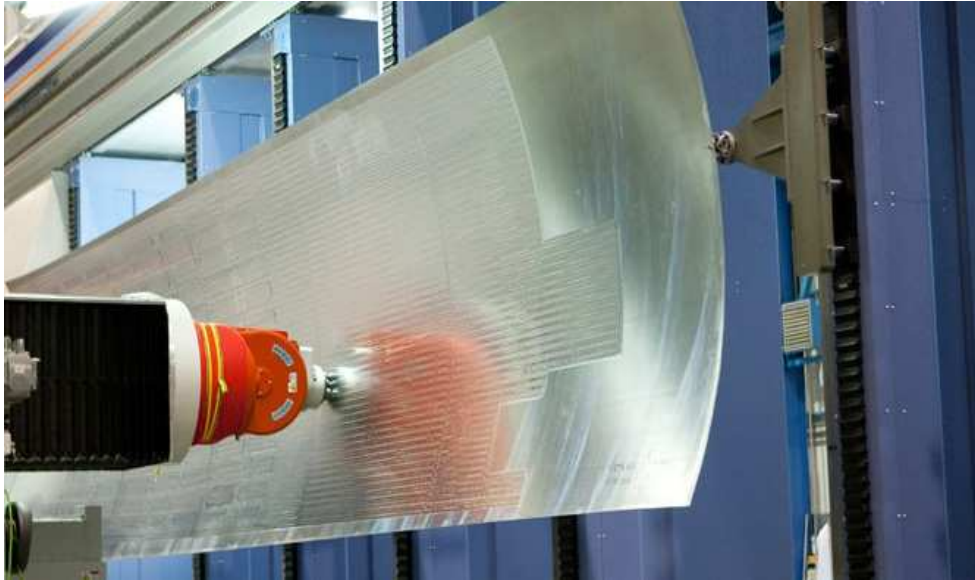


Figure 1.6 Panel milling by torres surface milling machine [33]

A. Chouinard conducted a feasibility study of a special grasping-machining end-effector for the robot, Figure 1.7, which could considerably reduce the demand for extensive hardware normally used for large panel mechanical milling [34]. Moreover, H. H. Roushan designed a new passive mechanism to keep the tool almost perpendicular the surface to be machined [35].

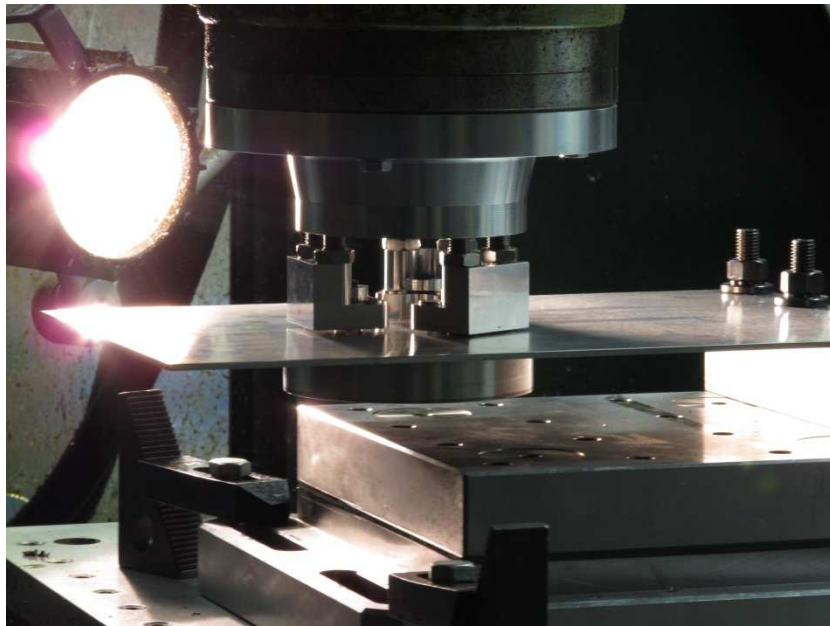


Figure 1.7 Grasping machining end-effector [34]

1.3.2 Patent Review

A search on USPTO², revealed several patents focused on invented machining-related instruments and apparatus. Among them, Giovanni B. Bonomi from *Imta* invented a multi-task end-effector for the articulated head of a CNC Robotic machining center to automate the assembly and integration of parts by means of rivets or similar fasteners, Figure 1.8 and Figure 1.9. It uses a single end-effector attached to the mobile working head of the robot and can accomplish hole preparation, fastener insertion and installation operation at selected location by a pair of aligned tool head connected by a so-called U-shaped frame to each other [36]. Each tool head carries multiple tool drivers adapted to various tools making it highly flexible for different tasks including drilling, deburring and reaming together with fastening operations.

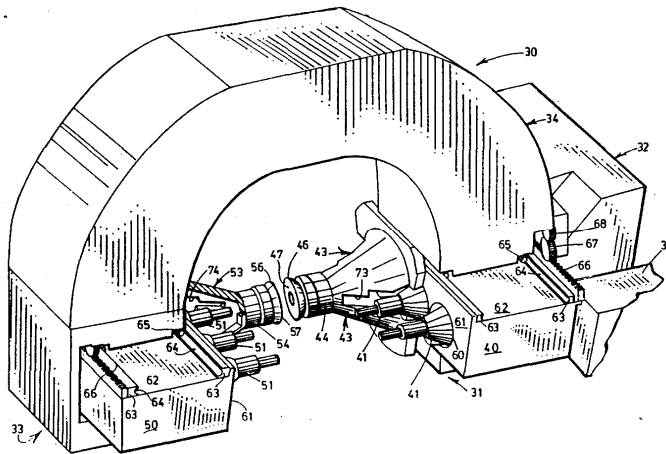


Figure 1.8 C-clamp preliminary idea [36]

²the United States Patent and Trademark Office

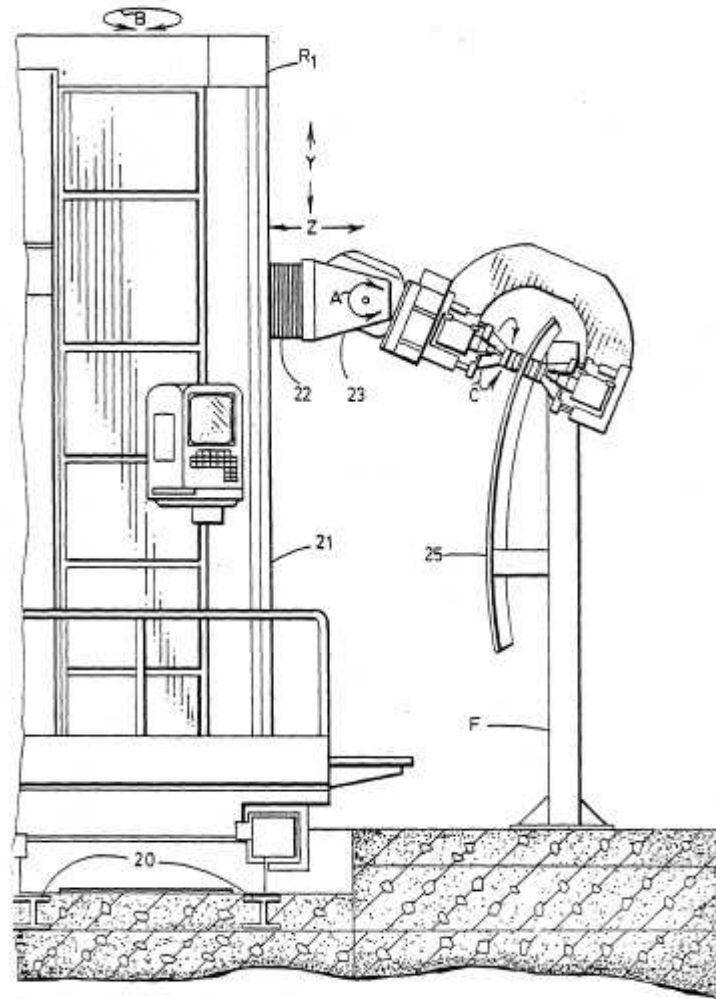


Figure 1.9 Illustration of work cell and robot equipped with an end-effector (C-clamp) [36]

Another patent [37], proposed by the aforementioned inventor, a riveting operation utilizing two mirror robots located opposite sides of the panel was considered where considering riveting tasks, the robots first prepare all rivet holes at successive locations and then returns to each one for insertion and installation of the rivets, Figure 1.10. In order to avoid stress and deformation of the components, fixtures and final assembled part, this new end-effector maintains the symmetrical balance throughout the hole preparation and fastener installation.

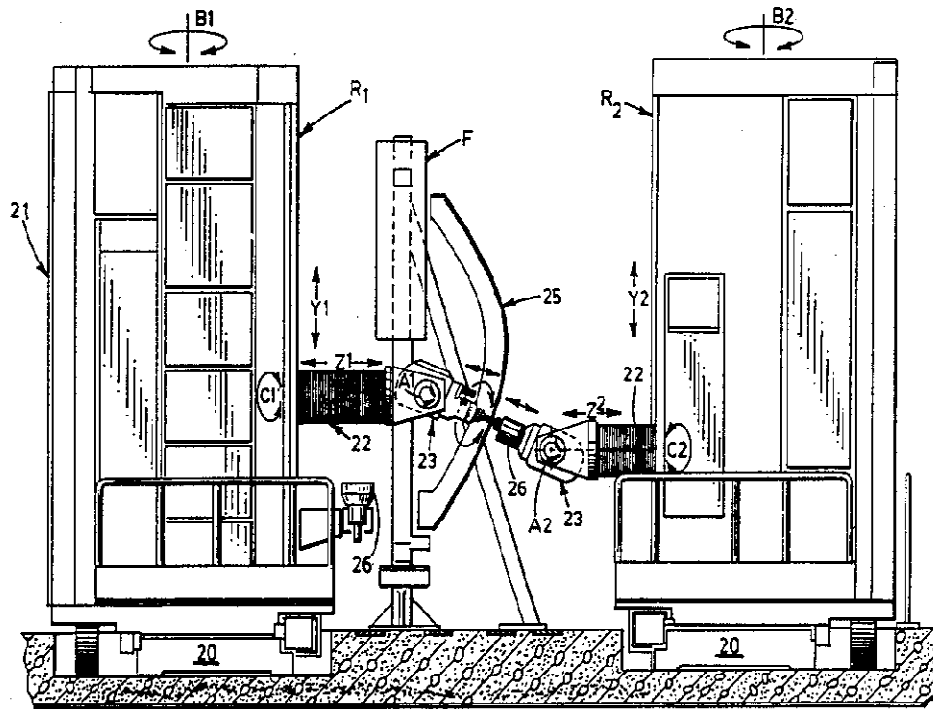


Figure 1.10 Using two mirror robots in fastening operations [37]

Machining of panels as an alternative to electro-discharge machining (EDM) is proposed by Dufieux industry and Airbus [38]. Although expensive, EDM has two disadvantages. First, to clean the panels by removal of masking material used to protect the non-machining area and rinsing, and second, it is not possible to have different depth of cut in a single operation. In this patent, the act of machining a flexible panel, used for aircraft cabins or fuselages, is realized with two mechanisms with at least 5 degree of freedom. One for the machining task and also avoiding panel attraction by tool (avoiding drag phenomenon), no. 59 in Figure 1.11, and another for supporting the panels against machining force and damping the vibration by the sphere made from elastically deformable material capable of rolling on the panel as it is shown in Figure 1.11 (no. 40). The support element (known as retention element), no. 13 in Figure 1.11, is fitted in removable way and can be changed easily.

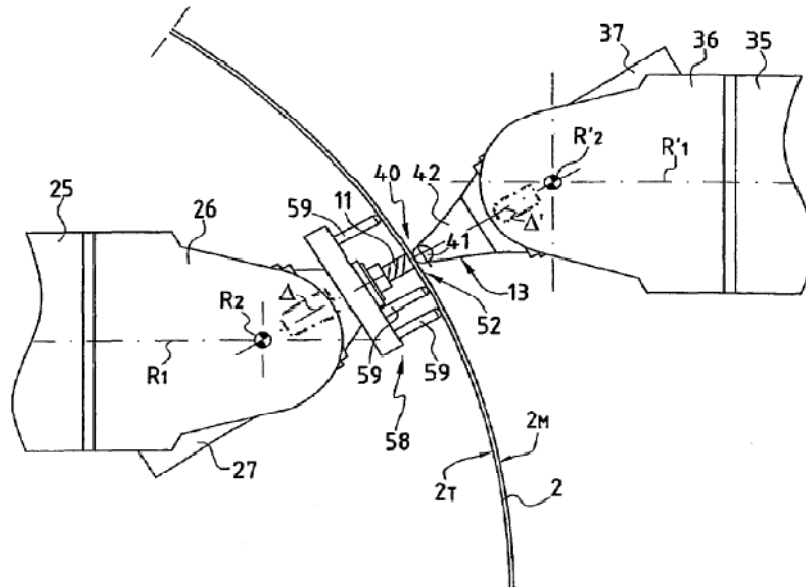


Figure 1.11 Machining of panels by two mechanisms (robots) [38]

Panels of the airplane nose have double curvature made of light alloys like aluminum and are produced by drawing where the surface is in contact with the drawing mold at the internal (concave) surface. Drawing processes produce a plastic deformation throughout the panels which result in non-uniform thickness. Conventional method for machining is to fix the panels by suction cups which lack precise dimensions in other points not taken by cups. To confront this imprecision, a mechanical device for machining of flexible panels with unknown complex shape, such as skin panels of aircraft fuselage, was invented by J. Hamann. The panel is fixed on its peripheral area and includes counterbalancing of applied forces; machining forces on one side of the panel and forces induced by a supporting instrument, in opposite direction of machining force, on the other side of the panel [39].

Figure 1.12 presents the key elements of the suggested machining process. No.1 is a flexible panel for an aircraft fuselage formed by drawing and necessarily with thickness variations. According to Figure 1.12, surface *1a* is in contact with the drawing mold and with known geometry and surface *1b* is the external surface of the fuselage. The Panel is subjected to machining in *1a* surface with respect to *1b* as reference surface.

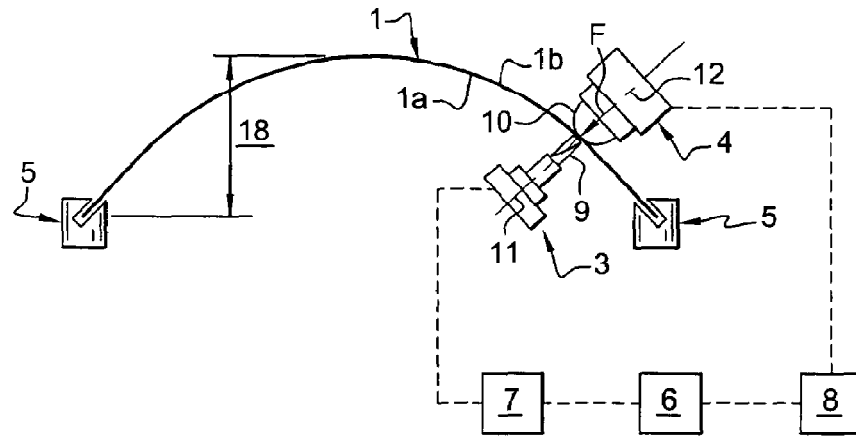


Figure 1.12 A schematic view of the machining process [39]

Owing to thickness variations, it is clear there is a problem in milling specially in pocketing when the bottom depth (e in Figure 1.13) has to seek a very tight tolerance ($< 0.2 \text{ mm}$) compared to the size of the panel (10 m^2). This problem can be solved by using support (No.4) opposite the cutting tools (No.9) while the panel is held by a gripper (No. 5). The tools and support are connected to each other by programmed numerical control (No. 6) where displacements of tools and support are calculated in No.7 and No.8 respectively.

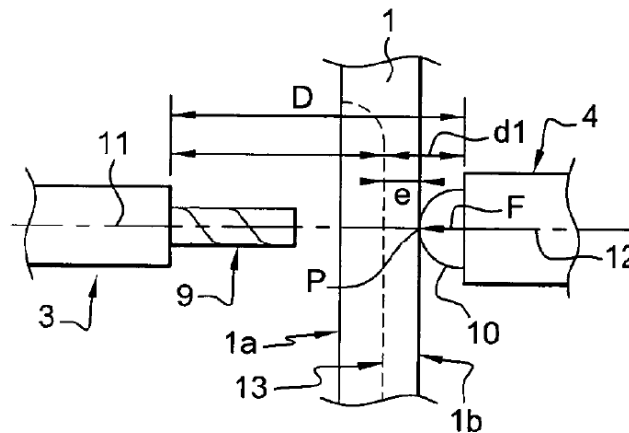


Figure 1.13 Partial cross-sectional view of producing a recess [39]

During the machining, the sphere, No. 10 in Figure 1.13, is in constant contact with the surface $1b$ and causes an elastic deformation in it. Knowing the distance D and setting the distance $d1$ in the numerical controller, the position of tool and support (No. 4) can be defined relatively in order to reaches to $d1$, independent of thickness variations, hence the precision of e can be

maintained. To precisely machine complex panels, in [40], the above inventor designed a new device to eliminate the positioning problem in machining of thin panels.

1.4 Literature Review Conclusion

According to the papers reviewed in this section, the main impediment in robotic machining is related to the low stiffness of the robot with respect to a conventional CNC machine tool. It is recommended to run the machining operations considering related stability lobs which leads to decreasing of the efficiency of the tasks. In pocket machining of large flexible panels, locally support of the panels subject to machining is necessary. In mirror machining the other side of the panel is supported by another robot which moves synchronously with the one carries the tool. Actually two Commercial versions of mirror machining are available even though the total cost of the equipment used is very high. Another solution for panel machining is using a U-shaped end-effector [36]. It was introduced as a multi-tasks end-effector for fastening operation but not for milling. This project is applying the idea of the U-shaped frame (C-frame) to the milling operation. To support the panel against the machining force the idea of using ball is adopted [38,39].

CHAPTER 2 DESIGN AND IMPLEMENTATION

This chapter describes the use of laser beam passing through optical elements to measure the deflection. In addition to explaining this metrology frame elements, characteristics and functions in current research continued by necessary electrical circuit to map from photodiode space to voltage space.

As seen in the first chapter, a number of patents dealing with robot-related machining and auxiliary machining processes provide some conceptual ideas, as a prerequisite, to the design of a C-frame. The industrial requirement is to mill the large panels, up to 2.5 m in width and 8 m in length, which impose a certain constraint to the design. The dimensions of the C-frame have to be enough large to cover the surface of the panels with different size and curvature. One side of the C-frame which is attached to the robot bears total load including weight of the C-frame and applied machining force. The other side supports the panel against machining force. Then, using FEM analysis the amount of deflections and stresses in the proposed C-frame are calculated which give some indication of the range and amplitude of deflection in the C-frame. With these information in hands, a metrology frame is designed and tested.

Since laser can be used for non-contact distance measurement for the largest possible range [41] it is proposed to measure the momentary deflection resulting from machining forces. A metrology frame [42], is designed but instead of using an interferometer it uses a position sensing detector (PSD) which is based on detecting the position of a laser beam through a spot on a photodiode surface due to the applied machining force.

2.1 Proposed solution (mechanical design)

To overcome the aforementioned difficulties in robot assisted machining while meeting the required tolerance and in order to eliminate using two robots on the one hand, and the environmental effects of chemical milling on the other hand, as well as slow rate, costs and time consuming process of electro-discharge machining, current study is beneficial of using a novel end-effector to do the milling task on large and flexible panels with complex shape and double curvature.

2.1.1 Conceptual design

By reviewing some patents, some helpful ideas are adopted. Utilizing a C-clamp is derived from [36] and employing the ball phenomena to support the plate subjected to machining is extracted from [39] and adapted to the new design. Then, as is shown in Figure 2.1, a new C-clamp is conceptually designed and then its features and dimensions was completed utilizing CATIA software, Figure 2.2 and Figure 2.3.

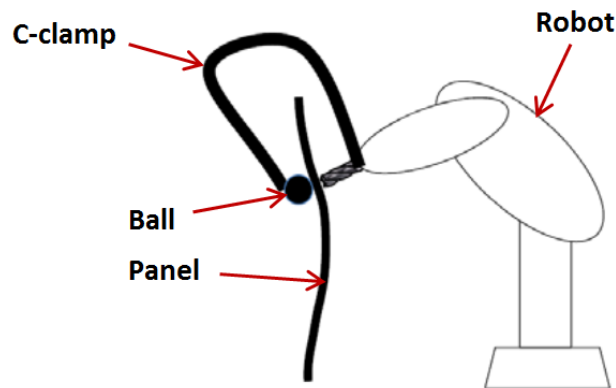


Figure 2.1 Conceptual schematic of C-frame based robotic machining

In order to machine the panel, two separate motions are necessary. Firstly, in-plane motion which is provided by CAD data of the panel as a path plan for the robot. Secondly, out-of-plane motion which is obtained by the end-mill embedded in the robots. The second motion is normal to the plane and affects the pocket floor thickness and is more critical than the first one.

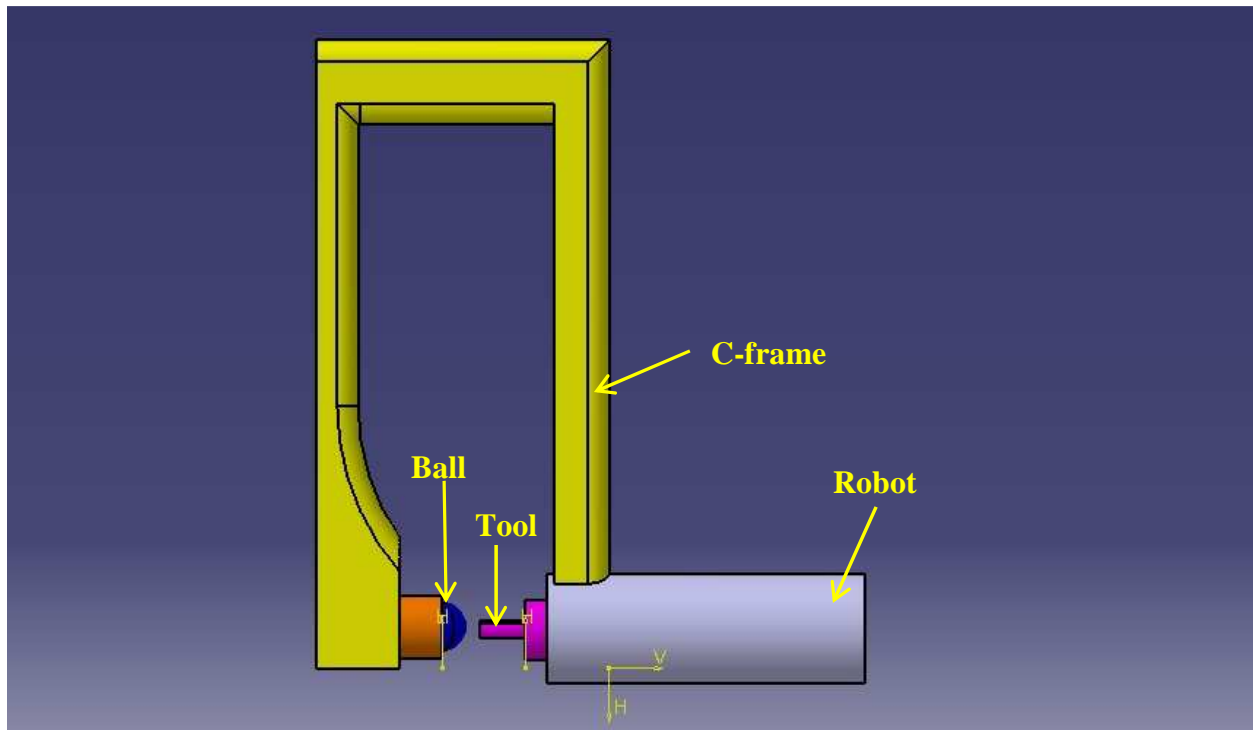


Figure 2.2 Conceptual design of C-frame

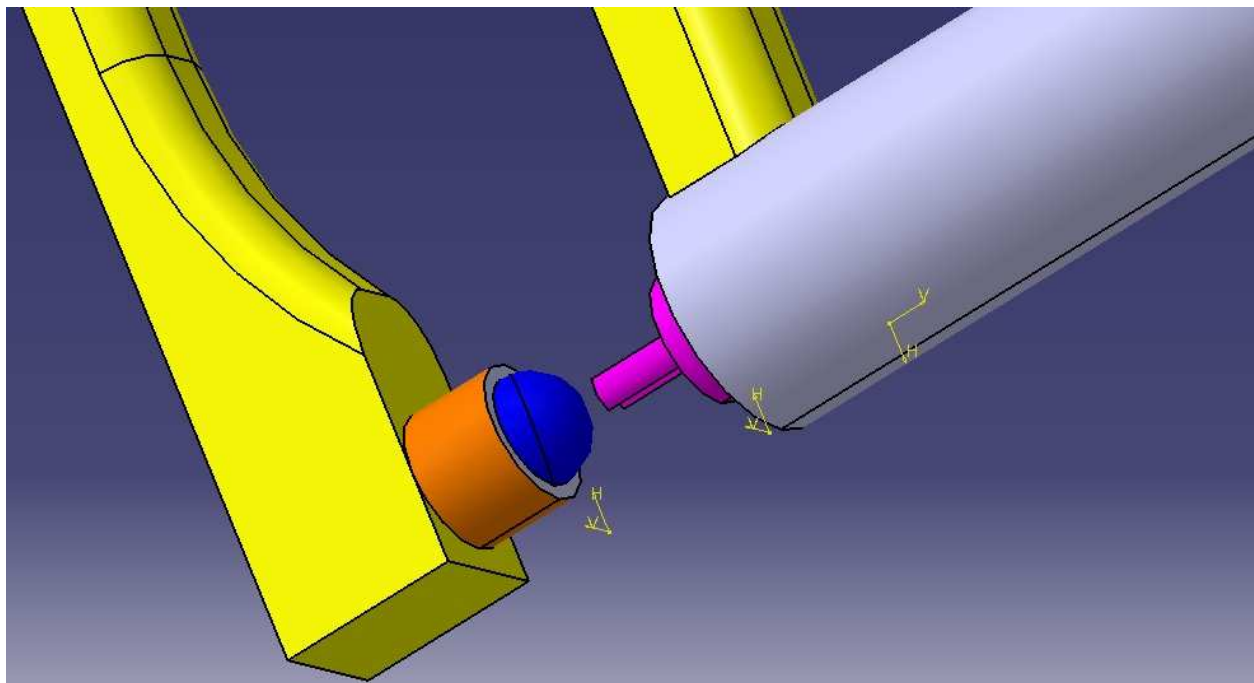


Figure 2.3 Placing of tool and support in C-frame

2.1.2 Finite Element Analysis (FEA) of C-frame

In order to realize the range of deflection for the proposed C-frame, the stresses and strains in the C-frame are calculated by FEA. Assuming panels of around 2.5 m in width calls for a C-frame of 1.3 m dimension in length. An Isometric view of the C-frame is presented in Figure 2.4 and the detailed dimensions are given in Appendix A.

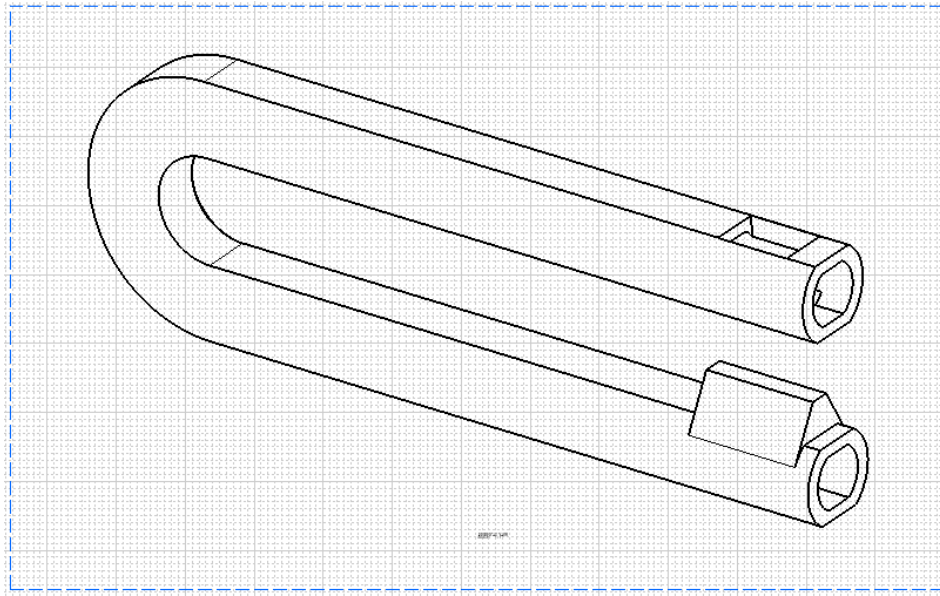


Figure 2.4 3D view of C-frame

To establish the FEM, the machining force is taken as 300 N , according to [17], and the area subjected to this force is 0.00624 m^2 resulting in 50 Kpa pressure as input of the FEM simulation and the rectangular hole in the upper arm is taken as support, Figure 2.4. The material is aluminum ($\sigma_{yield} = 225\text{ Mpa}$) and the C-frame has a 65 kg weight. As is clear from Figure 2.5, the maximum stress is around 1 Mpa in the so called critical zone. This area has the most stress concentration with respect to other area but even then it is completely safe regarding the material of the C-frame.

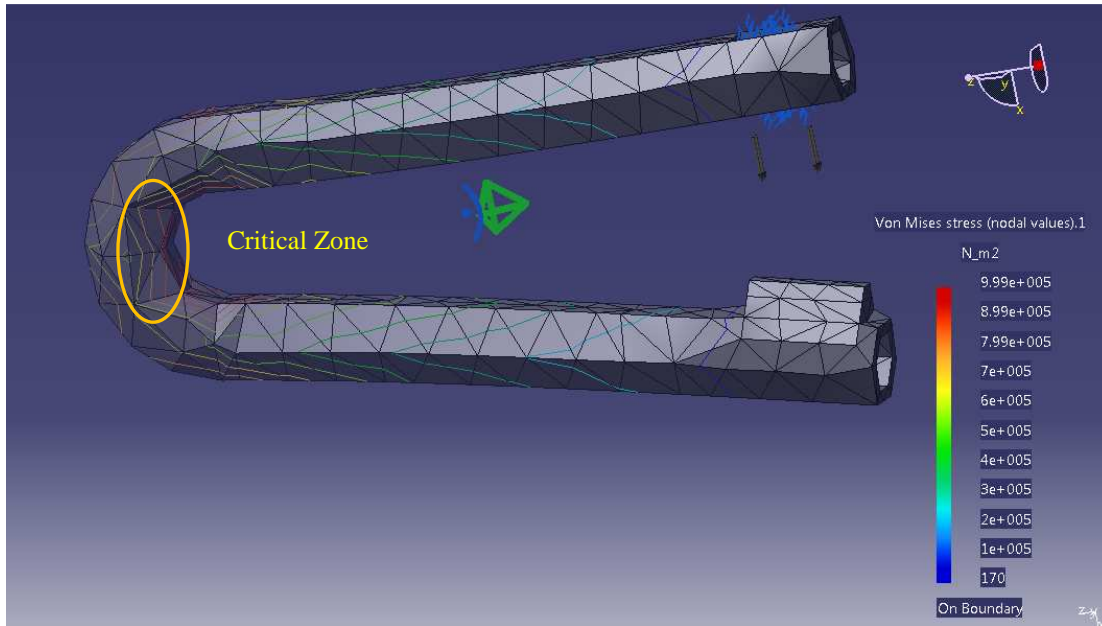


Figure 2.5 Deflection in opposite sides together with nodal stress values

Looking at nodal displacements shows that the maximum displacement occurs where the force is applied and decreases gradually to zero at the support Figure 2.6. As is seen from the colour band, the maximum displacement is around 0.26 mm giving this key information about the range of deflection in the lower arm. The metrology frame will be designed to measure this range of deflection.

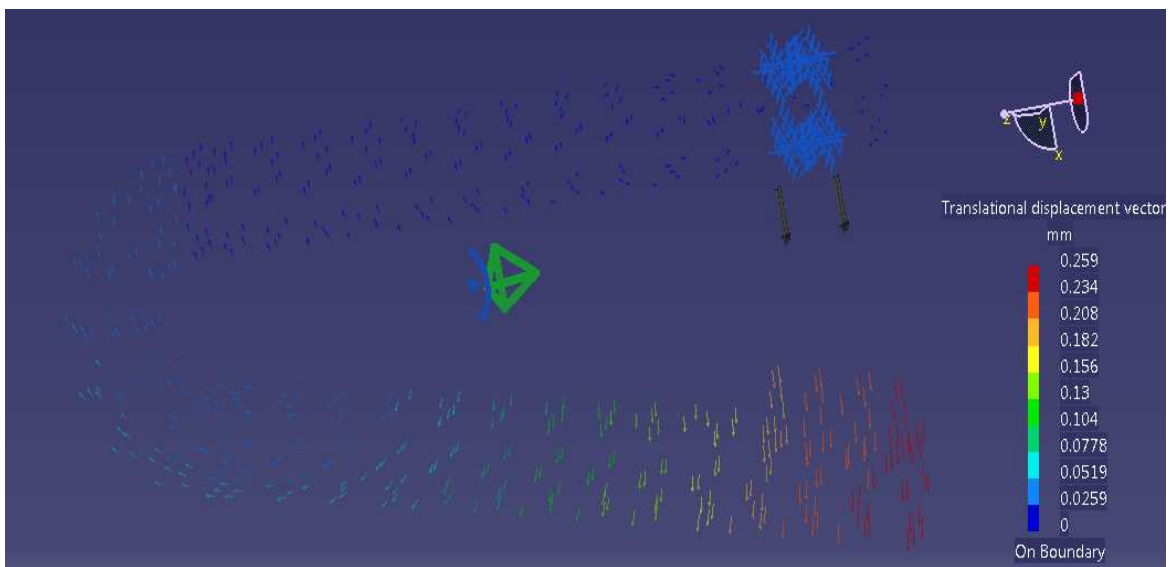


Figure 2.6 Range of displacement in C-frame because of machining force

2.2 Design of metrology frame

The concept of a metrology frame is used to separate the measurement systems from the effects of mechanical deformation and so isolate the measuring system from deformation-based errors due to thermal, static and dynamic loads to improve overall accuracy. J. F. Cuttino *et al.* have designed a three-dimensional non-contacting metrology frame (interferometry) to measure the position and orientation of an object in space using three position sensors and three laser beams [42]. They used forward kinematic to relate the incident beam positions and the six degree of freedom of the object. In [43], S. Moylan and D. Hong used a metrology frame to measure the position of the tool tip with respect to the workpiece while minimizing Abbe errors in a 3-axis milling machine (MMMTs). Since machine tools displacement measurement sensors are subjected to deformation which result in positioning errors, using a separate metrology frame bypasses these errors and improves the accuracy of the tool positioning.

Laser trackers are devices that accurately measure the position of large objects by determining the positions of optical targets held against those objects [44]. J. R. Rene Mayer [41] designed polarization optics to measure the 3-D positions of a target using laser tracking.

It is possible also to measure the position of a target by measuring the displacement of a beam spot on a position sensitive detectors (PSD) [45]. I. A. Ivan compared the performance of PSDs against a CCD camera by mounting a beamsplitter between the PSD and an object providing an alternative for the CCD camera and found that the PSD was very suitable to replace the expensive camera [46].

2.2.1 Conceptual design

Figure 2.7 shows the optical design of the metrology frame. The actual distance between lower and upper arm (d) is sought. Any deflection induced by machining force will affect this distance and will be sensed by position detector and its output can then be used directly to compensate the deflection.

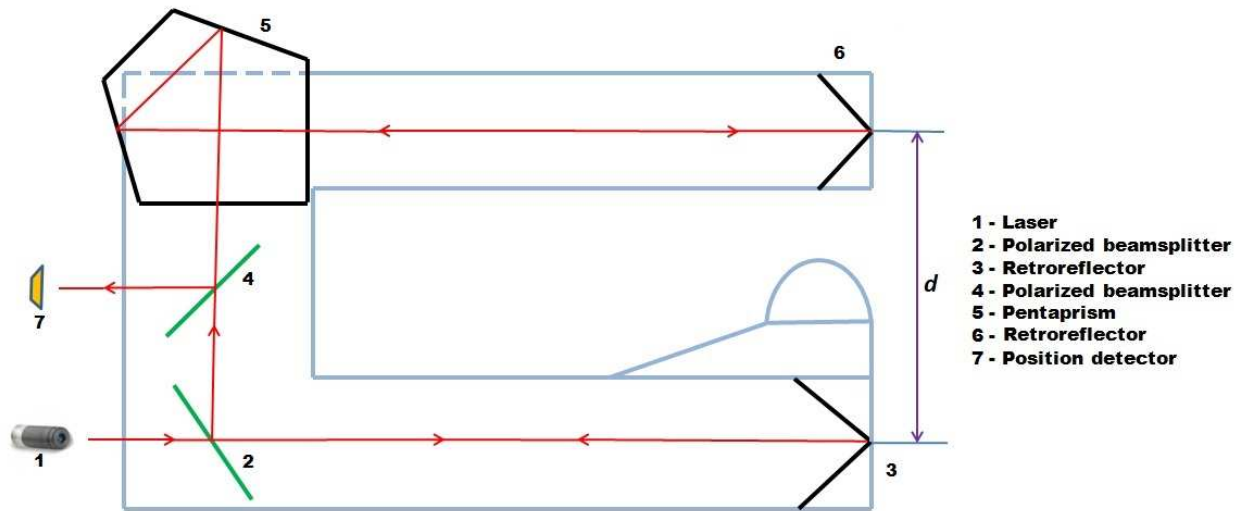


Figure 2.7 Conceptual metrology frame

In addition to the beam guiding aspect, another issue is light polarization when it passes through elements to ensure efficient management of the light intensity. Such which will be explained in detail in the following sections lead to the design shown in Figure 2.8.

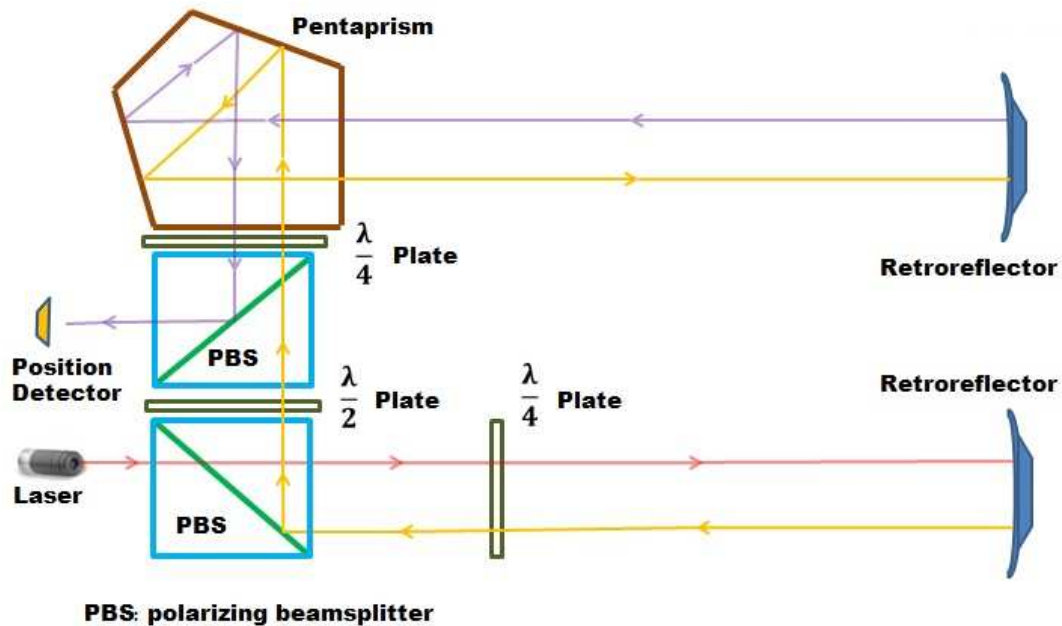


Figure 2.8 Using quarter and half wave plate to control light polarization

2.2.2 Elements of metrology frame and their functions

The proposed metrology frame consists of optical elements arranged to deliver the desired round beam with sufficient intensity at the photodetector.

2.2.2.1 Laser source

A laser diode module as a kind of solid state lasers is used for its low cost and compactness. The solid state laser uses a solid crystalline material as the lasing medium and is electrically pumped (as an excitation mechanism) [47].

Laser light has several specific characteristics: firstly, it is coherent which means that different parts of laser light are related to each other in phase, in space and in time. Secondly, the light from a laser typically comes from one atomic transition with a single precise wavelength. Hence, laser light consists of essentially one wavelength and is known as monochromatic. Thirdly, the light from a laser emerges in an extremely narrow beam and can easily be collimated [48].

Light is a transverse electromagnetic wave so the electric (and magnetic) field oscillates in a direction transverse to the direction of propagation. From a polarization viewpoint, the light is classified in three groups. As it is shown in Figure 2.9, a plane electromagnetic wave is said to be linearly polarized. The transverse electric field wave is accompanied by a magnetic field wave as illustrated in Figure 2.9. The electric field direction defines the polarization of light.

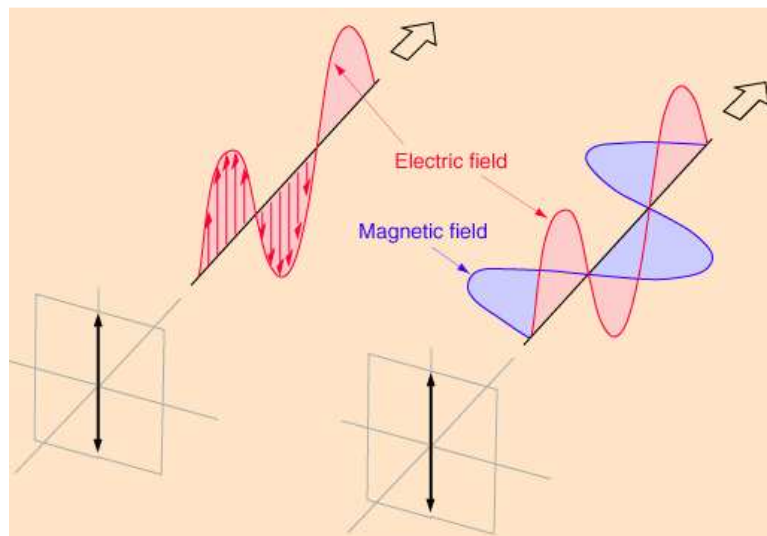


Figure 2.9 Linearly polarized light [48]

Circularly polarized light consists of two perpendicular electromagnetic plane waves of equal amplitude and phase difference of a quarter wave (90°). The light illustrated in Figure 2.10 is right- circularly polarized. The tip of the electric field vector is moving in a circle.

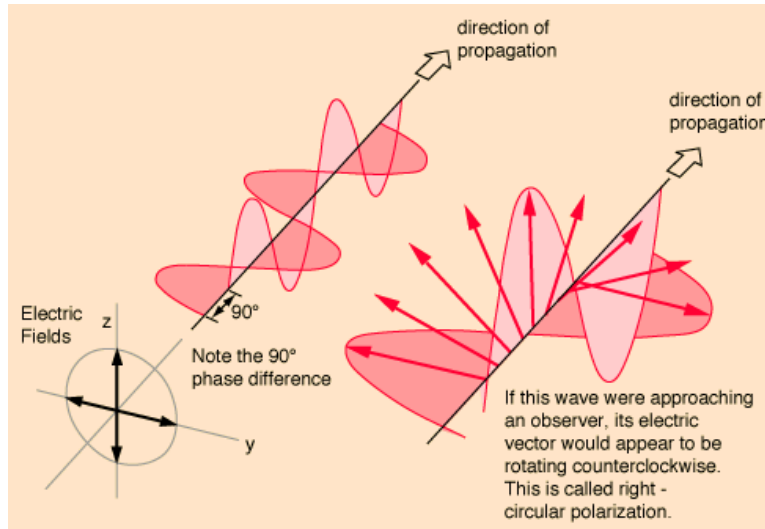


Figure 2.10 Circularly polarized light (just electrical fields are shown) [48]

Finally, according to Figure 2.11, elliptically polarized light consists of two perpendicular waves of unequal amplitude which differ in phase by 90° . The illustration shows right- elliptically polarized light.

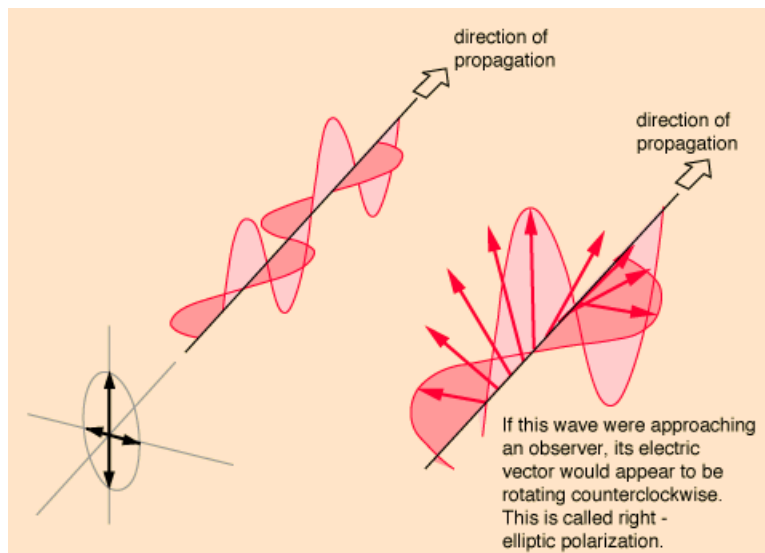


Figure 2.11 Elliptically polarized light (just electrical fields are shown) [48]

Another important definition evaluating divergence of a laser beam is pointing stability ($\frac{mrad}{^{\circ}C}, \frac{\mu m}{^{\circ}C}$) and in general case is around 30-40 $\frac{\mu m}{^{\circ}C}$, and the smaller one indicate the divergence is less so the beam is better collimated.

In this project, The CPS180 laser diode module is selected which is visible red light and withstand large temperature variations. It maintains an Optical-to-Mechanical alignment better than 20 *mrad*. Other Features are: a collimated laser diode module, round shape with beam diameter of 4 *mm*, lasing at 635 *nm*, power of 1 *mW* and divergence ≤ 1.8 *mrad* [49].

2.2.2.2 Polarizing beamsplitter (PBS)

A polarizing beamsplitter splits the light into *S* and *P* polarization components by reflecting the *S* component by 90° at the dielectric beamsplitter coating, while allowing the *P* component to pass through. Mounting the beamsplitting surface at a 45°, around the beam axis, causes 50% of the light to reflect and the remaining 50% to pass (Figure 2.12). Cube beamsplitters are constructed by cementing two precision right angle prisms together with appropriate interference coating on the hypotenuse surface which has to be compatible with the wavelength of the input light.

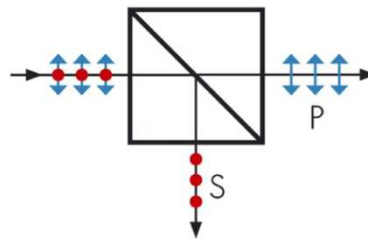


Figure 2.12 Polarizing beamsplitter [50]

2.2.2.3 Waveplates

Wave plates consists of a carefully adjusted thickness of a birefringent material such that the light associated with the larger index of refraction (fast axis) is retarded by 90° (a quarter wavelength) in phase with respect to that associated with the smaller index (slow axis which is perpendicular to the fast axis). The phase shift or retardance increases with the thickness and with appropriate choice of thickness any degree of retardance may be achieved. The most popular of retarders are quarter and half wave plates.

Quarter Wave Plates (QWPs) are designed to change the polarization of a beam from linear to circular or elliptical and vice versa. If the Fast axis of QWP is at 45° with respect to the optic axis (direction of linearly polarized input light), the output is circularly polarized, Figure 2.13 .

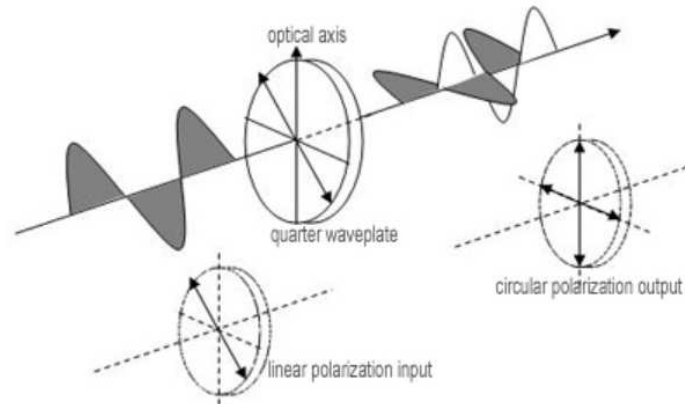


Figure 2.13 Using QWP to change the polarization of light [48]

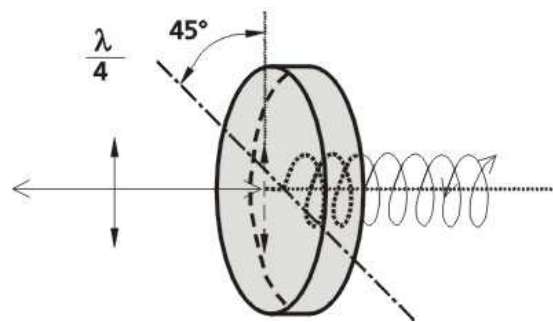


Figure 2.14 Using QWP to change the polarization of light [51]

As shown in Figure 2.14, if linearly polarized light is incident on a quarter-wave plate at 45° to the optic axis, then the light is divided into two equal electric field components. One of these is retarded by a quarter wavelength by the plate which produces circularly polarized light.

Half Wave Plates (HWPs) rotate the linearly polarized light to any desired orientation. As illustrated in Figure 2.15, the rotation angle is twice the angle between the incident polarized light and optical axis.

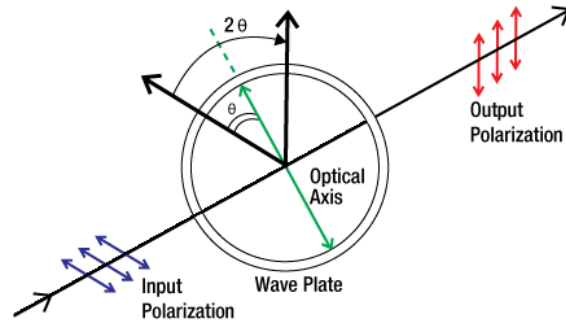


Figure 2.15 Changing the orientation of a linearly polarized light by HWP [52]

A zero order air-spaced wave plate with 25.4mm diameter is used which have broad bandwidth, lower sensitivity to temperature and wavelength changes.

2.2.2.4 Pentaprism

According to Figure 2.16, pentaprisms are used to define right angles in optical systems. It deviate the light by 90° (without any inverting or reversing). Pentaprisms are five-sided prisms unaffected by slight movements. The deviation angle of 90° is independent of any small rotation of the prism about an axis parallel to the line of the intersection of the two reflecting faces.

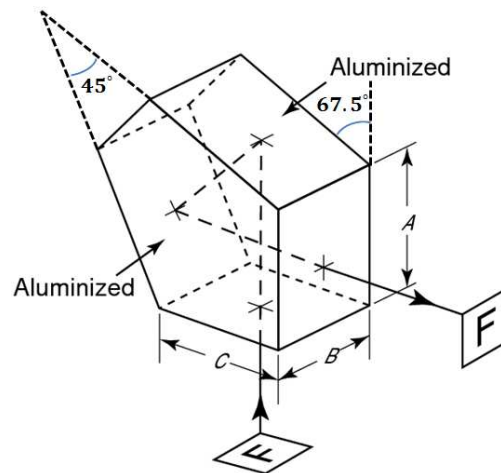


Figure 2.16 Pentaprism used to change the direction of the light by 90° [53]

The selected pentaprism has sides of A , B and C have equal dimensions of 40 mm .

2.2.2.5 Retroreflector

A retroreflector is an optical component combining three reflecting surfaces which are mutually perpendicular. The light entering a retroreflector is reflected back 180° towards its direction of origin and parallel to the original beam, regardless of its orientation and rotation Figure 2.17.

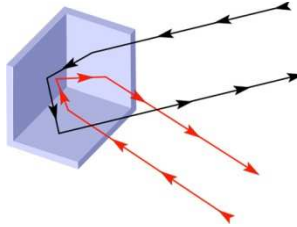


Figure 2.17 Retroreflector is composed of three perpendicular reflecting faces [54]

With regard to Figure 2.18, the reflected image is both inverted and reversed. However, unless the incident and reflected beams strike the exact center of the optic, they will not overlap but rather be shifted with respect to each other. For example, if the incident beam strikes the optic 3 mm to the right of the center, the retroreflected beam will emerge 3 mm to the left of the center.

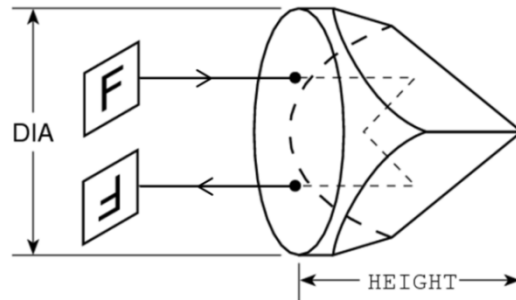


Figure 2.18 Retroreflector invert an image while inverting [55]

2.2.3 Optical assessments of laser beam by Jones matrix

Evaluating the polarization of the beam while it passes from one optical elements to another, helps to produce a round and Gaussian light with sufficient intensity at the photodetector surface. Jones calculus is a mathematical technique for analyzing the changes in the polarization state of a laser beam when it passes through optical component [56].

According to Jones calculus and considering that the beam propagates in the z direction, the light can be represented by its electrical field vector (E):

$$\vec{E} = \begin{bmatrix} E_x \\ E_y \end{bmatrix} \quad (1)$$

where E_x and E_y are the instantaneous scalar component amplitude of the electrical field.

$$\vec{E} = E_{0x}e^{i(kz-\omega t+\varphi_x)}\hat{x} + E_{0y}e^{i(kz-\omega t+\varphi_y)}\hat{y} = \vec{E}_0 e^{i(kz-\omega t)} \quad (2)$$

and

$$\vec{E}_0 = E_{0x}e^{i\varphi_x}\hat{x} + E_{0y}e^{i\varphi_y}\hat{y} = \begin{bmatrix} E_{0x}e^{i\varphi_x} \\ E_{0y}e^{i\varphi_y} \end{bmatrix} = \begin{bmatrix} \vec{E}_{0x} \\ \vec{E}_{0y} \end{bmatrix} \quad (3)$$

\vec{E}_0 is called a Jones vector and is a complex amplitude containing all polarization information. The state of polarization of light is completely determined by the relative amplitudes (E_{0x}, E_{0y}) which often are expressed in normalized form and the relative phases $\Delta = \varphi_y - \varphi_x$ of these components.

In most of cases, linear and circular polarization are considered, the representation of Jones vector are calculated below. Figure 2.19 shows a horizontally polarized light. The Jones vector is:

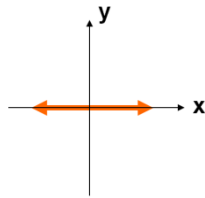


Figure 2.19 Horizontally polarized light

$$\vec{E}_0 = \begin{bmatrix} \vec{E}_{0x} \\ \vec{E}_{0y} \end{bmatrix} = \begin{bmatrix} E_{0x}e^{i\varphi_x} \\ E_{0y}e^{i\varphi_y} \end{bmatrix} = \begin{bmatrix} A \\ 0 \end{bmatrix} = A \begin{bmatrix} 1 \\ 0 \end{bmatrix} \quad (4)$$

And for circularly polarized, supposed E_y leads E_x , the Jones vector becomes:

$$\vec{E}_0 = \begin{bmatrix} \vec{E}_{0x} \\ \vec{E}_{0y} \end{bmatrix} = \begin{bmatrix} E_{0x}e^{i\varphi_x} \\ E_{0y}e^{i\varphi_y} \end{bmatrix} = \begin{bmatrix} A \\ Ae^{i\frac{\pi}{2}} \end{bmatrix} = A \begin{bmatrix} 1 \\ i \end{bmatrix} \xrightarrow{\text{after normalization}} = \frac{1}{\sqrt{2}} \begin{bmatrix} 1 \\ i \end{bmatrix} \quad (5)$$

According to Jones calculus, all possible polarization states of light are given in Table 2.1:

Table 2.1 Jones vector representing polarization states [56]

Linearly polarized in horizontal (x)	$\begin{bmatrix} 1 \\ 0 \end{bmatrix}$
Linearly polarized in vertical (y)	$\begin{bmatrix} 0 \\ 1 \end{bmatrix}$
Linearly polarized at $\pm 45^\circ$	$\frac{1}{\sqrt{2}} \begin{bmatrix} 1 \\ \pm 1 \end{bmatrix}$
Linearly polarized at any angle (θ) N.B. θ is measured with respect to x	$\begin{bmatrix} \cos \theta \\ \sin \theta \end{bmatrix}$
Right-handed circularly polarized	$\frac{1}{\sqrt{2}} \begin{bmatrix} 1 \\ -i \end{bmatrix}$
Left-handed circularly polarized	$\frac{1}{\sqrt{2}} \begin{bmatrix} 1 \\ i \end{bmatrix}$

Another application of Jones calculus is deriving the Jones matrix of optical devices, in order to follow the light polarization states while passing through them. In this regard, according to [58], Jones matrix for mostly used optical devices is in table 2.2.

Table 2.2 Jones matrix of common optical elements [56]

Polarized beamsplitter - transmission	$\begin{bmatrix} 1 & 0 \\ 0 & 0 \end{bmatrix}$
Polarized beamsplitter- reflection	$\begin{bmatrix} 0 & 0 \\ 0 & 1 \end{bmatrix}$
Polarized beam splitter (θ is the angle between input and output light)	$\begin{bmatrix} \cos^2\theta & \sin\theta \cos\theta \\ \sin\theta \cos\theta & \sin^2\theta \end{bmatrix}$
Quarter wave plate – fast axis horizontal	$\begin{bmatrix} 1 & 0 \\ 0 & i \end{bmatrix}$
Quarter wave plate – fast axis vertical	$\begin{bmatrix} 1 & 0 \\ 0 & -i \end{bmatrix}$
Quarter wave plate – fast axis at $\pm 45^\circ$	$\frac{1}{\sqrt{2}} \begin{bmatrix} 1 & \pm i \\ \pm i & 1 \end{bmatrix}$
Quarter wave plate - θ is the angle between fast axis and optical axis	$\begin{bmatrix} \cos^2\theta + i \sin^2\theta & (i-1)\sin\theta\cos\theta \\ (i-1)\sin\theta\cos\theta & \sin^2\theta + i \cos^2\theta \end{bmatrix}$
Half wave plate – fast axis horizontal	$e^{-i\frac{\pi}{2}} \begin{bmatrix} 1 & 0 \\ 0 & -1 \end{bmatrix}$
Half wave plate – fast axis vertical	$e^{i\frac{\pi}{2}} \begin{bmatrix} 1 & 0 \\ 0 & -1 \end{bmatrix}$
Half wave plate – fast axis at $\pm 45^\circ$	$\begin{bmatrix} 0 & 1 \\ 1 & 0 \end{bmatrix}$
Half wave plate – fast axis at θ from optical axis	$\begin{bmatrix} \cos 2\theta & \sin 2\theta \\ \sin 2\theta & -\cos 2\theta \end{bmatrix}$
Pentaprism	$\begin{bmatrix} 1 & 0 \\ 0 & 1 \end{bmatrix}$
Retroreflector	$\begin{bmatrix} 1 & 0 \\ 0 & -1 \end{bmatrix}$

As a general procedure, when the optical element rotates at θ :

$$\mathcal{M}(\theta) = \mathcal{R}(-\theta) \mathcal{M}_0 \mathcal{R}(\theta) \quad (6)$$

where $\mathcal{M}_0 = \mathcal{M}(\theta = 0)$ is the Jones matrix of optical component and $\mathcal{R}(\theta)$ is a rotation matrix:

$$\mathcal{R}(\theta) = \begin{bmatrix} \cos\theta & \sin\theta \\ -\sin\theta & \cos\theta \end{bmatrix} \quad (7)$$

In real cases, it is needed to model the effects of more than one component on the polarization states, in such cases it is enough to multiply all of the Jones matrix of the optical elements from last to first by the Jones vector of input light.

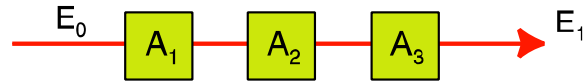


Figure 2.20 Effects of several components on the polarization state

As it is demonstrated in Figure 2.20, the resulting polarization state (E_1) is:

$$E_1 = A_3 A_2 A_1 E_0 \quad (8)$$

In the present research, the Jones calculus is applied to all metrology elements to analyze the polarization of the light passing over optical elements, starting with the linearly polarized light is produced by the laser diode.

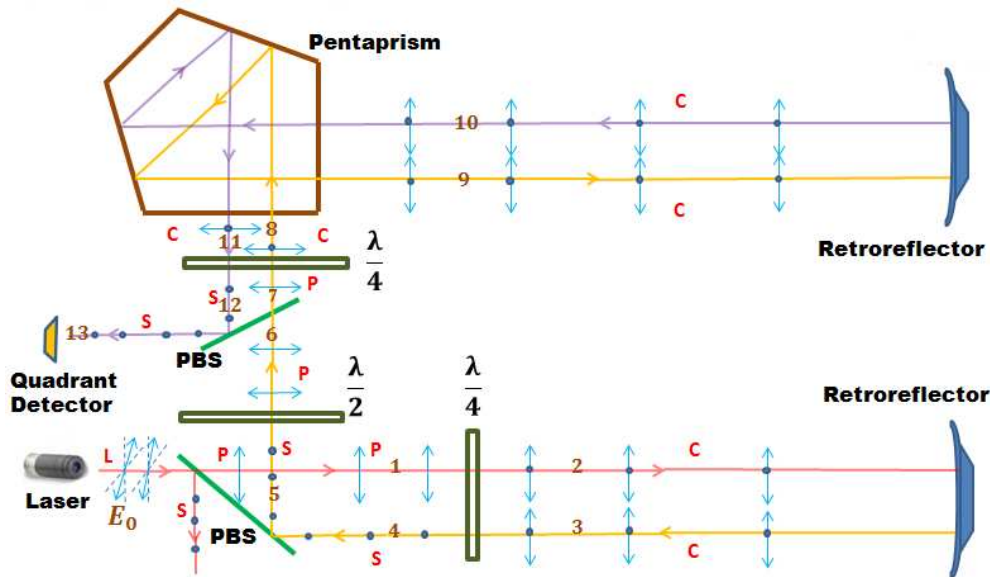


Figure 2.21 Nominal state of polarization in C-frame (c: circular, s: s-polarized, p: p-polarized)

Figure 2.21 shows the nominal state of polarization before and after each optical component. The polarization of output beam at the photodetector (location 13) is calculated below:

$$E_{13} = J_{\text{PBS}(90)} J_{\text{QWP}(-45)} J_{\text{Penta}} J_{\text{Retro}} J_{\text{Penta}} J_{\text{QWP}(+45)} J_{\text{PBS}(0)} J_{\text{HWP}(+45)} \\ \times J_{\text{PBS}(90)} J_{\text{QWP}(-45)} J_{\text{Retro}} J_{\text{QWP}(+45)} J_{\text{PBS}(0)} E_0 \quad (9)$$

The result is $\begin{bmatrix} 0 \\ 1 \end{bmatrix}$, s-polarized, that is linearly polarized light but vertically. The detailed calculation code is attached in Appendix B.

2.3 Implementation

Following the optical and stress analysis of the C-frame, a solid model was developed using CATIA software (Figure 2.22) as a preliminary step to the test bench implementation as shown in Figure 2.23.

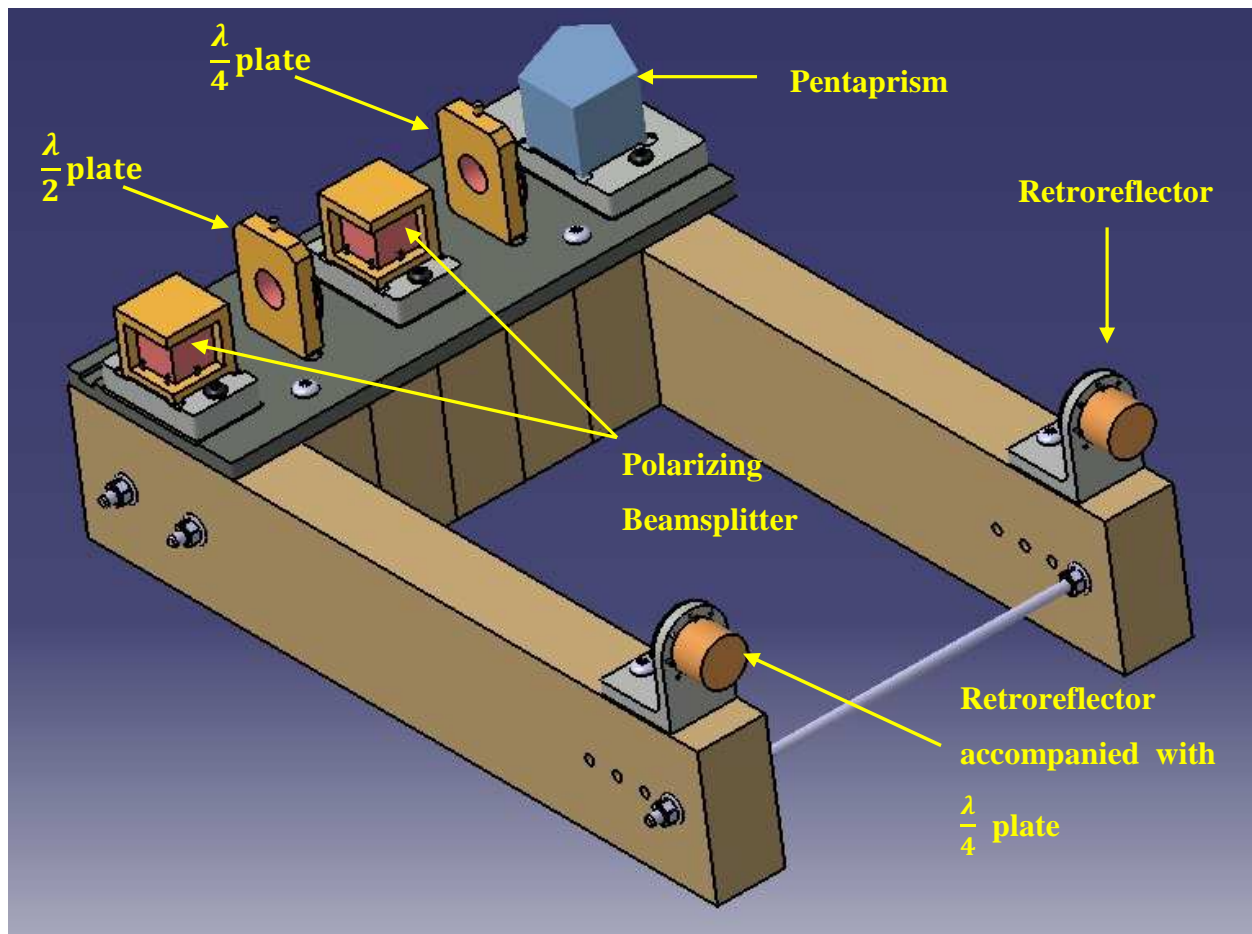


Figure 2.22 Arrangement of metrology elements in CATIA

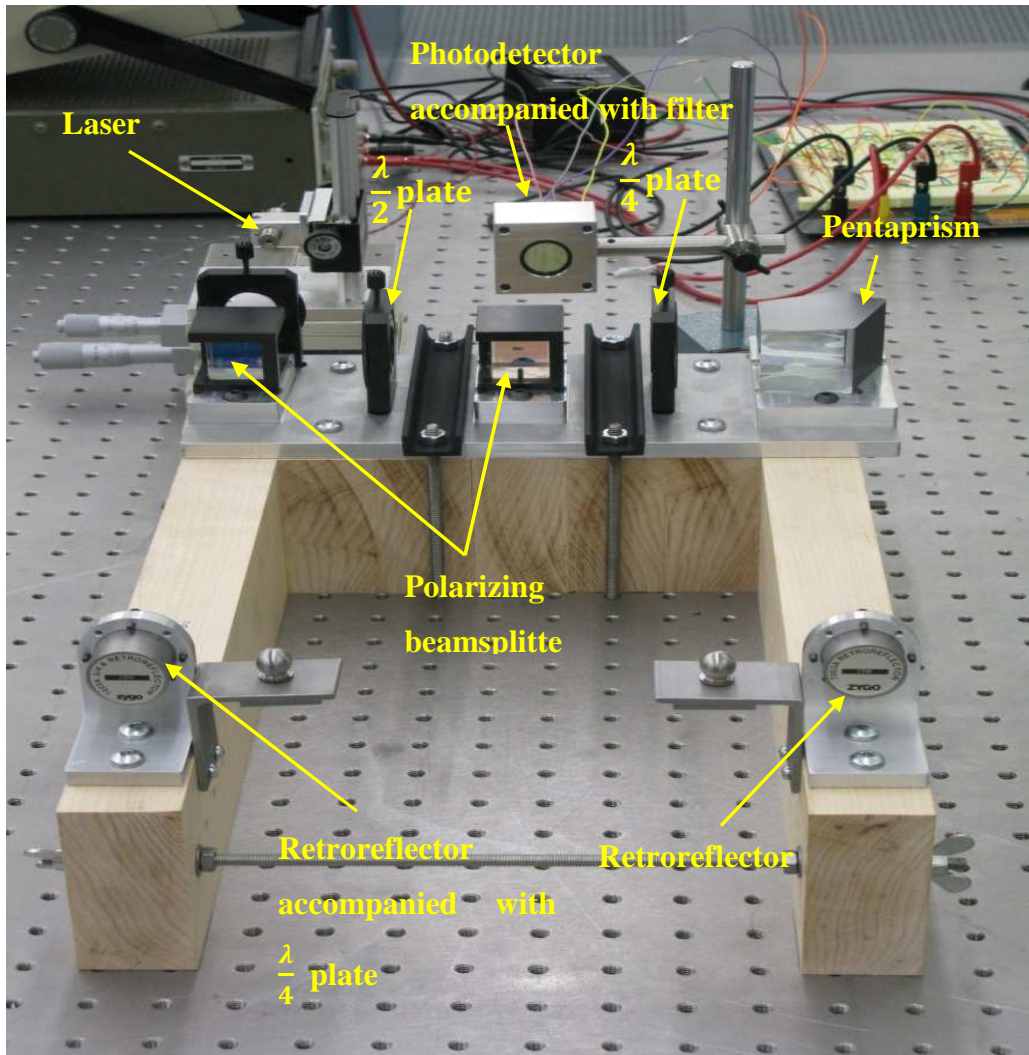


Figure 2.23 Implemented metrology frame

2.4 Electrical section

This section describes the conversion of the final laser beam position, as a spot on a photodetector, into an electrical signal.

2.4.1 Photodiode and its application in position sensing

Accurate measurement of the position of a laser beam can be achieved in several ways. One which brings about a good positioning accuracy, a fast response time (in the microsecond range)

as well as generating continuous data is using a quadrant photodiode with simple electronic circuitry. The principle of photodiode is given in Appendix C.

One of the main applications of photodiodes is for position measurement, namely position sensing detectors (PSDs), with the capability of converting an incident light spot position into a series of analog signals. In order to measure the beam position in 2D, PSDs are divided into four independent segments with a small gap or dead region of a few micrometers between them, Figure 2.24. In this case, they are called segmented or quadrant photodiode. An axisymmetric optical beam generates equal photocurrents in all segments while it is positioned at the center. The relative position can be obtained by comparing the signal received from each of the separate segments where the current difference between each half of the detector provides an indication of position in each direction. Eq. 10 and eq. 11 effectively show the relative displacement of the center of the beam ($\Delta x, \Delta y$) which is a linear combination of all four distinct segments where $A, B, C,$ and D are the signals generated by each of the four quadrants, Figure 2.24.

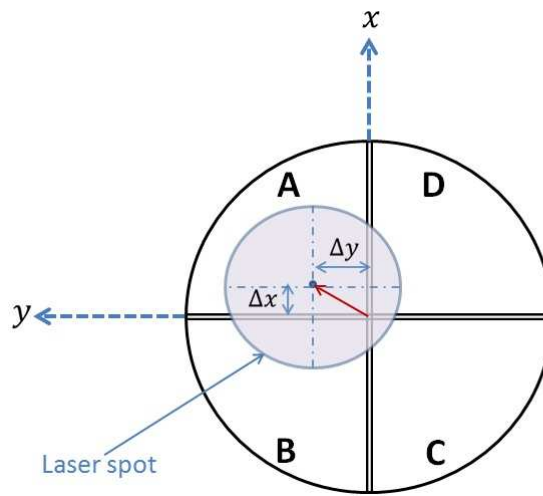


Figure 2.24 Quadrant photodiode and its coordinate frame

$$\Delta y = \frac{(A + B) - (C + D)}{A + B + C + D} \quad (10)$$

$$\Delta x = \frac{(A + D) - (B + C)}{A + B + C + D} \quad (11)$$

For the PSDs, position sensing requires that the beam touches all four elements simultaneously and that the spot size be less than the detector's active area but larger than the gap between individual active area. Hence, the positional detection range is related the spot size. Moreover, the positional resolution with small beam size is higher than for larger one because with the same displacement of the beam for two different sizes of spot the smaller one results in a large shift of light energy between segments, Figure 2.25. The main feature of this kind of detectors is that the sensibility (the slope of the linear region) can be increased as much as we need just by reducing the size of the spot.

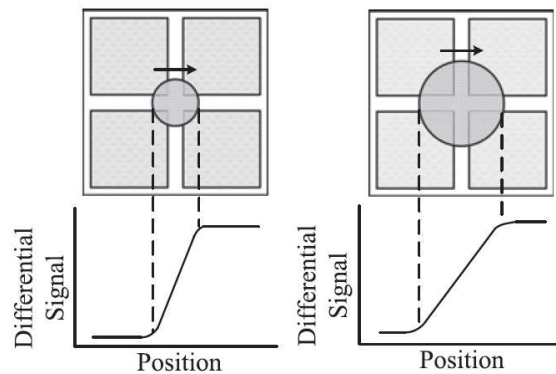


Figure 2.25 Positional resolution [57]

In this project, the SPOT series photodiode from Osioproelectronics is adopted which has a 10 *mm* diameter (active area per element of 19.6 *mm*²), dark current of 0.5 *nA* and element gap of 0.102 *mm* [58]. The Spot series have resolution better than 1 μm and spectral response range from 350-1100nm, so to eliminate the ambient light, a filter must be used.

2.4.2 Implementation of the circuit

As shown in Figure 2.26, the photodiode is in photovoltaic mode (zero biased). The photocurrent generated in each segment is then amplified by identical op-amp circuits with the gain of $R_f = 100\text{K}\Omega$. The first column of amplifiers are transimpedance amplifiers (current to voltage op-amp). In the second column, two differential amplifiers are used to give the relative position in both *x* and *y* directions (coordinate of center of the beam in 2D) in addition to a summing amplifier that is proportional to light intensity and is almost constant while the spot touches the active area of the photodiode. The function of each Op-amp is given in detail in Appendix D.

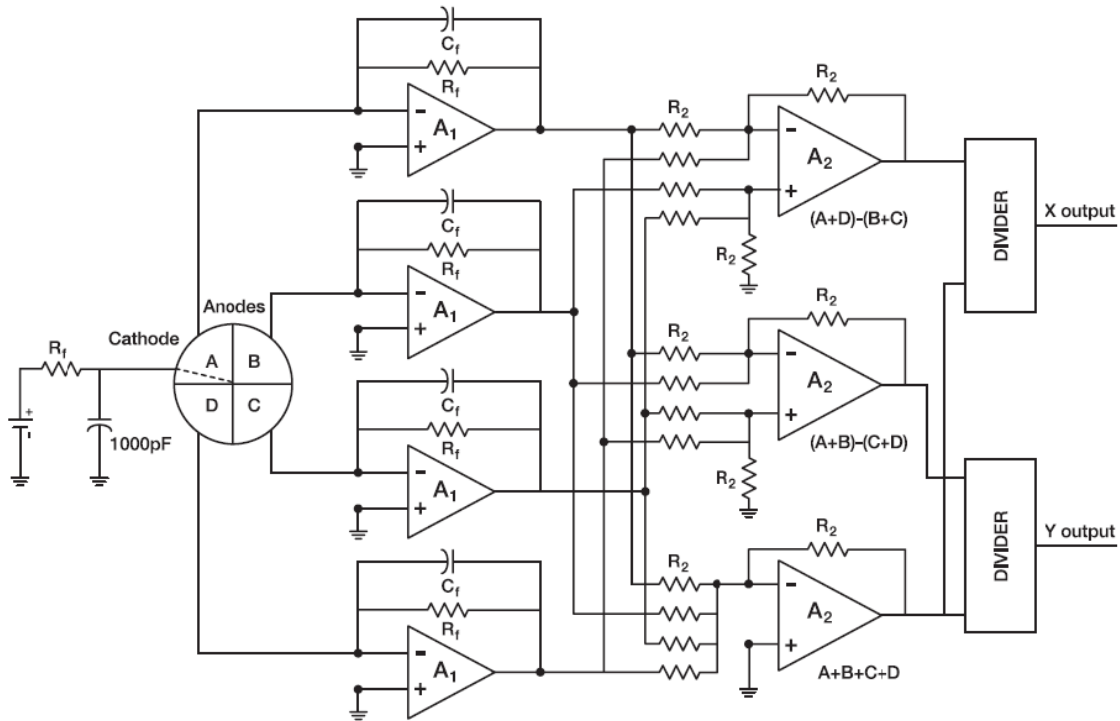


Figure 2.26 Final electrical circuits [58]

The above circuit was built and tested. Figure 2.27 shows the implemented entire electrical circuit in detail. The documentation of all metrology components and electrical elements are given in Appendix E and F respectively.

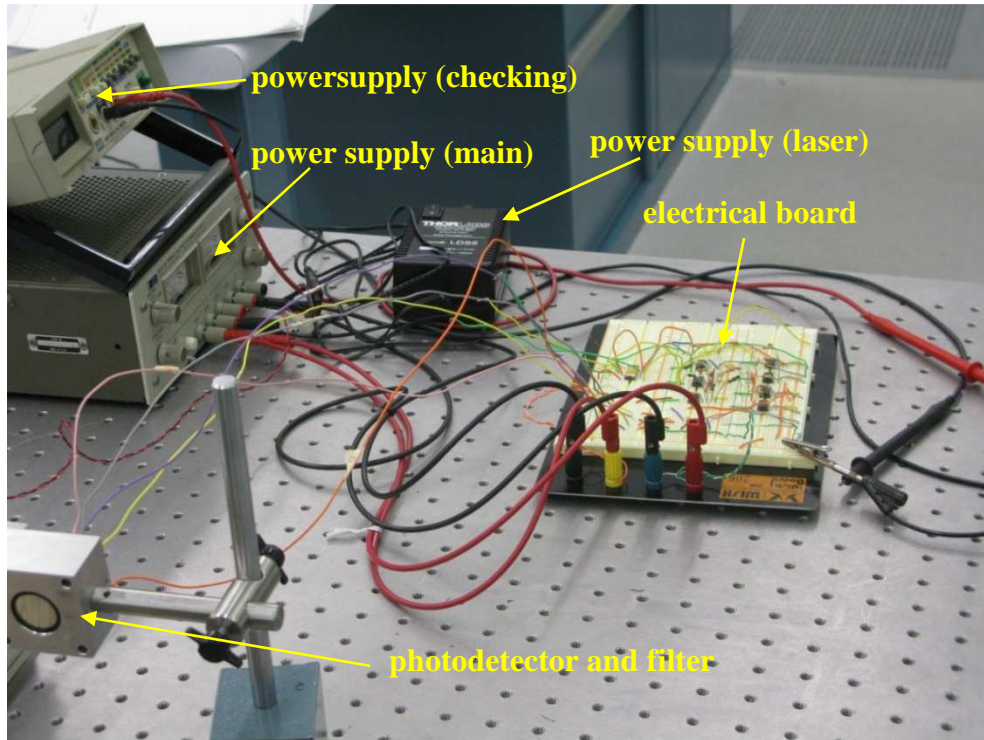


Figure 2.27 Electrical section

CHAPTER 3 CONDUCTING A METROLOGY TEST AND DISCUSSION

In order to evaluate the performance and precision of the implemented metrology frame, three different tests are conducted. Firstly, a deflection test aims to determine how sensitive the photodiode is to linear movement, namely deflection, of the C-frame arms while the arms open and deflect in opposite direction in y . Two other tests assess the sensitivity of the movement of the beam in the photodiode plane, with respect to rotations of the laser head around the y and x axes. As shown in Figure 3.1, deflection is along the y axis and light propagates in the z direction which is perpendicular to the $x - y$ plane.

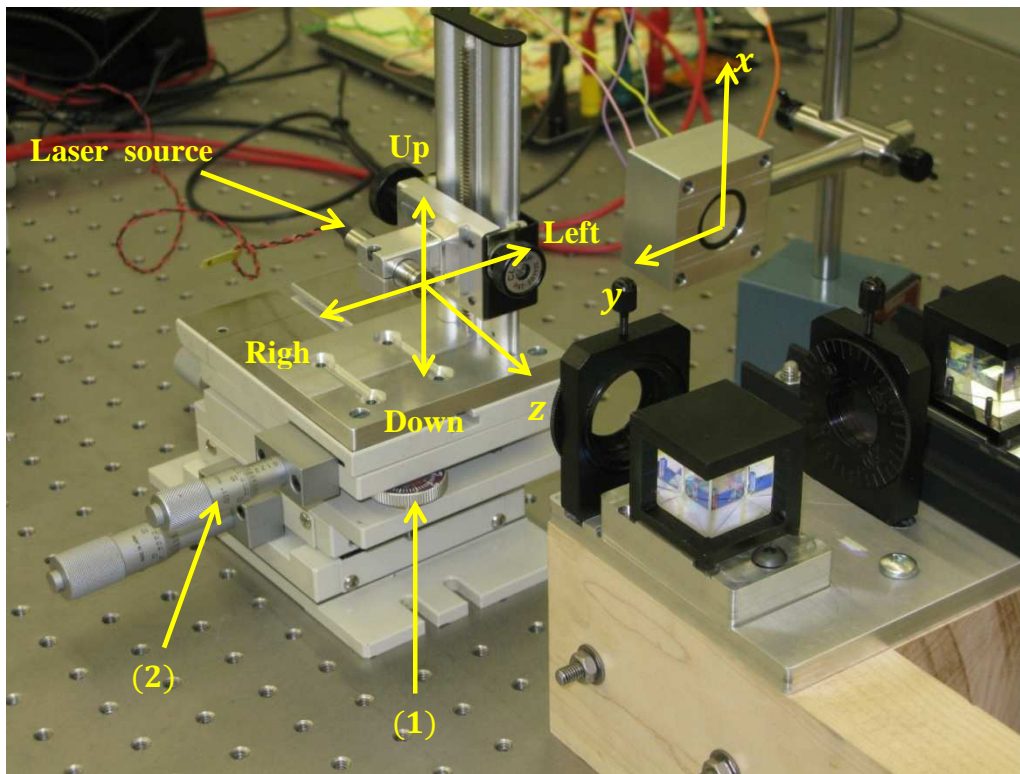


Figure 3.1 Coordinate and directions used during the test

Referring to Figure 3.1, turning the adjustable knob no.1, rotates the laser head around the y -axis resulting in the movement of laser beam in the photodiode plane, up and down, and so changing the values of Δx . In addition, adjustment of knob no.2 rotates the laser head around the x -axis causing the movement of the beam position along they-axis (right and left) and necessarily changing the values of Δy . The resulting data are given in Appendix F.

3.1 Deflection test

During the machining process major forces are applied along they-axis causing deflections of the C-frame arm in they direction. As observed before, based on simple FEM analysis done in CATIA, the force inside the C-frame causes an opening of the C-frame , with the arms deflecting in opposite direction (the upper arm goes up and the lower one goes down).

In this regard, the effect of each arm on beam position is considered separately using the superposition method. As shown in Figure 3.2, machining forces cause deflection (Δ_1) in the lower arm causing beam position change of Δ'_1 in the positive direction of y at the photodiode.

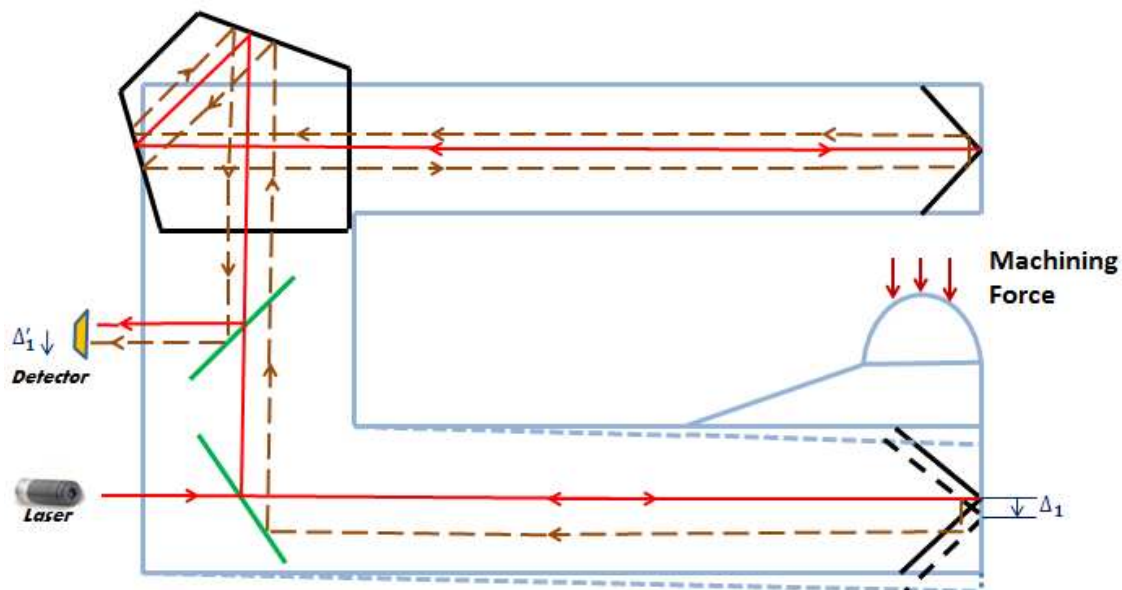


Figure 3.2 Beam position because of deflection in lower arm

Similarly, the upper arm is subjected to two loads. It has to support the total weight of the C-frame and also bear the reaction of machining force in the place of support. Because these two forces may be in the same direction, it is observed that the outcome reaction force is applied upward and hence resulting in a deflection of Δ_2 . According to Figure 3.3, a deflection in the upper arm (Δ_2) has an effect similar to Δ_1 and causes the position movement towards positive direction of y at the detector (Δ'_2). Therefore, it is possible to measure both deflections with one beam passing through the C-frame.

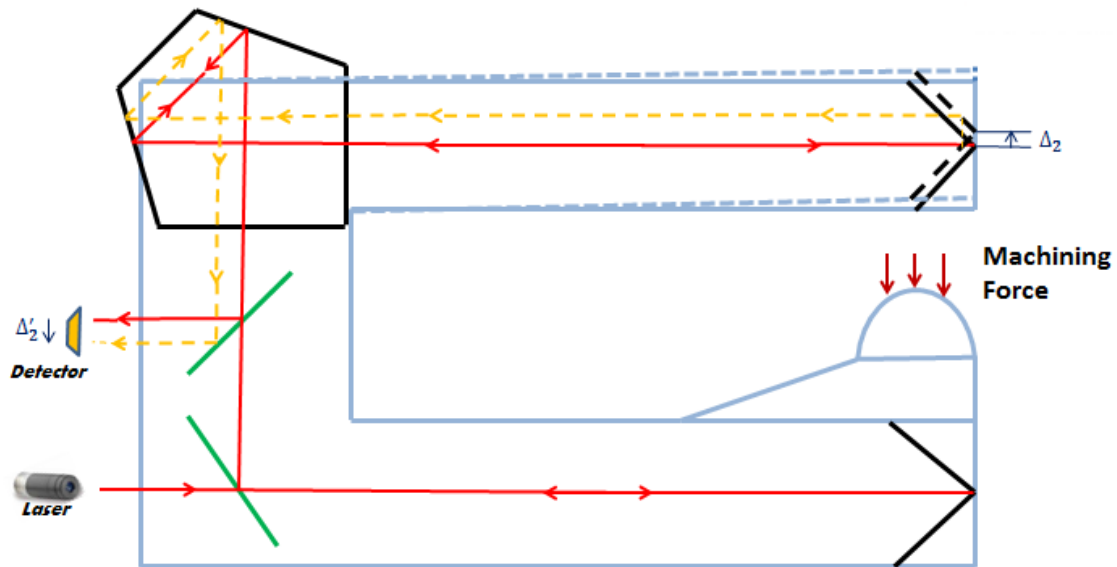


Figure 3.3 Beam position because of deflection in upper arm

Instead of applying the real force, the test procedure is simulated by opening the C-frame manually with two nuts and a threaded bar and measuring the distance between two balls (d), as shown in Figure 3.4. The balls are located in line with the retroreflector apices to avoid aberrations.

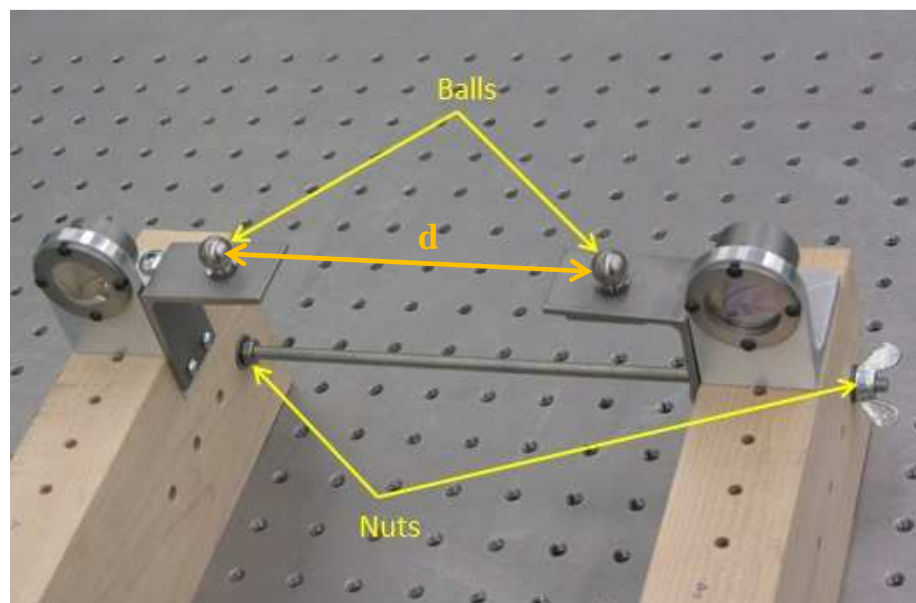


Figure 3.4 Proposed manual deflection producing

Figure 3.5 shows the results of deflection tests. As can be seen on the graph, the amount of Δy increases significantly while the values of Δx remain almost constant. Also, the tests are continued when the value of one of the segments become very small which means that the laser spot does not touch it efficiently. The data are fitted with polynomial function of degree three where the value R^2 quantifies goodness of fit and is a fraction between 0 and 1, and has no units. Higher values indicate that the model fits the data better. When $R^2 = 1$, all points lie exactly on the curve with no scatter. As it is clear the measurement range is around 2mm which causes around 4mm movement of the beam spot on the photodiode surface.

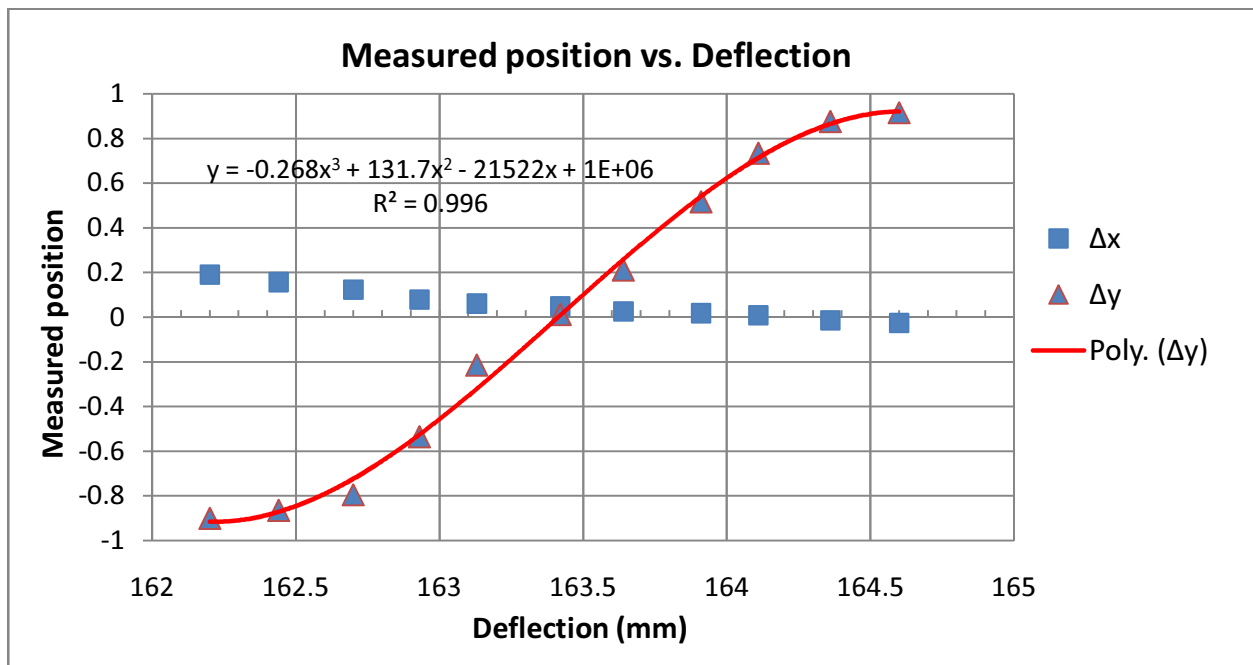


Figure 3.5 Measured positions with respect to deflection

According to Figure 3.6, the function relating the position to the voltage has a Gaussian form which confirms the accurate and reasonable trends of data.

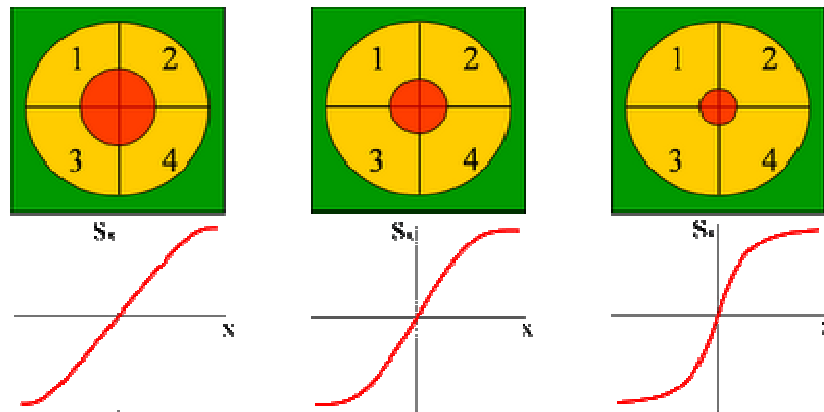


Figure 3.6 Voltage with respect to beam position for different beam diameter [59]

It is suggested to work around the middle of the Gaussian curve which means that around the center of the photodetector the results are more accurate and there is a linear relation between input and output. In this case, The useful range for measurement is about 1.5 mm around the center of the photodiode, both in upper and lower arm, which means this system is linearly sensitive to deflection up to 1.5 mm (and less than 2 mm) knowing this fact that the beam diameter is 4 mm .

3.2 Repeatability tests

Repeatability reflects the accuracy of results, the procedure, instruments and generally behaviour of the system. It shows in how much degree the results and consequently the system under tests are robust and stable. The Gaussian trends of all curve conforms the reasonable trend. In the Figure 3.7, “+ “ sign reflects the opening of the C-frame and the “-“ sign shows the closing of the C-frame for five sets of data.

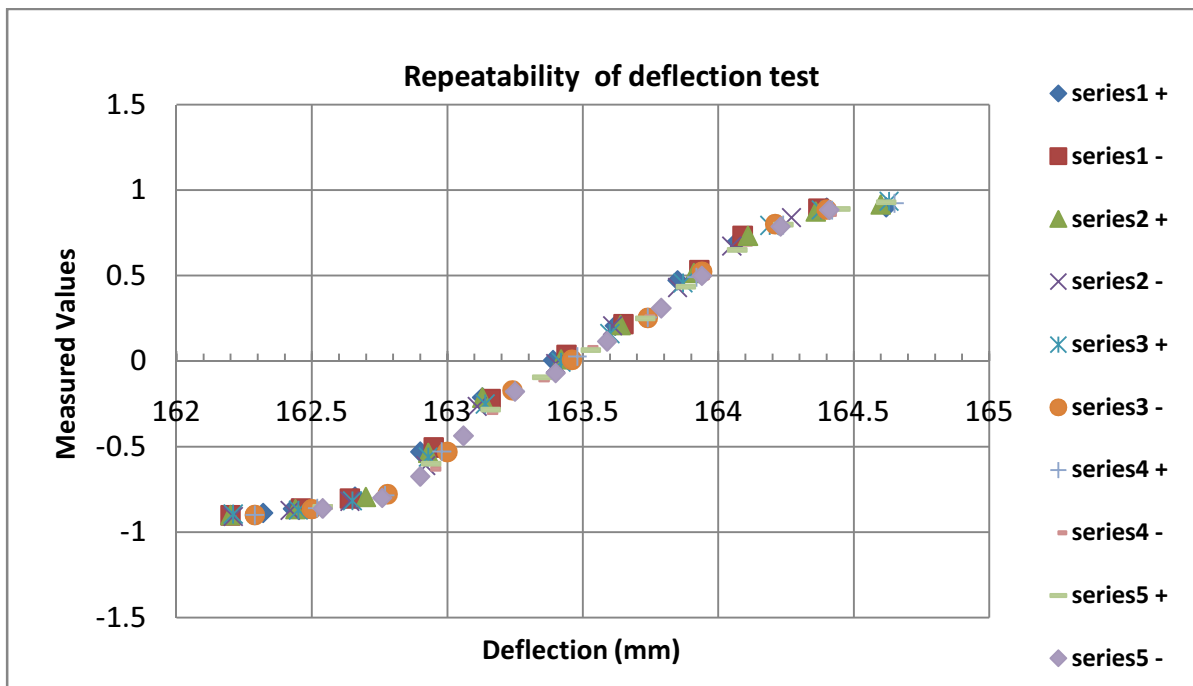


Figure 3.7 Repeatability test

As it is shown in the graph, the useful deflection range is between 162.75 mm to 164.25 mm which validate again the range of measurement (less than 2 mm). All data are settled very close to each other and in most of the cases indistinguishable.

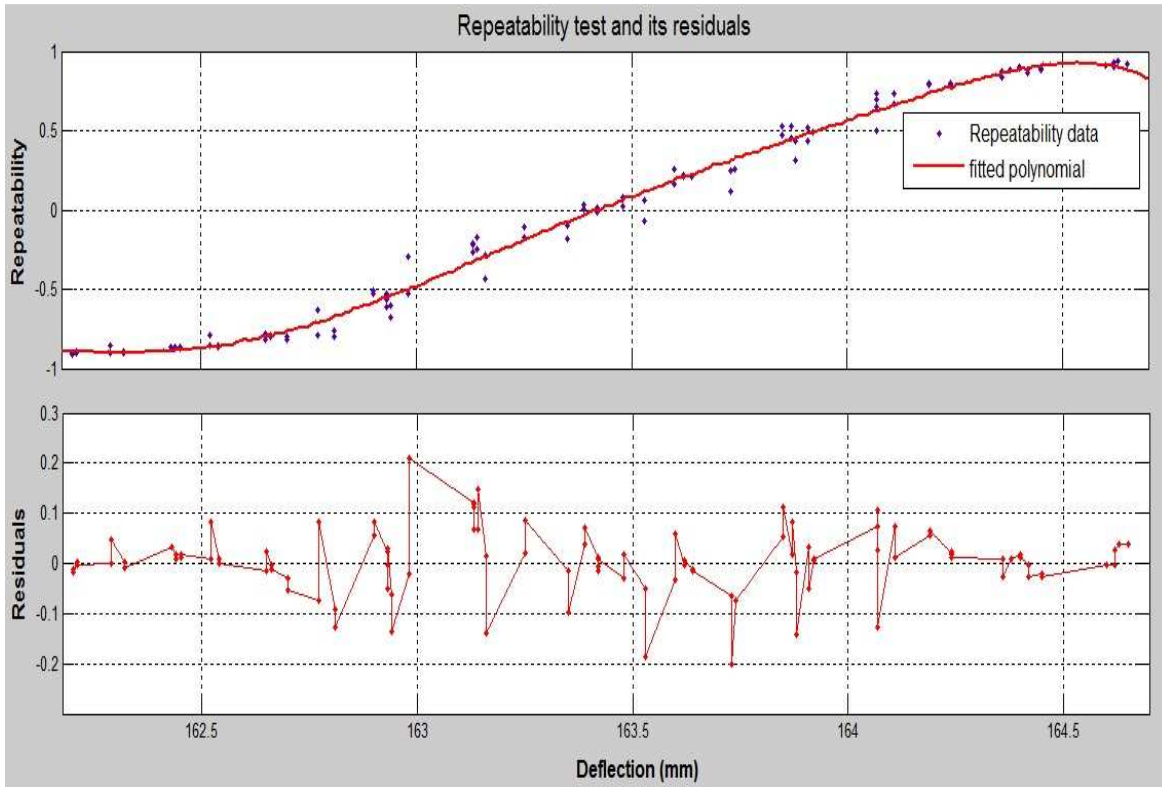


Figure 3.8 Residuals of the repeatability data with respect to the best fit

Figure 3.8 shows the residuals resulted from nominal values of the repeatability test with respect to the fitted polynomial of degree eight. The residuals are laid mostly between -1 and +1 that express the closeness of data.

3.3 Laser head rotation

Laser head rotation about the x and y axis, investigate the sensitivity of the proposed laser tracking system to rotation of the laser source. Even though the laser source is fixed on the frame and is subjected to very small strains. These tests represent how robust is the system to such disturbance.

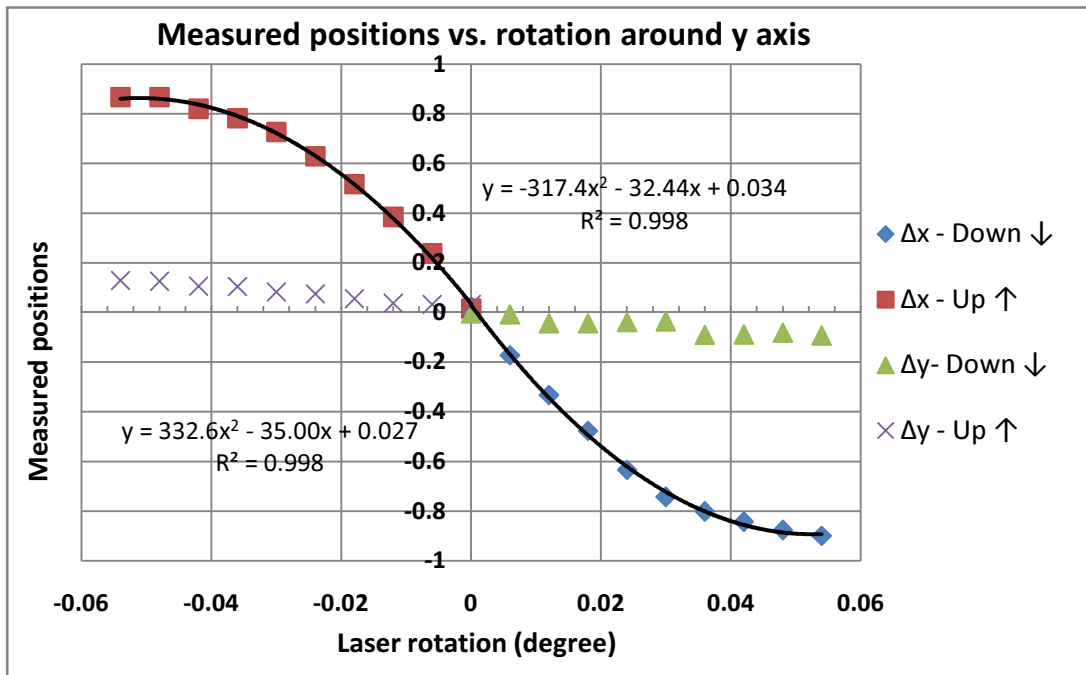


Figure 3.9 Measured positions with respect to laser rotation around y axis

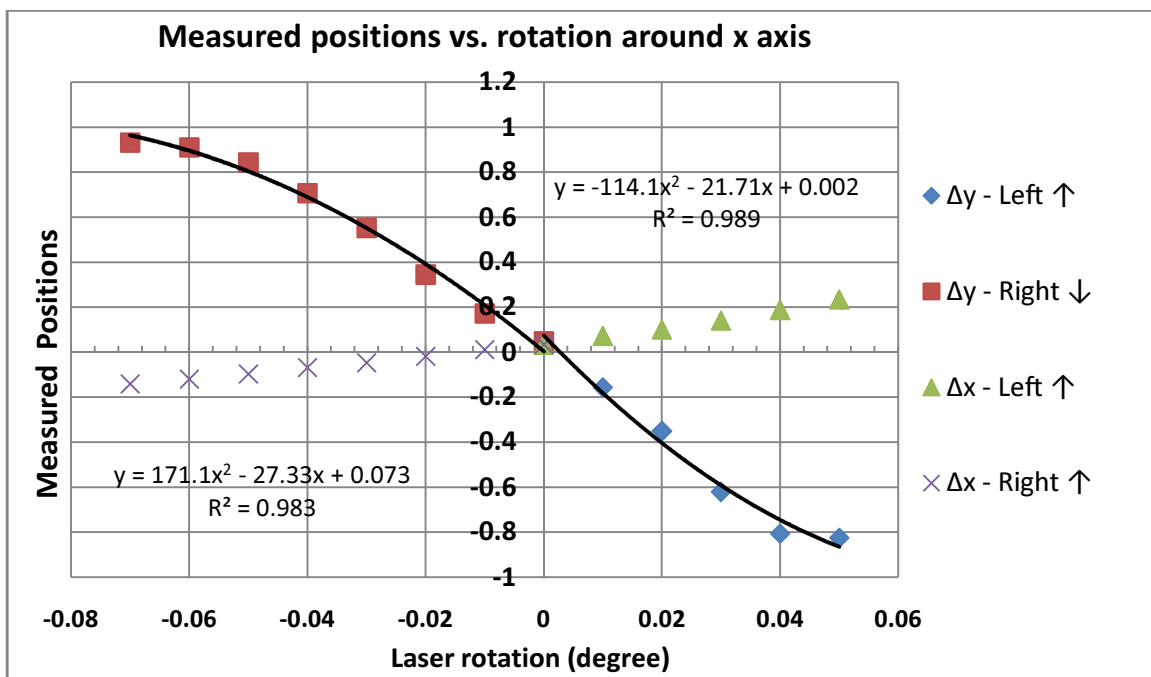


Figure 3.10 Measured positions with respect to laser rotation around x axis

According to Figure 3.9 and Figure 3.10, the trends are the same for up-down and right-left movement. Besides, regarding the large variations of Δy , on the other hand, the changes of Δx is negligible and emphasise the consistent of tests results with the prediction deduced from the theory and physical behaviour of the metrology frame.

These results indicate that the mechanical stability of the laser mounting is very important and must be considered.

3.4 Accuracy of the measurements

In order to evaluate the amplitude of error associated with the results of the tests and to estimate the accuracy of measurements, all signals are observed on an oscilloscope and the error in the form of sinusoidal signals are monitored. All following figures show the error signals which are in voltage (100 *mv*) with respect to time (10 *ns*). Figure 3.11 shows the error signal when the laser was turned off. The error amplitude is 100 *mv* while there is not any laser beam.

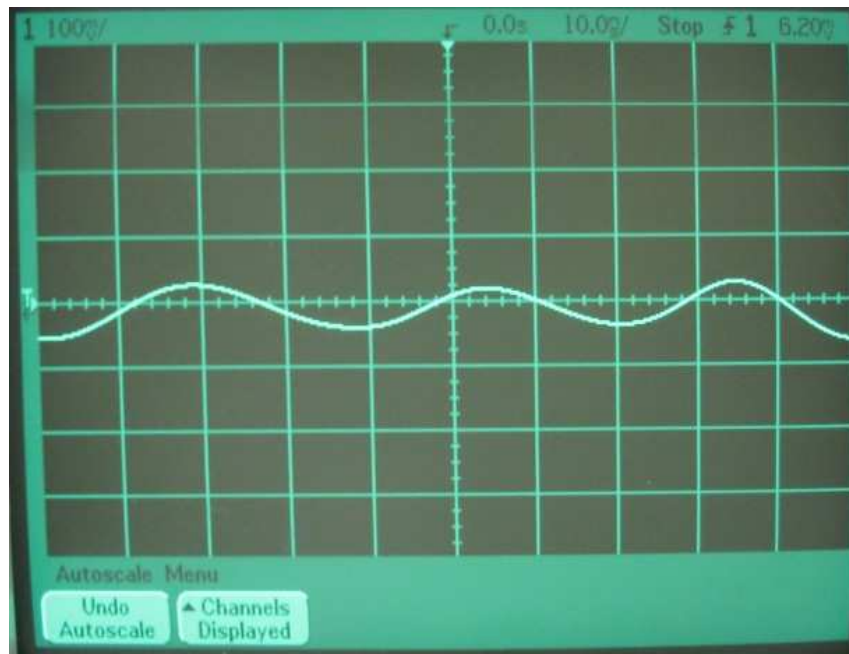


Figure 3.11 Associated error without any laser light
(Horizontal scale = 10 *ns*/div. , Vertical scale = 100 *mv*/div.)

this shows there is a noise unrelated to the laser source and much more relevant to the electrical parts. The frequency is around 33 MHz that is far from the normal electricity frequency (60Hz) and also the laser light frequency ($f = \frac{c}{\lambda} \cong 10^{15} \text{ Hz}$).

Figure 3.12 shows the error associated with segment A of the photodiode. The related noise signals for other segments are given in Appendix G.

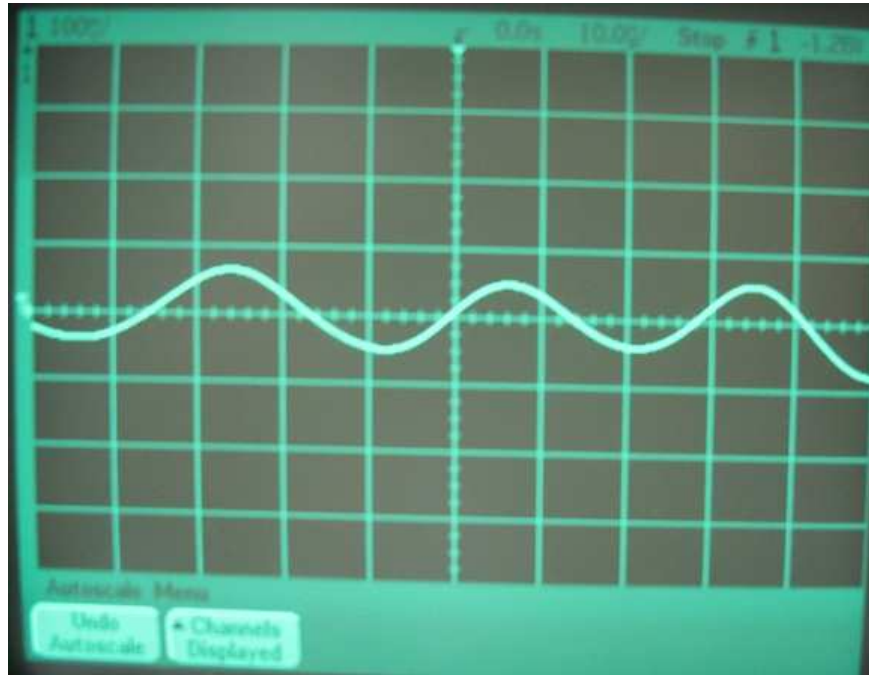


Figure 3.12 Error signal related to leg A of photodiode (A)
(Horizontal scale = 10 ns/div. , Vertical scale = 100 mv/div.)

Figure 3.13 and 3.14 shows the error signals related to the differential and summing amplifiers respectively. As deduced from the figures the errors are almost the same.

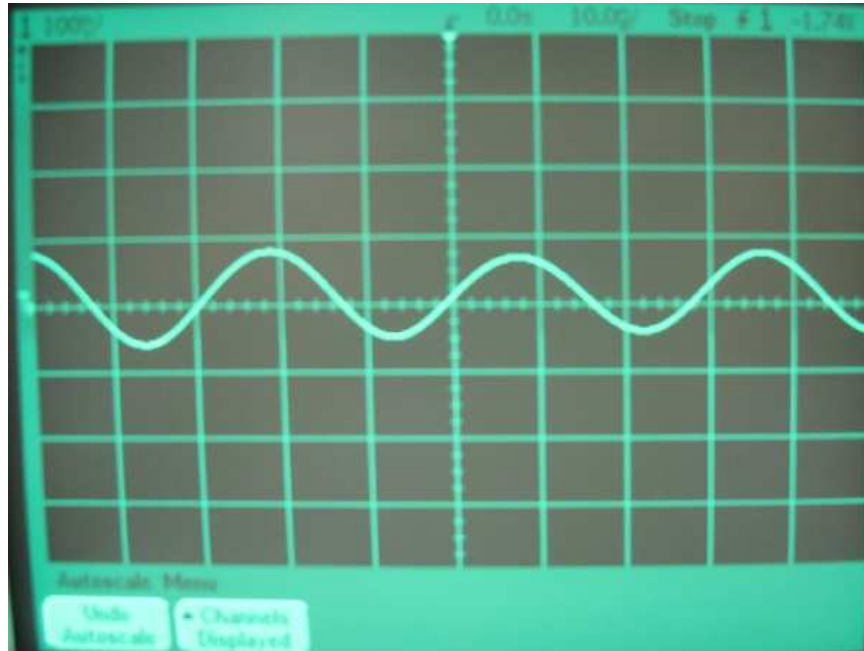


Figure 3.13 Error signal of first differential amplifier (E)

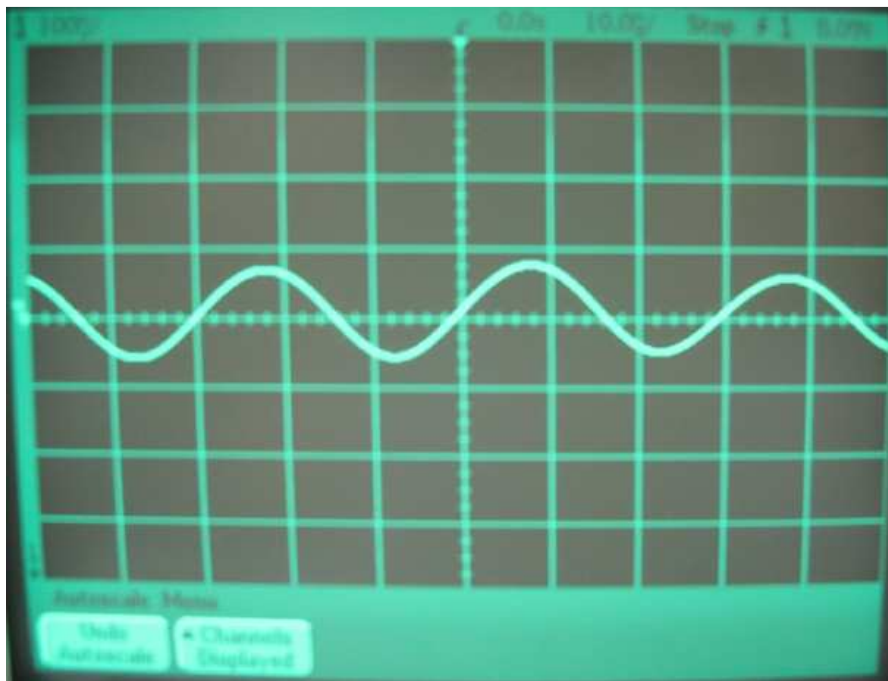


Figure 3.14 Error signal of sum amplifier (G)

Table 3.1 shows the nominal value and related error signals for different sections of the aforementioned circuit (Figure 2.26).

Table 3.1 Error signals associated with the data in terms of amplitude and frequency

	Nominal value(v)	Noise Amplitude (mv)	Noise Ratio	Noise Frequency (Hz)
no light	0	100	-	27.77×10^6
A	-1.251	125	9.99%	28.57×10^6
B	-2.182	125	5.73%	31.25×10^6
C	-1.667	100	5.99%	31.25×10^6
D	-0.915	125	13.66%	25.64×10^6

As table 3.1 shows, error signals have approximately the same amplitude. Even when the laser is turned off there is an noise with amplitude of 100 *mv*. It can be because of electrical elements such as op-amps. Using another set of electrical material may be useful to reduce the noises. Using electrical filters can be another suggestion to remove it.

Knowing this fact that each segment can have a values between zero to -1.5v which is equivalent to 2 *mm* deflection and regarding the average noise to signal ratio of 8.84% ,it is possible to measure the deflection with the accuracy of ± 0.088 *mm*.

CONCLUSION AND FUTURE WORKS

Conclusion

In this research, in order to machine large flexible panels, a new opto-electro method was presented. Based on some relevant patents reviewed, a conceptual design was proposed. The design criteria concerned mainly the panels size and flexibility as well as supporting the total load : the weight of the C-frame and machining force. Moreover, The proposed metrology frame based on opto-electronic concept can measure any disturbances like chatter and vibration during machining in addition to the ordinary force-induced deflection.

The proposed C-frame was modelled in CATIA and the machining conditions were simulated by FEM. As observed in FEM simulations of the C-frame, the critical zone with respect to stress is in the area where most of the optical elements are located. As a result, all optics must be located on a stabilized platform not subject to these deformation.

In order to conduct tests of the proposed metrology frame, a wooden C-frame was built and all optical elements were fixed on it. Deflection tests were designed to measure the deflection applied in C-frame due to machining force and laser head rotation tests pursue the sensibility of results with respect to any rotation of the laser source. The trend of the graphs taken as a result of tests confirms the correctness of the built metrology frame.

The error associated with each signal was monitored and found to be present even without laser spot so it is concluded that it is more related to the electrical circuitry such as op-amps than the laser source.

Current research shows that by employing the optical systems (metrology frame) inside the mechanical tools (C-frame) the effects of small displacement in the range of less than 2 *mm* are measured within the tolerance of ± 0.088 *mm*.

Future works

Regarding the achievements of the current research, the following issues can be considered in order to obtain better results and to continue the actual study:

- Utilizing a better set of electrical circuit helps to reduce the error signals associated with the data and therefore result in a precise deflection measurement system.
- Regarding the shape and weight of the C-frame, developing a new design by using shape and structural optimization techniques to achieve high stiffness and adequately protect all optical materials and photodiode without applying extra load to the robot.
- Using a bigger laser spot and bigger photodiode can increase the range of measurement significantly which can be used where there are a large and unpredicted machining force and necessarily bigger unpredicted deflection.
- Integration of the metrology frame in a realistic C-frame.
- Designing a new metrology frame with double beam in order to reduce the sensitivity of the metrology frame to the laser source motion.

REFERENCES

- [1] <http://www.asminternational.org/portal/site/www/>
- [2] F. Campos , A. Filho and A. Pina, “ Using Robots to material removal processes ”, *Proceedings of the 9th Brazilian Conference on Dynamics Control and their Applications* , June 07-11,2010.
- [3] D. Milutinovic , M. Glavonjic, N. Slavkovic, Z. Dimic, “Reconfigurable robotic machining system controlled and programmed in a machine tool manner ” , *Int. J. Adv. Manuf. Technol.* , vol. 53, pp. 1217–1229, 2011.
- [4] H. Zhang, Z. Pan and Z. Zhu et al. , “Machining with flexible manipulator: toward improving robotic machining performance”, *IEEE/ASME AIM*, July 24-28, pp. 1127-32, 2005.
- [5] Z. Pan, H. Zhang, “Robotic machining from programming to process control: a complete solution by force control”, *Industrial Robot: An International Journal*, vol. 35/5, pp. 400–409, 2008.
- [6] Z. Pan, H. Zhang, “Robotic Machining from programming to process control ”, *Proceedings of the 7th World Congress on Intelligent Control and Automation* , Chongqing, China, June 25 - 27, 2008.
- [7] A. Allcock, “Reports: Robot Machining” ,April 2012
URL:<http://www.machinery.co.uk> .
- [8] COMET, 2011, EU/FP7-project: Plug-and-produce COmponents and METHods for adaptive control of industrial robots enabling cost effective, high precision manufacturing in factories of the future. <http://www.cometproject.eu>

- [9] The COMET news, “COMET project targets industrial Robots for high-end machining ”, Issue 1-January 2011.
- [10] J. Pandremenos , C. Doukas, P. Stavropoulos and G. Chryssolouris, “MACHINING WITH ROBOTS: A CRITICAL REVIEW ”, *Proceedings of DET2011: 7th International Conference on Digital Enterprise Technology*, Athens, Greece, 28-30 September, 2011.
- [11] Pan, Z. (2006). “Intelligent robotic machining with force control”, *Ph.D. dissertation*, Stevens Institute of Technology, NJ, USA, Jan 2006.
- [12] Y. Altintas, “Manufacturing Automation: Metal Cutting Mechanics, Machine Tool Vibrations, and CNC Design”, *Cambridge University Press*, 2000.
- [13] E. Abele, M. Weigold and S. Rothenbucher, “Modeling and Identification of an Industrial Robot for Machining Applications”, *CIRP Annals - Manufacturing Technology*, Volume 56, Issue 1, Pages 387–390, 2007.
- [14] E. Abele, J. Bauer, S. Rothenbücher, M. Stelzer and O. von Stryk, “Prediction of the Tool Displacement by Coupled Models of the Compliant Industrial Robot and the Milling Process ”, *Proceedings of the International Conference on Process Machine Interactions*, pp. 223-230, 3-4 September, 2008 .
- [15] C. Doukas, J. Pandremenos, P. Stavropoulos and P. Fotinopoulos, “On an empirical investigation of the structural behaviour of robots”, 45th CIRP Conference on Manufacturing Systems, Volume 3, pp.501 – 506, 2012 .
- [16] E. Abele , J. Bauer , T. Hemker , R. Laurischkat, “Comparison and validation of implementations of a flexible joint multibody dynamics system model for an industrial robot”, *CIRP Journal of Manufacturing Science and Technology* vol. 4, pp. 38–43 , 2011.

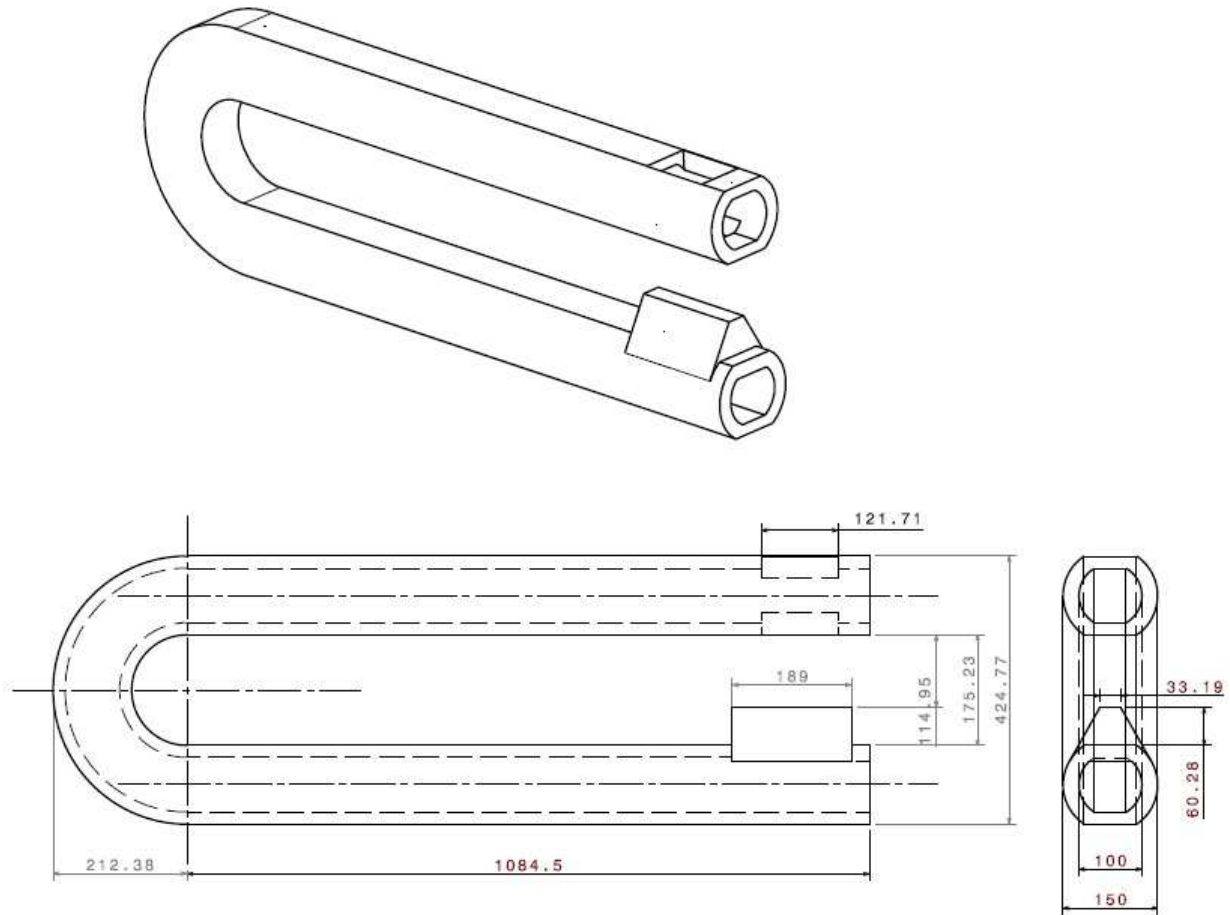
- [17] J. Wang, H. Zhang, Z. Pan, "Machining with Flexible Manipulators: Critical Issues and Solutions", *Industrial Robotics: Programming, Simulation and Applicationl* ,pp. 515-536 , December 2006 .
- [18] E. Rubio, "Experimental analysis of the tool-to-workpiece vibrations transmission during chatter development in milling processes " ,*Scientific Research and Essays* ,vol. 7(39), pp. 3286-3291, 4 October, 2012 .
- [19] Z. Pan, H. Zhang ,Z. Zhub, J. Wang, "Chatter analysis of robotic machining process ", *Journal of Materials Processing Technology* ,vol. 173, pp. 301–309, April 2006 .
- [20] Y. Oki, K. Kanitani, "Development of robot machining system for aluminum building materials" ,*J. JSME*, vol. 99 , pp. 78, 1996.
- [21] S. Matsuokaa, K. Shimizu, N. Yamazaki, Y. Oki, "High-speed end milling of an articulated robot and its characteristics", *Journal of Materials Processing Technology*, vol. 95, pp. 83-89, 1999 .
- [22] J.S. Dhupia, and A. Ulsoy, "Control of Machine Tools and Machining Processes", *The Control Handbook*, W.S. Levine (ed.), 2nd Edition, CRC Press , 2009.
- [23] A.Sharon, N.Hogan, D.E.Hardt, "The macro/micro manipulator: An improved architecture for robot control " , *Robotics and Computer-Integrated Manufacturing*, Volume 10, Issue 3, Pages 209–222, June 1993.
- [24] O. Sornmo, B. Olofsson, U. Schneider, A. Robertsson and Rolf Johansson, "Increasing the Milling Accuracy for Industrial Robots Using a Piezo-Actuated High-Dynamic Micro Manipulator " , *The 2012 IEEE/ASME International Conference on Advanced Intelligent Mechatronics* , Kaohsiung, Taiwan, July 11-14, 2012.
- [25] B. Olofsson, O. Sornmo, U. Schneider, Anders Robertsson, "Modeling and Control of a Piezo-Actuated High-Dynamic Compensation Mechanism for Industrial Robots " , *IEEE/RSJ International Conference on Intelligent Robots and Systems (IROS)*, 25-30 september , 2011 .

- [26] C. Gong, J. Yuan , J. Ni, “Nongeometric error identification and compensation for robotic system by inverse calibration ”, *International Journal of Machine Tools & Manufacture*, vol. 40 , pp. 2119–2137, 2000 .
- [27] J. M. Motta, G. C. de Carvalho, R.S. McMaster, “Robot calibration using a 3D vision-based measurement system with a single camera ”, *Robotics and Computer-Integrated Manufacturing*, vol. 17, Issue 6, , pp. 487- 497,Dec. 2001.
- [28] M. R. Driels, W. Swayze,S. Potter, “Full-pose calibration of a robot manipulator using a coordinate measuring machine”, *Int. J.Manuf.Technol.*,vol 8,Issue 1, pp.34–41, 1993.
- [29] H. P. Jawale and H. T. Thorat , “Positional Error Estimation in Serial Link Manipulator Under Joint Clearances and Backlash ”, *J. Mechanisms Robotics* 5(2), Mar 26, 2013.
- [30] Y. Chen and F. Dong , “Robot machining: recent development and future research issues ” , *Int J Adv .Manuf .Technol.*, August 2012.
- [31] http://www.airbus.com/company/environment/documentation/?eID=dam_frontend_push&docID=4033
- [32] http://ec.europa.eu/environment/life/project/Projects/index.cfm?fuseaction=search.dsPage&n_proj_id=2858
- [33] <http://www.mtorres.es/en/aeronautics/products/metallic/torres-surface-milling>
- [34] Abel. Chuinard, “Replacement of chemical machining by mechanical milling in machining of Alluminumalloys” ,Thesis,ecolepolytechnique,April 2011.
- [35] H. Heidari-Roushan, L. Baron, “Design of new PSP mechanism usable in robotic machining of panels ” , Thesis, ecolepolytechnique, 2013.

- [36] G. B. Bonomi, B. Oldani, “Multi-task end-effector for Robotic machining center”, US patent No.: 4,955,119
- [37] G. B. Bonomi, L. Ciacomini, “Riveting process and apparatus”, US patent No.:4,885,836
- [38] R. Panzcuk, P. Foissac, “Process and a device for the machining of panels”, Dufieux and Airbus, US Patent No. : 7,682,112 B2
- [39] J. C. Hamann, “Process and mechanical device for machining flexible panels, in particular with complexe shape ”, US Patent No.: 7,507,059 B2.
- [40] J. C. Hamann, “Process and device for machining by windowing of non-deformable thin panels”, US PatentNo.: 7,168,898 B2.
- [41] J. R. Rene Mayer, “Polarization optics design for a laser tracking triangulation instrument based on dual-axis scanning and a retroreflective target”, *Journal of optical engineering*, Vol.32,No. 12, December 1993.
- [42] J. F. Cuttino, D.E. Schinstock, M.J. Prather, “Three—dimensional metrology frame for precision applications”, *Journal of precision engineering*, vol. 23, pp. 103-112, 1999 .
- [43] S. Moylan, D. Hong, “Development of a metrology frame to improve the positioning accuracy of Micro/Meso-scale Machine Tools”, *Int. J. Mechatronics and Manufacturing Systems*, vol. 2, Nos. 5/6, 2009.
- [44] http://en.wikipedia.org/wiki/Laser_tracker
- [45] I. Edwards, “Using photodetectors for position sensing”, *Sensors*, December 1988.
- [46] I. A. Ivan, M. Ardeleanu, G. J. Laurent, “High dynamics and precision optical measurement using a Position Sensitive Detector (PSD) in reflection-mode: application to 2D object tracking over s smart surface”, *Sensors*, vol. 12, pp. 16771-16784, 2012.

- [47] <http://www.repairfaq.org/sam/laserssl.htm>
- [48] <http://hyperphysics.phy-astr.gsu.edu/hbase/optmod/qualig.html>
- [49] <http://www.thorlabs.com/thorProduct.cfm?partNumber=CPS180>
- [50] <http://www.lasercomponents.com/us/product/polarizing-beam-splitter-cubes>
- [51] <https://www.cvimellesgriot.com/company/Glossary.aspx?Character=Q>
- [52] http://www.thorlabs.com/newgrouppage9.cfm?objectgroup_id=711
- [53] <http://search.newport.com/?x2=sku&q2=BPP-12.7>
- [54] <http://en.wikipedia.org/wiki/Retroreflector>
- [55] http://www.foctek.net/products/optics/P_C_C_R.htm
- [56] A. Gerrard, J. M. Burch, “ Introduction to matrix methods in optics ”,John Wiley, 1975 .
- [57] <http://www.aptechnologies.co.uk/support/photodiodes/bi-cell-a-quadrant-photodiodes>
- [58] <http://www.osioptoelectronics.com/Libraries/Product-Data-Sheets/Quadrant-Bi-Cell-Photodiode.sflb.ashx>
- [59] http://www.judsontechnologies.com/xy_position.html

APPENDIX A – C-FRAME DRAWING



APPENDIX B – MATLAB CODE

```

% ..... Jones Calculation of .....
% ..... Metrology frame .....
% .... Ref.: introduction to matrix method in optics .....
% ..... By: A.GerrardandJ.M.Burch .....

%..... QWP .....
t=pi/4;
QWP1=[cos(t)^2-i*sin(t)^2  sin(t)*cos(t)*(i+1);
sin(t)*cos(t)*(i+1)  sin(t)^2-i*cos(t)^2];
R1=QWP1;

t=-pi/4;
QWP2=[cos(t)^2-i*sin(t)^2  sin(t)*cos(t)*(i+1);
sin(t)*cos(t)*(i+1)  sin(t)^2-i*cos(t)^2];
R2=QWP2;

% ..... HWP .....
t3=pi/4;
HWP=[cos(2*t3)  sin(2*t3);sin(2*t3)  -cos(2*t3)];

% ..... PBS .....
t1=0;
PBS1=[cos(t1)^2  sin(t1)*cos(t1) ;
sin(t1)*cos(t1)  sin(t1)^2];

t1=pi/2;
PBS2=[cos(t1)^2  sin(t1)*cos(t1) ;
sin(t1)*cos(t1)  sin(t1)^2];

% .....
RtR=[1 0;0 -1];

% .....
PntP=[1 0;0 1];

% .....
E0=[1;1]
pt1=PBS1*E0
pt2=R1*PBS1*E0
pt3=RtR*R1*PBS1*E0
pt4=R2*RtR*R1*PBS1*E0
pt5=PBS2*R2*RtR*R1*PBS1*E0

% .....
pt6=HWP*pt5
pt7=PBS1*pt6
pt8=R1*pt7

% .....
pt9=PntP*pt8
pt10=RtR*pt9
pt11=PntP*pt10

% .....
pt12=R2*pt11
pt13=PBS2*pt12

```

APPENDIX C – PRINCIPLES OF PHOTODIODE

In order to better understand the optical position sensing, it is worth knowing the sensor, which form the heart of the system, in detail. Photodiodes are similar to semiconductor diode except they can be exposed to light. Hence, they are a *p-n junction* which is an interface between two type of semiconductor material, *p-type* and *n-type* (Figure B.1).

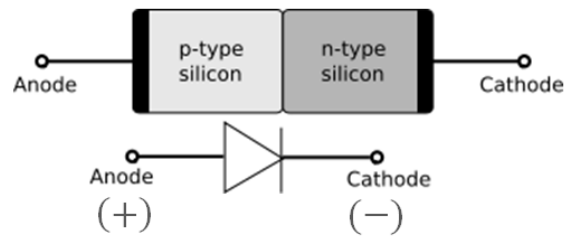


Figure B.1 p-n junction and diode symbol

When *p-type* and *n-type* are joined together to form a junction, due to a very large potential differences existing between both sides of the junction, electrons and holes tend to migrate to a region with lower concentration of electron and hole. Thus electrons diffuse from *n-type* to *p-type* region, leaving positively charged ions(donors), and holes diffuse from *p-type* to *n-type*, leaving fixed ions (acceptor), Figure B.2. In this regard, and looking at Figure B.2, this exchange make a built-in voltage followed by electrical field which result in a depletion region containing positive ions on the *n* side and negative ions on the *p* side.

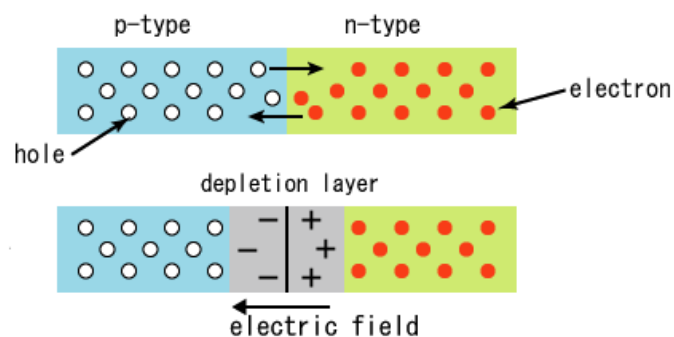


Figure B.2 Formation of depletion layer in p-n junction

As is found in Figure B.3, the potential differences between n and p is equal to voltage which results in an electric field directed from n -type to p -type.

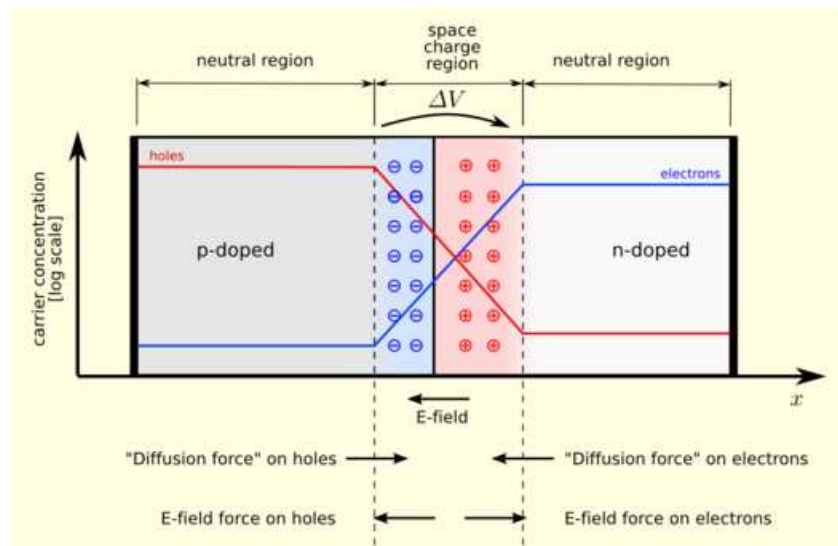


Figure B.3 Voltage and electrical field built in depletion region

When a photon of sufficient energy strikes the diode, like as in a photodiode, it absorbs and excites an electron and generates an electron-hole pair. When the photons reach the depletion region, the electric field forces them away such that the holes are pushed toward the anode (p-type) and electrons moves toward the cathode (p-type) resulting in a photocurrent which is linearly related to the intensity of the incident light and is practically independent of the bias voltage.

APPENDIX D – OP-AMP, FUNCTIONS AND TYPES

Operational Amplifier (op-amp) is such a device mostly used in analog electronics to amplify a voltage, Figure D.1. As eq.12 shows it magnifies the differences between inputs by using a large gain.

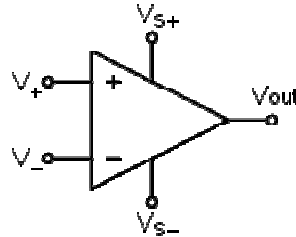


Figure D.1 Differential op-amp symbol [60]

$$V_{out} = G (V_+ - V_-) \quad (12)$$

where G is a gain in the order of more than 10^{+4} and V_{out} can utmost reach the voltage of the power supply ($\pm V_S$) otherwise the op-amp is saturated. To analyse the op-amp performance, there exist two golden rules, firstly the voltage differences between the inputs, V_+ and V_- , is zero. Secondly, the inputs draw no currents (it means that the impedance is much larger than any other current path).

In general, one of the inputs is connected to the ground. Figure D.2 shows an inverting amplifier because the input signal comes to the " - " input. Since input " + " is connected to the ground, by using rule one, input " - " is supposed to be at ground which is considered as virtual ground. So the voltage drop across the R_1 is $V_{IN} - V_- = V_{IN}$ and across the R_2 is $V_{OUT} - V_- = V_{OUT}$. By applying kirchoff's first law to the node at " - " :

$$i_- = 0 = i_{IN} + i_{OUT} = \frac{V_{IN}}{R_1} + \frac{V_{OUT}}{R_2} \quad (13)$$

or

$$G = \frac{V_{OUT}}{V_{IN}} = -\frac{R_2}{R_1} \quad (14)$$

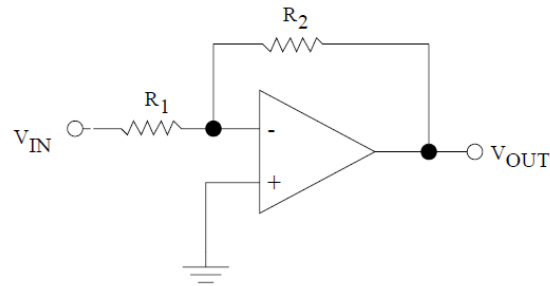


Figure D.2 Inverting amplifier [60]

Three frequently used op-amps circuits are relevant for converting the spot position to an x and y analog output.

D-1 Trans impedance amplifier (TIA)

As stated previously, photocurrents produced in a photodiode which flow from positive pole (anode) are in the order of mA or less and need to be magnified to be used. As shown in Figure D.3, they are suited to a TIA configuration, also known as current-to-voltage converter, such that the photodiode can replace input resistor R_1 in Figure D.2. The photodiode directly generate the current, as the "–" input voltage is zero, the TIA's input impedance is nearly zero, which is exactly what is needed to capture the maximum current from the photodiode.

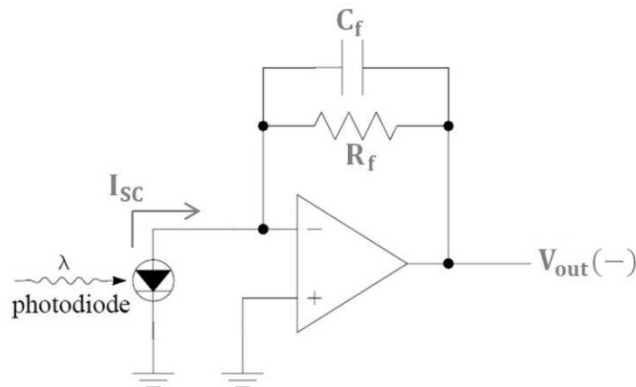


Figure D.3 Trans impedance amplifier [61,62]

In this arrangement, and according to eq. 15, V_{out} always has a negative value proportional to R_f which is the gain.

$$V_{out} = -(I_{SC} \times R_f) \quad (15)$$

$$C_f = \frac{1}{2\pi R_f f} \quad (16)$$

where f is the frequency of discontinuous light.

D-2 Summing amplifier

Two or more inputs can be added together using the circuits shown in Figure D.4. The fact that V_- is a virtual ground can be skilfully used and all signals can be tied together in V_- input.

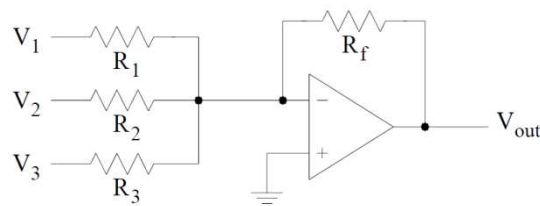


Figure D.4 Summing amplifier [60]

In this configuration, the currents from the different inputs add together at the inverting input and flow through the feedback resistor (R_f) to form an output:

$$V_{\text{out}} = -R_f \left(\frac{V_1}{R_1} + \frac{V_2}{R_2} + \frac{V_3}{R_3} \right) \quad (17)$$

and with equal values for all resistances:

$$V_{\text{out}} = -(V_1 + V_2 + V_3) \quad (18)$$

D-3 Differential amplifier

Figure D.5 represents a differential amplifier in which the output is related to the inputs difference. Owing to a linear relation between output and input, the superposition method can be employed.

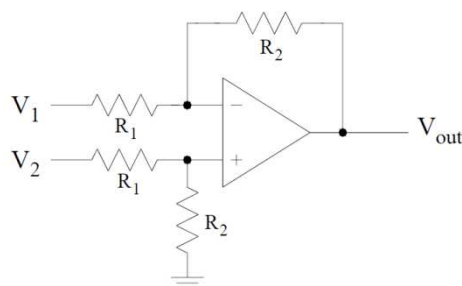


Figure D.5 Differential amplifier [60]

First, the voltage V_1 is turned off (V_1 is short to the ground). It can be similar to a non inverting op-amp with an output given by:

$$V_{out}(V_1 \text{ off}) = \left(\frac{R_1 + R_2}{R_1} \right) V_+ \quad (19)$$

where V_+ is just V_2 reduced by $R_1 : R_2$ voltage divider,

$$V_+ = \left(\frac{R_2}{R_1 + R_2} \right) V_2. \quad (20)$$

Replacing V_+ in eq. 18 ,

$$V_{out}(V_1 \text{ off}) = \left(\frac{R_2}{R_1} \right) V_2. \quad (21)$$

Then, V_2 is turned off. It can be treated as an ordinary inverting op-amp,

$$V_{out}(V_2 \text{ off}) = - \left(\frac{R_2}{R_1} \right) V_1 \quad (22)$$

Adding eq. 21 to eq.22 results in:

$$V_{out} = \left(\frac{R_2}{R_1} \right) (V_2 - V_1) \quad (23)$$

and if all resistors are the same yields:

$$V_{out} = V_2 - V_1 \quad (24)$$

D-4 Log and antilog amplifier

Log and antilog amplifiers can be made either by diodes or transistors. Figure D.6 shows the log amplifier. According to eq. 25, in both cases, the equation is the same and because of V_T (thermal voltage) and I_s (saturation current), it is temperature-dependent.

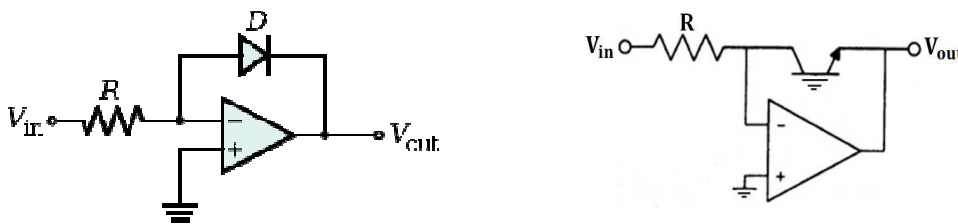


Figure D.6 Diode and transistor log amplifier [63]

$$V_{\text{out}} = -V_T \ln \left(\frac{V_{\text{in}}}{R I_S} \right) \quad (25)$$

or

$$V_{\text{out}} = K_1 \ln \left(\frac{V_{\text{in}}}{V_{\text{ref}}} \right) \quad (26)$$

where K_1 is the scale factor and V_{ref} is a normalized constant in volts which can be regarded as a second constant ($K_2 = \frac{1}{V_{\text{ref}}}$). Regarding antilog amplifier, Figure D.7, there is an exponential relation between the output and input voltages, eq .27.

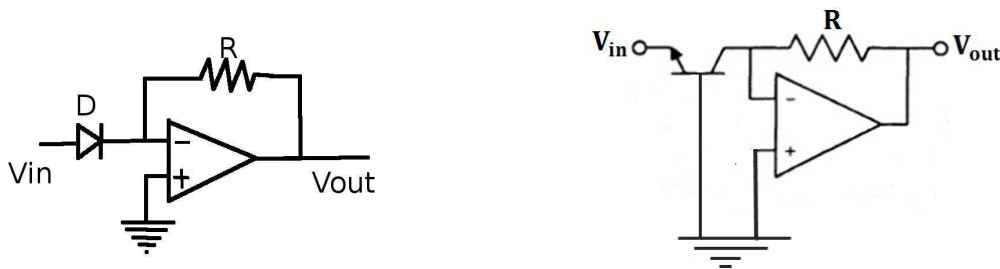


Figure D.7 Diode and transdiode antilog amplifier [64]

$$V_{\text{out}} = -R I_S e^{\frac{V_{\text{in}}}{V_T}} \quad (27)$$

Divider

In order to have the output in the form of $(\Delta x, \Delta y)$, as it is expressed in eq. 10 and eq. 11, which are divisions of two scalar inputs, a divider is selected. It can be built using log and antilog amplifier. The circuit of Figure D.8 gives the output which is proportional to division of two input voltages.

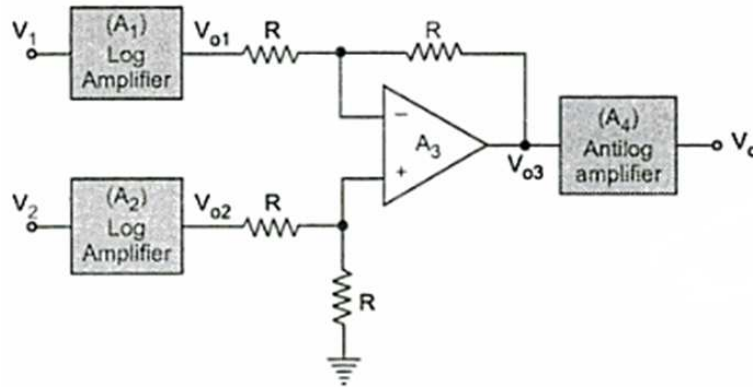


Figure D.8 Analog voltage divider circuit [65]

$$V_o = \frac{1}{K_2} \frac{V_2}{V_1} \quad (28)$$

[60] http://en.wikipedia.org/wiki/Operational_amplifier

[61] P. Horowitz, W. Hill, “The art of electronics”, Cambridge university press, 1989.

[62] HAMAMTSU, “photodiode technical information”,
http://www.physics.ucc.ie/fpetersweb/FrankWeb/courses/PY3108/Labs/PD_Info.pdf

[63] http://en.m.wikipedia.org/wiki/Log_amplifier

[64] http://en.wikipedia.org/wiki/Operational_amplifier_applications

[65] http://en.wikibooks.org/wiki/Electronics/Analog_multipliers

APPENDIX E - ELEMENTS OF METROLOGY FRAME

Elements of metrology frame				
Item		Quantity	Company	Part/Model No.
1-	Laser Madule	1	Thorlabes	CPS180 (4mm, 635nm)
2-	Half Wave Plate	1	Foctek	WPA225H
3-	Quarter Wave Plate	3	Foctek	WPA225Q
4-	Polarizing Beam Splitter	2	Foctek	PBS1107 (Narrow band)
5-	RetroReflector	2	Zygo	7003A
6-	Pentaprism	1	Thorlabes	PS933
7-	Holder of Wave Plate	3	FOCtek	WH3025 (Ring) + WRH30(Rotating)
8-	Holder of PBS	2	FOCtek	MCB1025

LASER SOURCE SPECIFICATION

Thorlabs, Inc. 435 Route 206 • Newton, NJ 07860 • Sales (973)579-7227 • Fax (973)300-3600

Collimator Pen
CPS180

Description

Type number: CPS180
 Date of first issue: Aug-27-98
 Date of change: Sep-01-98

Operational Hazard: Semiconductor Laser Diode

This laser pen emits radiation that is visible to the human eye. When in use, do not look directly into the device. Direct viewing of laser diode emission at close range may cause eye damage, especially in conjunction with collimating lenses. Extreme care must be taken to prevent the beam from being viewed directly or through external optics or mirrors.

Properties

Housing: Stainless steel
 Lens: Glass
 Type of laser: N-type

Features

Operating temperature: -10 to 50 °C
 Storage temperature: -40 to 85 °C
 Application: Non contact measurement

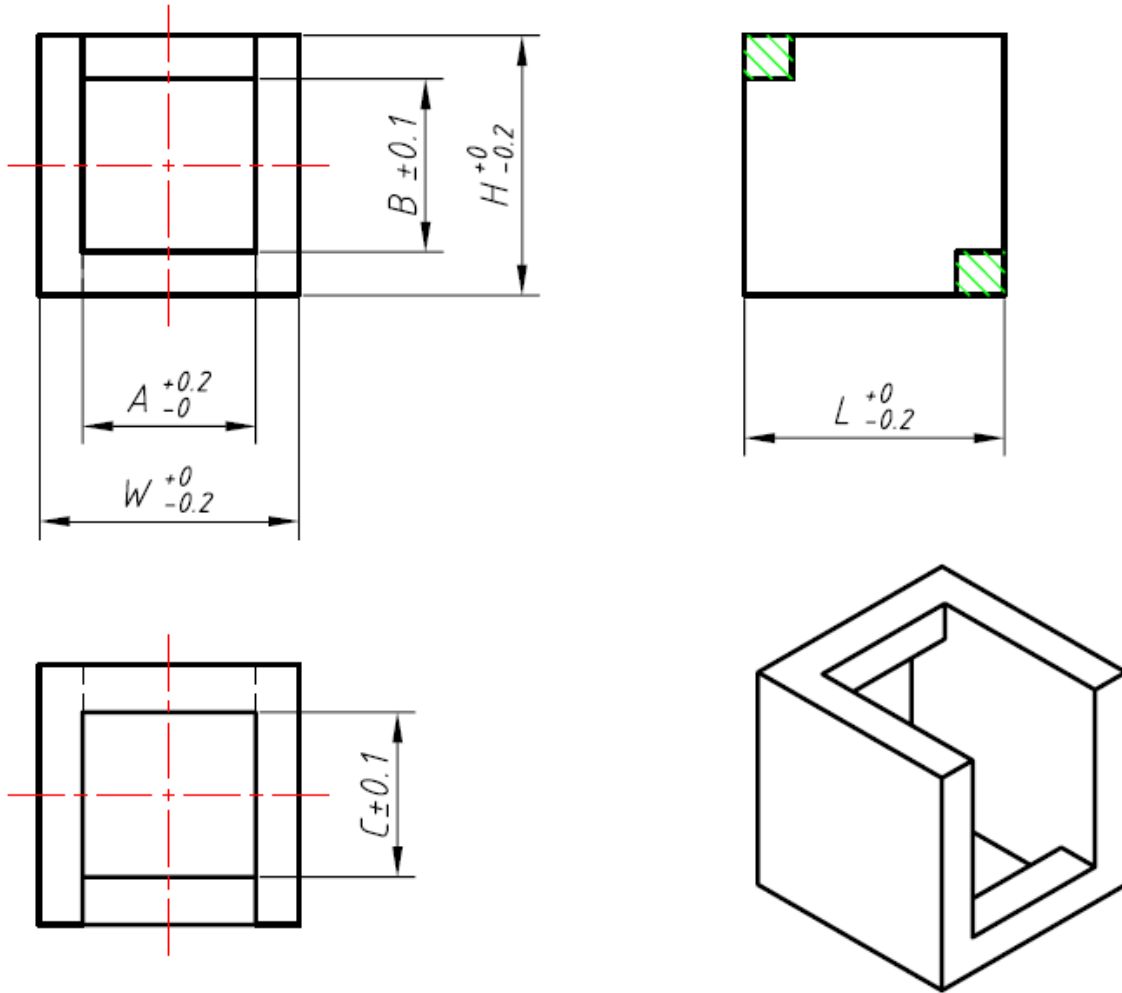
This product conforms to all applicable standards of FDA regulations (DHHS, 21 CFR subchapter J). In combination with a power supply the laser module falls within Safety Class 3R. Due to the small size of these devices, the required warning is affixed to the box containing the laser modules.

Quick reference data

T_{case}=(25 ± 2) °C Po=4.0 mW, unless otherwise specified

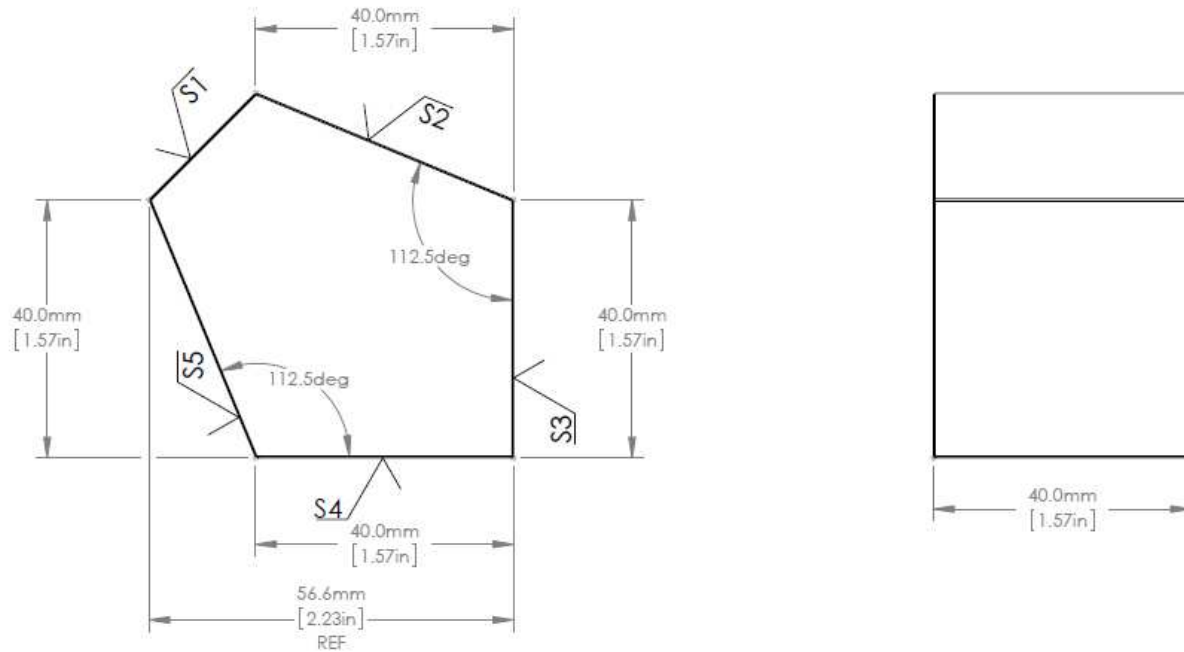
Symbol	Parameter	Conditions	Min	Typ	Max	unit
λ	Wavelength			635	640	nm
Po	Optical output power	100mm from pen		1		mW
D.Lx d//	Beam diameter perpendicular x parallel to the laser stripe	1/e ² (clip 13.5%) at pen exit		4.0 Round		mm
col	Collimation	Including natural divergence			0.3	mrad
α_{om}	Optical-mechanical axis deviation			5	10	mrad
dca	Clear aperture			4		mm
Iop	Operating current laser pen			40	60	mA
Vop	Operating voltage	With reference to ground	-4.5	-5	-5.5	V
Imon	Monitor diode current				0.65	mA

HOLDER OF POLARIZING BEAMSPLITTER



Dimensions					
A	B	C	H	L	W
25.8mm	25.4mm	24.9mm	38mm	38mm	38mm

PENTAPRISM



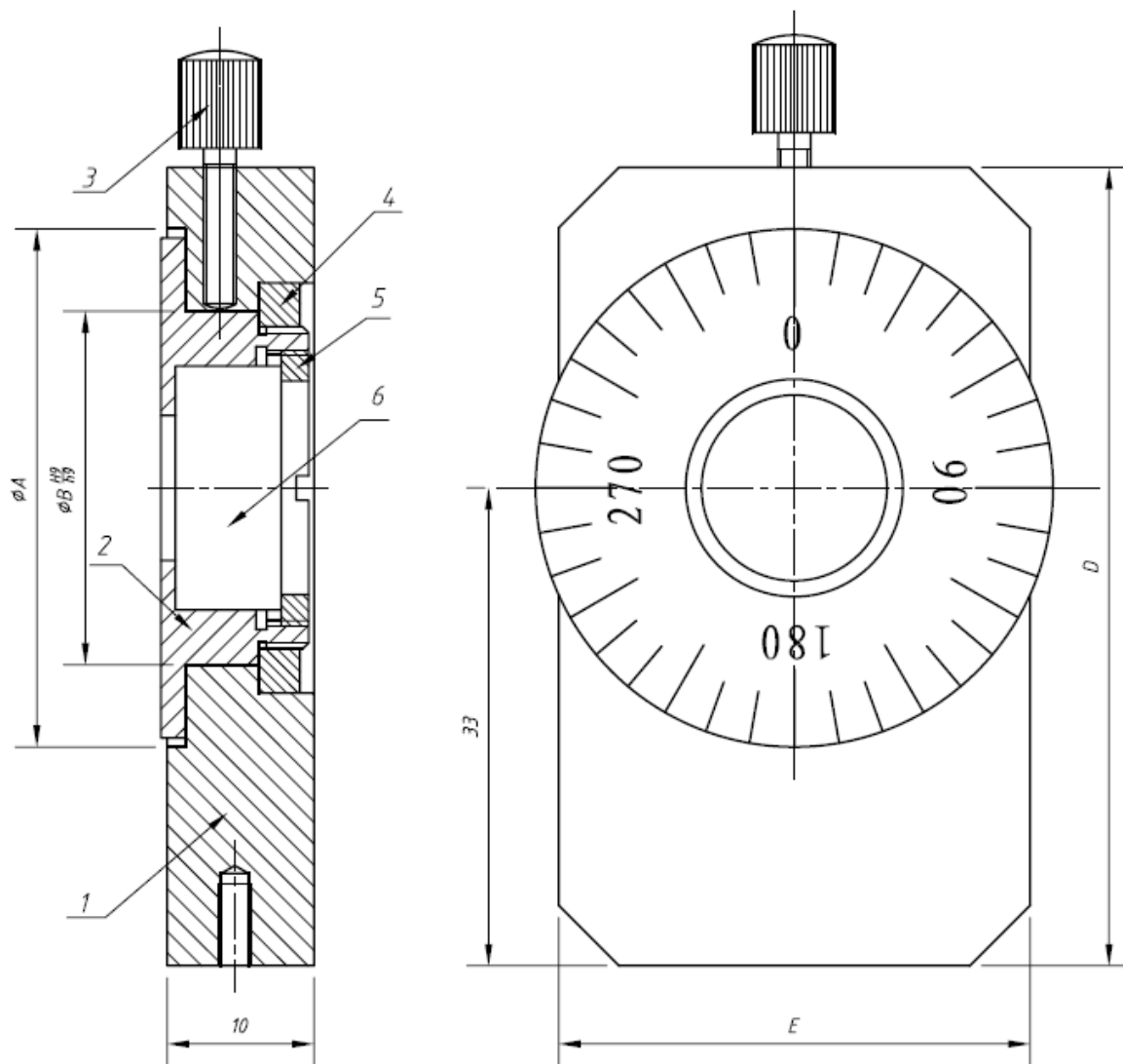
THORLABS 40mm PENTAPRISM
MATERIAL: N-BK7

NOTES/SPECIFICATIONS:

1. CLEAR APERTURE (S2, S3, S4, S5): >70% OF FACE, LENGTH, AND WIDTH
2. SURFACE FLATNESS (S2, S3, S4, S5): $\lambda/10$ AT 632.8nm OVER CLEAR APERTURE
3. SURFACE QUALITY (S2, S3, S4, S5): 40-20 SCRATCH-DIG, (S1) FINE GROUND
4. ANGULAR TOLERANCE: 3 arcmin
5. BEAM DEVIATION: 3 arcmin
6. DIMENSIONAL TOLERANCE: 0.1 mm

HOLDER OF WAVEPLATES

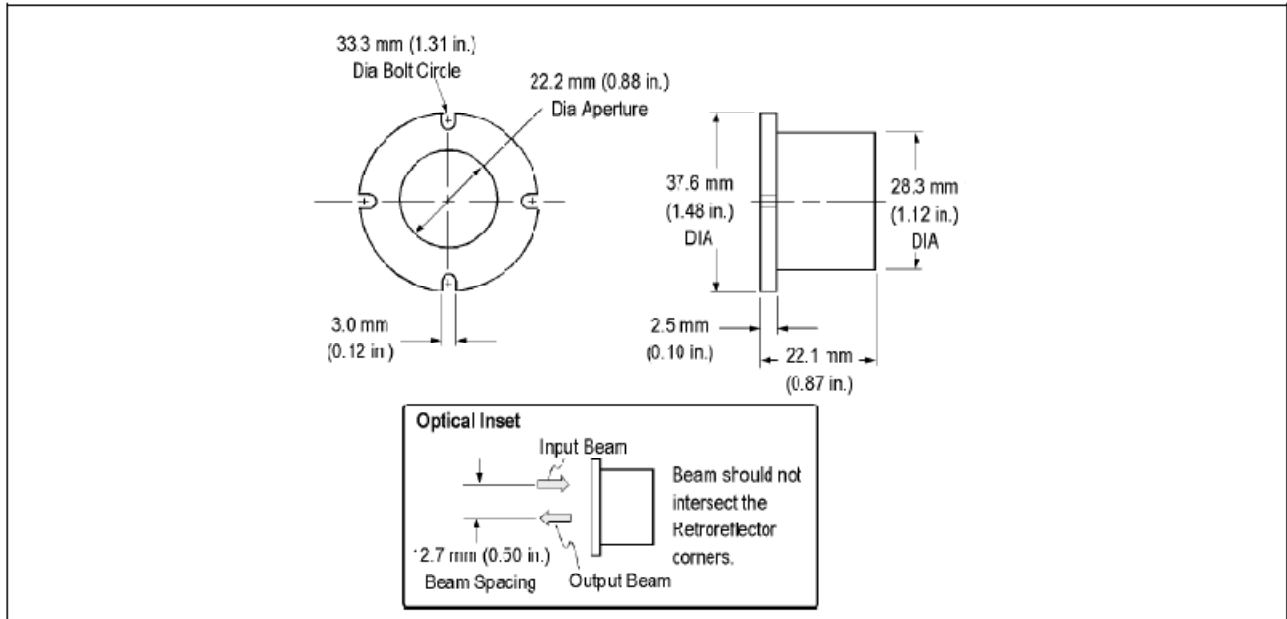
(FOCTEK WRH30)



Dimensions				
A	B	C	D	E
50.5mm	40mm	30.2mm	63mm	45mm

ZYGO RETROREFLECTOR

(P/N: 6191-0438-02)



APPENDIX F - ELEMENTS OF ELECTRICAL SECTION

Elements of electrical section				
Item		Quantity	Company	Part/Model No.
1-	PhotoDetector	1	osioptoelectronics	SPOT-9D (Compatible with 350nm-1100nm, Active area= $19.6 \frac{\text{mm}^2}{\text{segment}}$)
2-	Op-amp	7	OPA-37	newark74K3909 (OPA37GP)
3-	Capacitor	4+1	4*100PF+1*1000PF	
4-	Resistor	22+4	20*200K Ω +4*50K Ω	
5-	Power Supply	1		$\pm 15\text{V}$ and (5V for laser)
6-	Divider	2	AD-534	Newark 13M6172 (AD534JDZ)
7-	BreadBoard (wisherBoard)	1		Newark 18M7115 (WBU-206+J)

APPENDIX G - Test DATA

Deflection Test								
Test No.	Distance (mm)	A(v)	B(v)	C(v)	D(v)	Δx	Δy	A+B+C+D
1	162.20	-0.114	-0.195	-2.247	-3.674	+1.311	-5.634	+6.247
2	162.44	-0.151	-0.264	-2.343	-3.437	+0.975	-5.382	+6. 218
3	162.70	-0.239	-0.388	-2.303	-3.235	+0.763	-4.928	+6.203
4	162.93	-0.631	-0.772	-2.008	-2.621	+0.478	-3.253	+6.071
5	163.13	-1.147	-1.174	-1.605	-2.007	+0.362	-1.285	+5.974
6	163.42	-1.507	-1.493	-1.338	-1.623	+0.295	+0.064	+6.011
7	163.64	-1.783	-1.824	-1.093	-1.282	+0.152	+1.259	+5.996
8	163.91	-2.280	-2.204	-0.701	-0.752	+0.106	+3.042	+5.902
9	164.11	-2.630	-2.557	-4.424	-0.413	+0.049	+4.405	+6.008
10	164.36	-2.832	-2.920	-0.195	-0.190	-0.091	+5.381	+6.151
11	164.60	-2.818	-3.004	-0.128	-0.140	-0.160	+5.619	+6.137

where for all data Δx and Δy are calculated as below :

$$\Delta x = (A+D)-(B+C)$$

$$\Delta y = (A+B)-(C+D)$$

Pitch Tests – Rotation around Y axis (up-down)								
Test No.	Pitch (degree)	A(v)	B(v)	C(v)	D(v)	Δx	Δy	A+B+C+D
1	0	-1.461	-1.509	-1.421	-1.590	+0.134	-0.027	+5.997
2	0.006	-1.148	-1.831	-1.667	-1.313	-1.029	+0.048	+5.952
3	0.012	-0.796	-2.060	-1.939	-1.185	-1.982	-0.266	+5.953
4	0.018	-0.571	-2.253	-2.128	-0.966	-2.834	-0.262	+5.940
5	0.024	-0.361	-2.462	-2.355	-0.706	-3.744	-0.232	+5.902
6	0.030	-0.234	-2.570	-2.551	-0.487	-4.362	-0.218	+5.869
7	0.036	-0.169	-2.455	-2.809	-0.371	-4.688	-0.530	+5.840
8	0.042	-0.139	-2.444	-2.877	-0.282	-4.911	-0.523	+5.820
9	0.048	-0.114	-2.527	-2.887	-0.203	-5.060	-0.470	+5.868
10	0.054	-0.105	-2.454	-2.906	-0.161	-5.077	-0.523	+5.642
11	0.048	-0.117	-2.555	-2.845	-0.205	-5.035	-0.402	+5.725
12	0.042	-0.142	-2.516	-2.794	-0.275	-4.876	-0.393	+5.770
13	0.036	-0.179	-2.506	-2.725	-0.382	-4.634	-0.413	+5.844
14	0.030	-0.254	-2.608	-2.487	-0.504	-4.337	-0.129	+5.893
15	0.024	-0.355	-2.456	-2.380	-0.710	-3.744	-0.274	+5.921
16	0.018	-0.573	-2.375	-2.072	-0.913	-2.944	-0.021	+5.958
17	0.012	-0.835	-2.172	-1.844	-1.110	-2.053	+0.030	+5.936
18	0.006	-1.202	-1.868	-1.587	-1.310	-0.944	+0.159	+5.990
19	0	-1.506	-1.535	-1.406	-1.538	+0.092	+0.186	+6.014
20	-0.006	-1.893	-1.209	-1.078	-1.833	+1.428	+0.193	+6.010
21	-0.012	-2.163	-0.934	-0.896	-2.005	+2.308	+0.223	+6.001
22	-0.018	-2.403	-0.707	-0.701	-2.116	+3.805	+0.330	+5.974
23	-0.024	-2.618	-0.534	-0.545	-2.195	+3.712	+0.438	+5.903
24	-0.030	-2.755	-0.398	-0.422	-2.291	+4.247	+0.478	+5.843
25	-0.036	-2.966	-0.292	-0.337	-2.333	+4.638	+0.618	+5.930
26	-0.042	-3.045	-0.224	-0.274	-2.381	+4.854	+0.626	+5.920
27	-0.048	-3.068	-0.190	-0.241	-2.373	+5.054	+0.730	+5.830
28	-0.054	-3.180	-0.162	-0.201	-2.398	+5.166	+0.766	+5.955
29	-0.048	-3.074	-0.179	-0.238	-2.463	+5.020	+0.588	+5.961
30	-0.042	-2.985	-0.217	-0.280	-2.473	+4.903	+0.465	+5.944
31	-0.036	-2.848	-0.276	-0.349	-2.452	+4.626	+0.350	+5.933
32	-0.030	-2.649	-0.353	-0.440	-2.495	+4.270	+0.135	+5.916
33	-0.024	-2.497	-0.493	-0.571	-2.334	+3.716	+0.122	+5.901
34	-0.018	-2.265	-0.672	-0.761	-2.292	+3.092	-0.116	+6.018
35	-0.012	-2.066	-0.896	-0.934	-2.119	+2.328	-0.074	+6.038
36	-0.006	-1.857	-1.176	-1.116	-1.875	+1.455	+0.087	+6.030
37	0	-1.519	-1.463	-1.384	-1.617	+0.282	+0.016	+6.013

Yaw Tests – Rotation around x axis (right-left)								
Test No.	Yaw (degree)	A(v)	B(v)	C(v)	D(v)	Δx	Δy	A+B+C+D
1	0	-1.356	-1.596	-1.148	-1.570	+0.195	+0.273	+5.692
2	0.01	-1.082	-1.285	-1.356	-1.946	+0.410	-0.895	+5.685
3	0.02	-0.826	-0.955	-1.528	-2.247	+0.561	-1.954	+5.560
4	0.03	-0.494	-0.523	-1.792	-2.575	+0.761	-3.367	+5.420
5	0.04	-0.246	-0.241	-1.821	-2.831	+0.971	-4.173	+5.170
6	0.05	-0.169	-0.157	-1.644	-2.833	+1.183	-4.167	+4.8
7	0.04	-0.248	-0.246	-1.823	-2.811	+0.977	-4.159	+5.140
8	0.03	-0.482	-0.503	-1.779	-2.591	+0.756	-3.410	+5.367
9	0.02	-0.796	-0.917	-1.564	-2.257	+0.578	-2.103	+5.572
10	0.01	-1.064	-1.237	-1.383	-1.981	+0.423	-1.026	+5.694
11	0	-1.320	-1.508	-1.220	-1.708	+0.267	-0.082	+5.724
12	-0.01	-1.538	-1.808	-1.013	-1.343	+0.065	+0.974	+5.690
13	-0.02	-1.698	-2.035	-0.852	-1.053	-0.103	+1.963	+5.701
14	-0.03	-2.012	-2.346	-0.629	-0.670	-0.268	+3.119	+5.662
15	-0.04	-2.276	-2.591	-0.430	-0.394	-0.396	+4.071	+5.760
16	-0.05	-2.372	-2.877	-0.250	-0.206	-0.557	+4.815	+5.710
17	-0.06	-2.377	-3.005	-0.171	-0.137	-0.671	+5.110	+5.617
18	-0.07	-2.343	-3.132	-0.135	-0.107	-0.816	+5.371	+5.768
19	-0.06	-2.413	-3.085	-0.178	-0.139	-0.681	+5.266	+5.840
20	-0.05	-2.478	-2.917	-0.259	-0.204	-0.510	+4.885	+5.712
21	-0.04	-2.273	-2.565	-0.413	-0.372	-0.363	+4.204	+5.634
22	-0.03	-2.111	-2.368	-0.595	-0.625	-0.241	+3.247	+5.687
23	-0.02	-1.785	-2.041	-0.808	-1.012	-0.071	+2.035	+5.703
24	-0.01	-1.548	-1.795	-0.968	-1.323	+0.105	+1.078	+5.740
25	0	-1.368	-1.519	-1.162	-1.638	+0.267	+0.134	+5.677

Repeatability Test #1								
Test No.	Distance (mm)	A(v)	B(v)	C(v)	D(v)	Δx	Δy	A+B+C+D
1	162.32	-0.132	-0.225	-2.346	-3.625	+1.170	-5.644	+6.354
2	162.43	-0.156	-0.267	-2.340	-3.562	+1.110	-5.504	+6.370
3	162.66	-0.245	-0.403	-2.356	-3.278	+0.752	-5.011	+6.325
4	162.90	-0.654	-0.784	-2.060	-2.697	+0.505	-3.315	+6.238
5	163.13	-1.142	-1.172	-1.588	-2.013	+0.402	-1.272	+5.988
6	163.39	-1.487	-1.490	-1.359	-1.621	+0.254	+0.025	+5.978
7	163.62	-1.761	-1.821	-1.107	-1.273	+0.101	+1.237	+5.987
8	163.85	-2.186	-2.175	-0.770	-0.802	+0.025	+2.812	+5.949
9	164.07	-2.538	-2.560	-0.477	-0.446	-0.053	+4.210	+6.017
10	164.40	-2.932	-2.963	-0.173	-0.172	-0.101	+5.612	+6.251
11	164.62	-2.756	-3.120	-0.122	-0.133	-0.355	+5.651	+6.280
12	164.37	-2.772	-2.933	-0.176	-0.177	-0.140	+5.467	+6.130
13	164.09	-2.656	-2.584	-0.431	-0.403	+0.037	+4.421	+6.040
14	163.93	-2.322	-2.183	-0.682	-0.733	+0.149	+3.148	+5.912
15	163.65	-1.827	-1.797	-1.062	-1.280	+0.235	+1.296	+5.991
16	163.44	-1.560	-1.517	-1.285	-1.590	+0.337	+0.218	+5.965
17	163.16	-1.146	-1.151	-1.601	-2.040	+0.430	-1.323	+5.972
18	162.95	-0.687	-0.810	-1.972	-2.560	+0.460	-3.061	+6.059
19	162.64	-0.228	-0.377	-2.340	-3.227	+0.740	-4.977	+6.197
20	162.46	-0.154	-0.274	-2.376	-3.446	+0.951	-5.394	+6.257
21	162.20	-0.114	-0.195	-2.274	-3.674	+1.311	-5.634	+6.247

Repeatability Test #2								
Test No.	Distance (mm)	A(v)	B(v)	C(v)	D(v)	Δx	Δy	A+B+C+D
1	162.20	-0.114	-0.195	-2.247	-3.674	+1.311	-5.634	+6.247
2	162.44	-0.151	-0.264	-2.343	-3.437	+0.975	-5.382	+6.218
3	162.70	-0.239	-0.388	-2.303	-3.235	+0.763	-4.928	+6.203
4	162.93	-0.631	-0.772	-2.008	-2.621	+0.478	-3.253	+6.071
5	163.13	-1.147	-1.174	-1.605	-2.007	+0.362	-1.285	+5.974
6	163.42	-1.507	-1.493	-1.338	-1.623	+0.295	+0.064	+6.011
7	163.64	-1.783	-1.824	-1.093	-1.282	+0.152	+1.259	+5.996
8	163.91	-2.280	-2.204	-0.701	-0.752	+0.106	+3.042	+5.902
9	164.11	-2.630	-2.557	-4.424	-0.413	+0.049	+4.405	+6.008
10	164.36	-2.832	-2.920	-0.195	-0.190	-0.091	+5.381	+6.151
11	164.60	-2.818	-3.004	-0.128	-0.140	-0.160	+5.619	+6.137
12	164.27	-2.807	-2.712	-0.265	-0.263	+0.067	+5.041	+6.008
13	164.05	-2.616	-2.418	-0.488	-0.503	+0.212	+4.073	+6.015
14	163.85	-2.173	-2.031	-0.780	-0.914	+0.284	+2.553	+5.926
15	163.61	-1.809	-1.695	-1.103	-1.388	+0.407	+1.034	+6.005
16	163.40	-1.519	-1.405	-1.314	-1.714	+0.502	-0.080	+5.980
17	163.11	-1.090	-1.094	-1.647	-2.146	+0.485	-1.590	+6.008
18	162.92	-0.526	-0.649	-2.086	-2.773	+0.550	-3.720	+6.088
19	162.64	-0.207	-0.344	-2.316	-3.319	+0.863	-5.080	+6.201
20	162.42	-0.148	-0.253	-2.337	-3.501	+1.050	-5.448	+6.240
21	162.21	-0.11	-0.185	-2.205	-3.714	+1.423	-5.650	+6.219

Repeatability Test #3								
Test No.	Distance (mm)	A(v)	B(v)	C(v)	D(v)	Δx	Δy	A+B+C+D
1	162.21	-0.110	-0.185	-2.205	-3.714	+1.423	-5.560	+6.219
2	162.45	-0.147	-0.251	-2.322	-3.494	+1.072	-5.479	+6.288
3	162.65	-0.206	-0.350	-2.340	-3.315	+0.822	-5.097	+6.243
4	162.93	-0.611	-0.721	-2.020	-2.717	+0.570	-3.419	+6.092
5	163.14	-1.106	-1.120	-1.634	-2.107	+0.442	-1.514	+6.005
6	163.42	-1.507	-1.450	-1.336	-1.681	+0.395	-0.038	+5.996
7	163.60	-1.759	-1.704	-1.136	-1.395	+0.315	+0.970	+6.017
8	163.87	-2.241	-2.088	-0.761	-0.872	+0.231	+2.730	+5.963
9	163.95	-2.444	-2.251	-0.624	-0.665	+0.217	+3.437	+5.934
10	164.19	-2.794	-2.612	-0.335	-0.321	+0.216	+4.911	+6.19
11	164.38	-2.850	-2.765	-0.184	-0.192	+0.086	+5.326	+6.022
12	164.63	-2.860	-2.981	-0.124	-0.138	-0.056	+5.658	+6.054
13	164.40	-2.851	-2.845	-0.184	-0.191	+0.034	+5.370	+6.061
14	164.21	-2.787	-2.631	-0.326	-0.318	+0.136	+4.881	+6.093
15	163.94	-2.420	-2.126	-0.692	-0.761	+0.351	+3.134	+5.988
16	163.74	-2.043	-1.673	-0.955	-1.292	+0.703	+1.511	+5.983
17	163.46	-1.599	-1.396	-1.260	-1.713	+0.653	+0.047	+5.985
18	163.24	-1.281	-1.162	-1.482	-1.997	+0.637	-1.016	+5.948
19	163.00	-0.677	-0.732	-1.899	-2.734	+0.772	-3.227	+6.027
20	162.78	-0.277	-0.406	-2.132	-3.331	+1.048	-4.805	+6.175
21	162.50	-0.151	-0.254	-2.180	-3.662	+1.366	-5.448	+6.293
22	162.29	-0.120	-0.197	-2.165	-3.730	+1.467	-5.635	+6.263

Repeatability Test #4								
Test No.	Distance (mm)	A(v)	B(v)	C(v)	D(v)	Δx	Δy	A+B+C+D
1	162.29	-0.120	-0.197	-2.165	-3.730	+1.467	-5.635	+6.263
2	162.52	-0.160	-0.268	-2.183	-3.612	+1.318	-5.375	+6.257
3	162.77	-0.261	-0.397	-2.171	-3.331	+1.017	-4.862	+6.189
4	162.98	-0.671	-0.751	-1.927	-2.703	+0.694	-3.212	+6.081
5	163.25	-1.274	-1.170	-1.488	-1.992	+0.597	-1.028	+5.954
6	163.48	-1.621	-1.437	-1.250	-1.665	+0.586	+1.166	+5.994
7	163.74	-1.941	-1.791	-0.990	-1.248	+0.417	+1.526	+5.990
8	163.92	-2.265	-2.114	-0.711	-0.824	+0.297	+2.917	+5.950
9	164.24	-2.824	-2.534	-0.321	-0.331	+0.396	+4.884	+6.141
10	164.42	-3.091	-1.776	-0.193	-0.196	+0.295	+5.422	+6.144
11	164.65	-2.957	-2.904	-0.124	-0.138	+0.074	+5.671	+6.146
12	164.40	-2.954	-2.754	-0.194	-0.201	+0.164	+5.295	+6.157
13	164.22	-2.854	-2.522	-0.331	-0.338	+0.329	+4.796	+6.050
14	163.92	-2.341	-2.032	-0.716	-0.858	+0.461	+2.933	+5.963
15	163.73	-1.985	-1.741	-0.968	-1.259	+0.539	+1.536	+5.977
16	163.52	-1.732	-1.457	-1.165	-1.596	+0.697	+0.462	+5.984
17	163.34	-1.407	-1.218	-1.370	-1.904	+0.717	-0.637	+5.918
18	163.15	-1.077	-1.019	-1.619	-2.271	+0.697	-1.794	+6.017
19	162.94	-0.520	-0.597	-1.972	-2.974	+0.892	-3.851	+6.119
20	162.74	-0.259	-0.388	-2.142	-3.371	+1.097	-4.877	+6.199
21	162.54	-0.163	-0.272	-2.159	-3.630	+1.353	-5.384	+6.310

Repeatability Test #5								
Test No.	Distance (mm)	A(v)	B(v)	C(v)	D(v)	Δx	Δy	A+B+C+D
1	162.54	-0.163	-0.272	-2.159	-3.630	+1.353	-5.384	+6.310
2	162.81	-0.293	-0.418	-2.112	-3.307	+1.068	-4.735	+6.186
3	162.94	-0.569	-0.636	-1.963	-2.896	+0.845	-3.665	+6.104
4	163.16	-1.088	-1.047	-1.621	-2.228	+0.635	-1.705	+6.010
5	163.35	-1.406	-1.255	-1.380	-1.861	+0.624	-0.560	+5.927
6	163.53	-1.674	-1.492	-1.204	-1.593	+0.565	+0.381	+5.979
7	163.73	-1.950	-1.756	-1.008	-1.254	+0.435	+1.496	+5.996
8	163.88	-2.185	-2.038	-0.768	-0.917	+0.291	+2.283	+5.948
9	164.07	-2.607	-2.315	-0.514	-0.567	+0.334	+3.902	+5.998
10	164.24	-2.854	-2.544	-0.314	-0.326	+0.281	+4.803	+6.016
11	164.45	-2.987	-2.717	-0.177	-0.188	+0.251	+5.443	+6.118
12	164.62	-2.901	-2.905	-0.128	-0.144	+0.043	+5.666	+6.105
13	164.41	-2.966	-2.716	-0.201	-0.187	+0.228	+5.376	+6.080
14	164.23	-2.884	-2.526	-0.323	-0.331	+0.345	+4.815	+6.115
15	163.94	-2.402	-2.061	-0.708	-0.810	+0.413	+2.991	+5.993
16	163.79	-2.066	-1.809	-0.914	-1.160	+0.511	+1.847	+5.982
17	163.59	-1.797	-1.518	-1.129	-1.526	+0.668	+0.684	+5.992
18	163.40	-1.467	-1.278	-1.332	-1.843	+0.702	-0.418	+5.947
19	163.25	-1.285	-1.137	-1.473	-2.032	+0.697	-1.063	+5.954
20	163.06	-0.842	-0.857	-1.789	-2.560	+0.744	-2.657	+6.070
21	162.90	-0.443	-0.532	-2.043	-3.060	+0.905	-4.142	+6.133
22	162.76	-0.244	-0.371	-2.131	-3.416	+1.133	-4.946	+6.184
23	162.54	-0.162	-0.269	-2.135	-3.654	+1.392	-5.368	+6.224

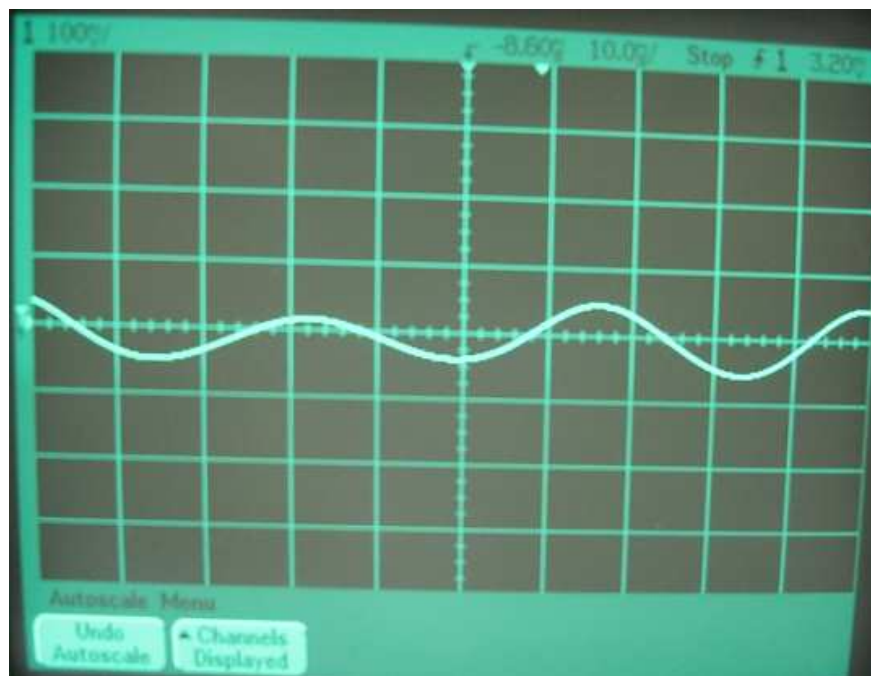
APPENDIX H - Noise signals related to each segment of the electrical section

Figure H.1 Error signal related to leg A of photodiode (before resistor)

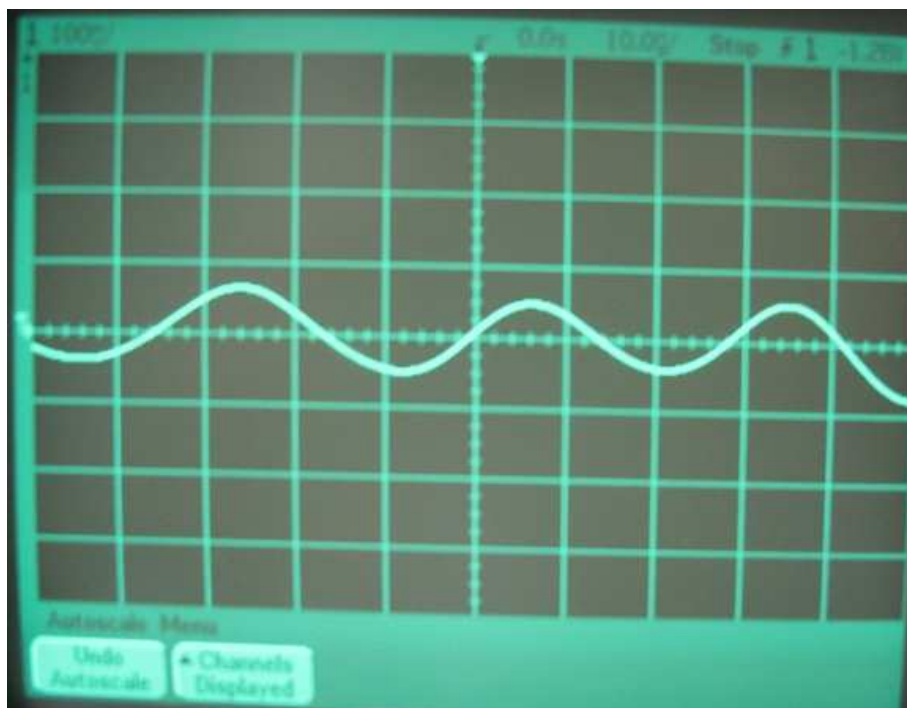


Figure H.2 Error signal related to leg A of photodiode (A)

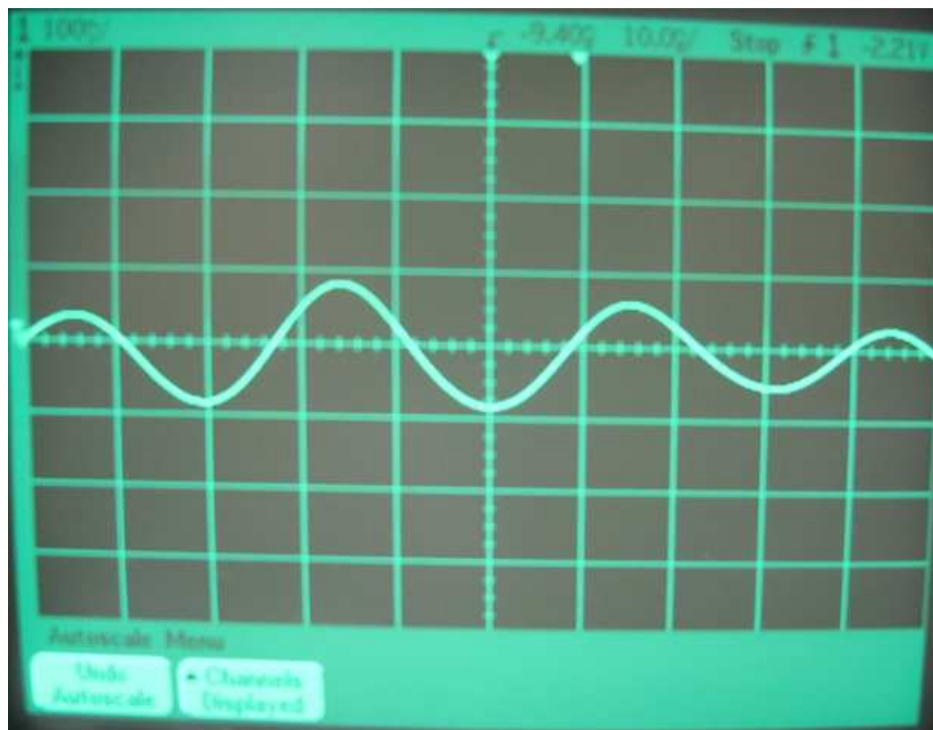


Figure H.3 Error signal related to leg B of photodiode (B)

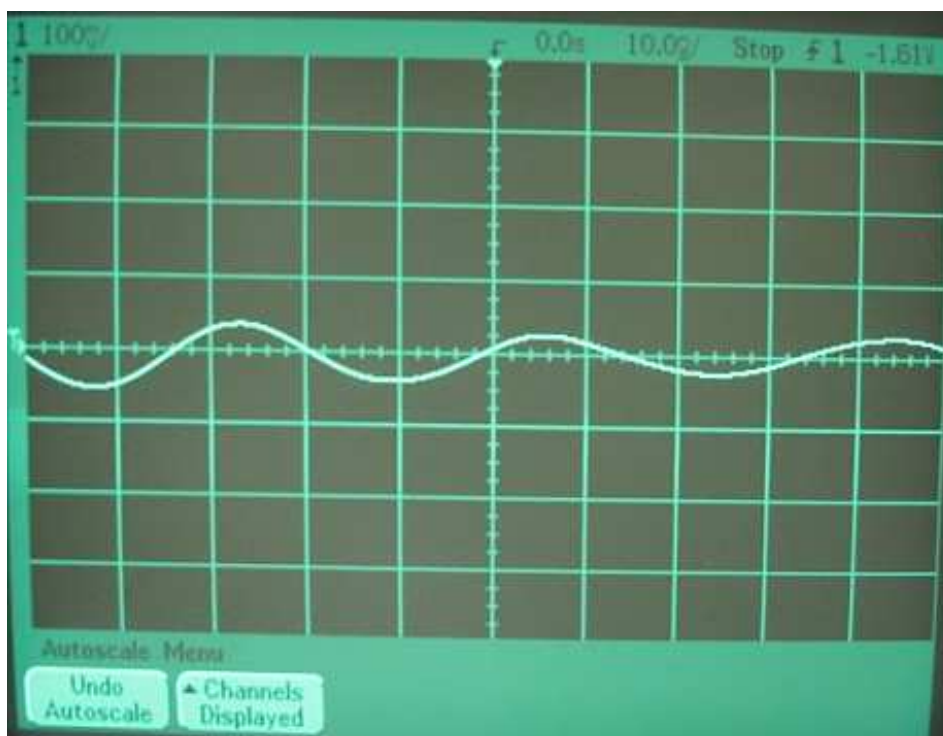


Figure H.4 Error signal related to leg C of photodiode (C)

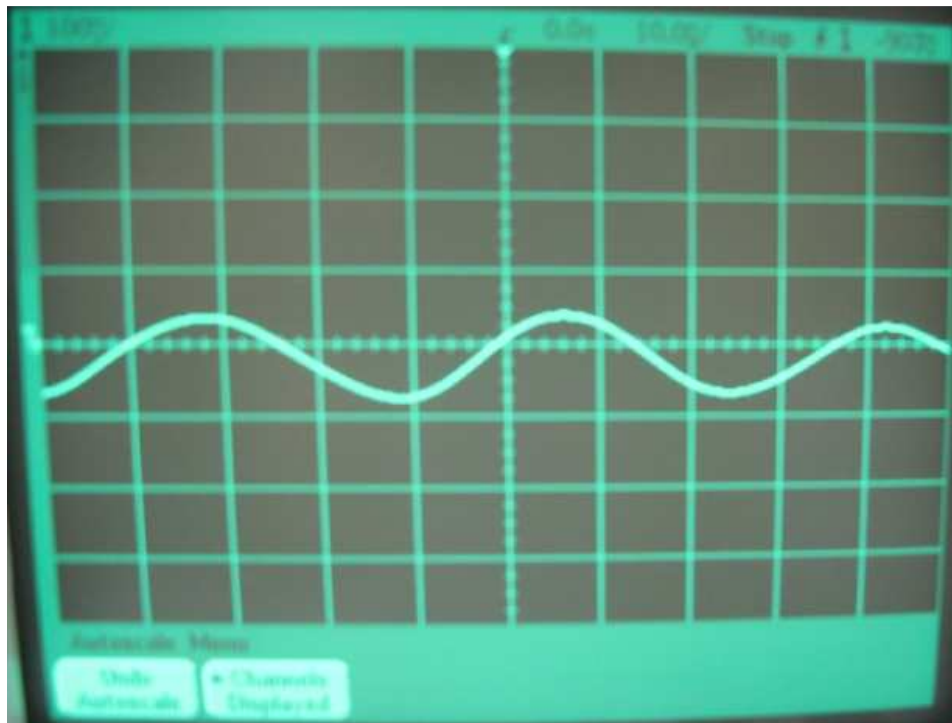


Figure H.5 Error signal related to leg D of photodiode (D)

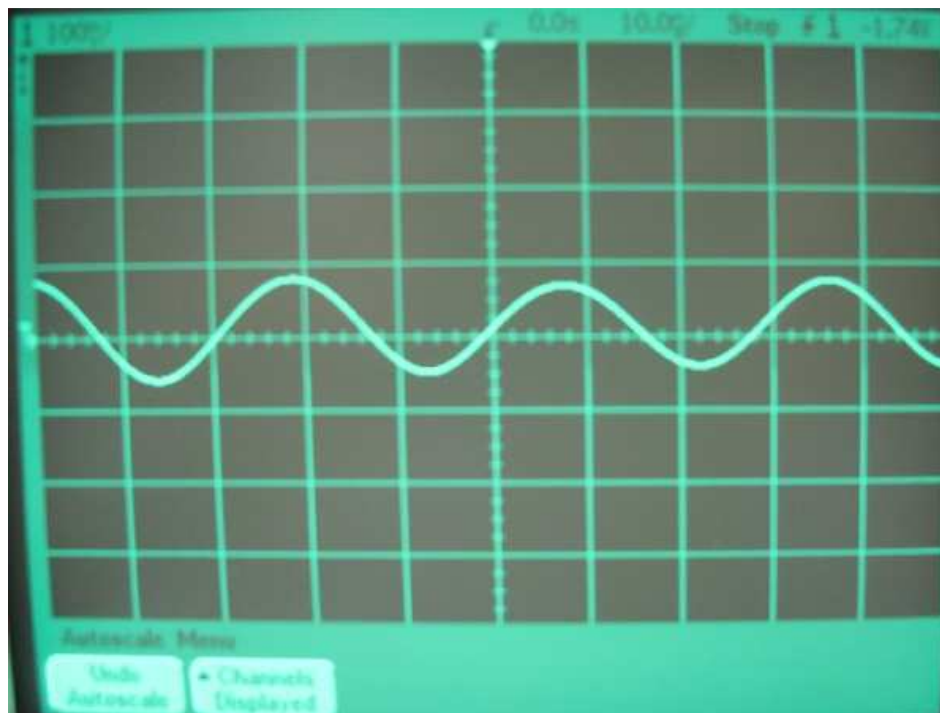


Figure H.6 Error signals of first differential amplifier(E)

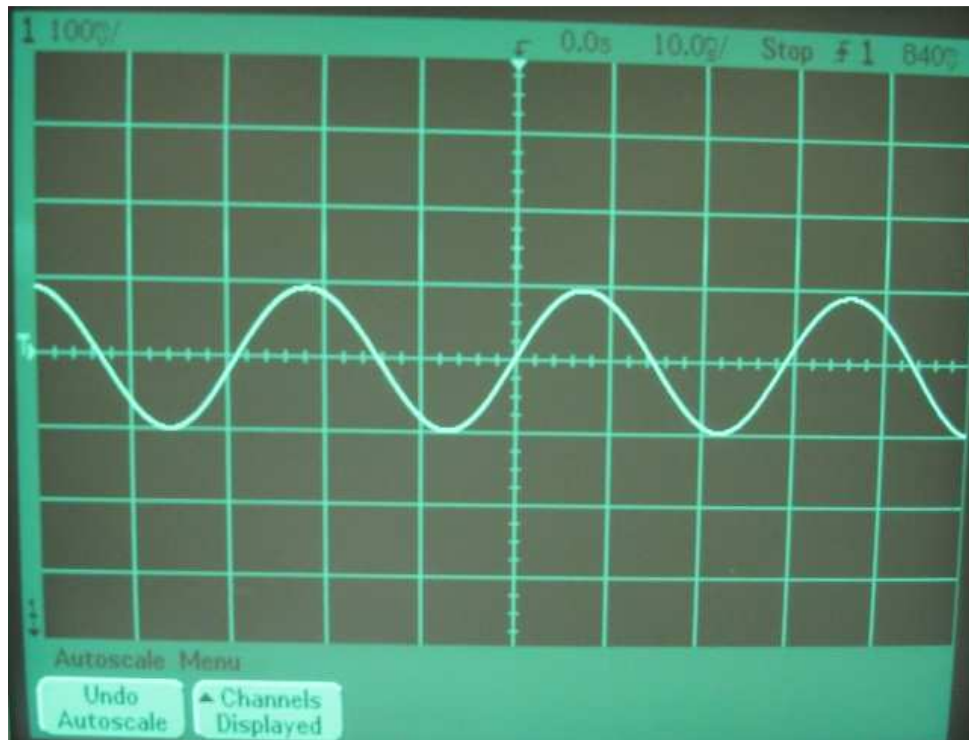


Figure H.7 Error signals of second differential amplifier (F)

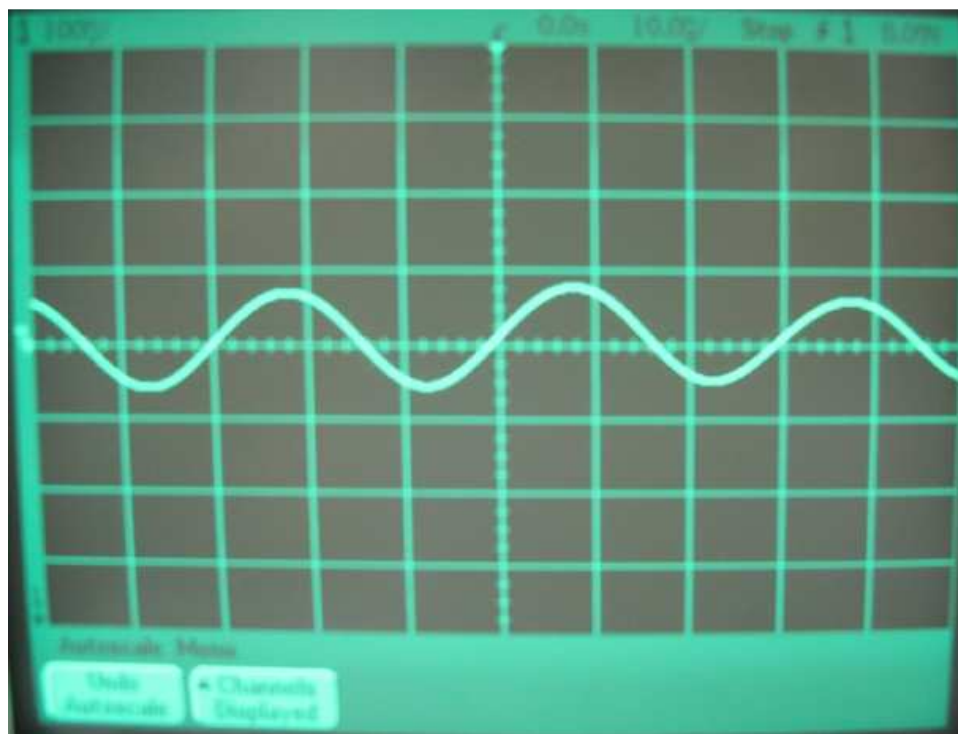


Figure H.8 Error signals of sum amplifier (G)